

UNIVERSITÉ DE BOURGOGNE

Laboratoire Interdisciplinaire Carnot de Bourgogne UMR CNRS 6303

NATIONAL ACADEMY OF SCIENCES OF ARMENIA

Institute for Physical Research

**STUDY OF THE COHERENT EFFECTS IN RUBIDIUM ATOMIC VAPOR
UNDER BI-CHROMATIC LASER RADIATION**

by
Rafayel MIRZOYAN

A Thesis in Physics

Submitted for the Degree of Doctor of Philosophy

Date of defense June 04 2013

Jury

Stefka CARTALEVA	Professor Institute of Electronics, BAS, Sofia	Referee
Arsen HAKHOUMIAN	Professor, Director of the Institute IRPHE Institute of Electronics, BAS, Sofia	Examiner
Claude LEROY	Professor ICB, Université de Bourgogne, Dijon	Supervisor
Aram PAPOYAN	Professor, Director of the institute IPR IPR, NAS of ARMENIA, Ashtarak	Co-Supervisor
Yevgenya PASHAYAN-LEROY	Dr. of Physics ICB, Université de Bourgogne, Dijon	Co-Supervisor
Hayk SARGSYAN	Professor Russian-Armenian State University, Yerevan	Examiner
David SARKISYAN	Professor IPR, NAS of ARMENIA, Ashtarak	Supervisor
Arlene WILSON-GORDON	Professor Bar-Ilan University, Ramat Gan	Referee

LABORATOIRE INTERDISCIPLINAIRE CARNOT DE BOURGOGNE-UMR CNRS 6303
UNIVERSITE DE BOURGOGNE, 9 AVENUE A. SAVARY - 21078 DIJON - FRANCE

INSTITUTE FOR PHYSICAL RESEARCH, NATIONAL ACADEMY OF SCIENCES OF
ARMENIA ASHTARAK-2, 0203 ARMENIA

Remerciements

Je désire exprimer ma sincère considération à mes Directeurs de thèse, les Professeurs Aram Papoyan, David Sarkisyan, Claude Leroy et Dr Yevgenya Pashayan-Leroy pour leur soutien moral et scientifique et leur aide constante.

Je remercie l'Ambassade de France en Arménie pour son aide financière, notamment la bourse N^o. 2011-3369 en tant que Boursier du Gouvernement Français. Je veux remercier Jean-Paul Martin, Anne Rosensthiel puis Guillaume Bréjot du SCAC pour leur grande aide pendant ces deux dernières années. Ce financement m'a aussi permis de découvrir la culture française et de bénéficier de l'apport scientifique d'une collaboration réelle entre une équipe de recherche française et une équipe de recherche arménienne.

Je voudrais aussi remercier tous mes collègues et tout le personnel de l'Institute for Physical Research de l'Académie des sciences d'Arménie et du Laboratoire Interdisciplinaire Carnot de Bourgogne de l'université de Bourgogne pour leur aide et leur chaleureuse camaraderie.

Acknowledgments

I desire to express my sincere gratitude to my supervisors Prof. Claude Leroy, Dr Yevgenya Pashayan-Leroy and Professors Aram Papoyan and David Sarkisyan for their moral and scientific support and constant help.

I acknowledge the support of French Embassy in Armenia for Grant N^o. 2011-3369 as Boursier du Gouvernement Français. I want to thank Jean-Paul Martin, Anne Rosensthiel then Guillaume Bréjot of the SCAC for their great help during these two last years. This grant allowed me to discover the French culture and to benefit of both scientific contribution coming from a real collaboration between an Armenian research team and a French one.

I would also like to thank all the co-workers and staff of the Institute for Physical Research of National Academy of Sciences and Laboratoire Interdisciplinaire Carnot de Bourgogne of University of Bourgogne for the valuable assistance, kindly and warmhearted attitude.

Research conducted in the scope of the International Associated Laboratory IRMAS (CNRS-France & SCS-Armenia)

Part of the research leading to these results has received funding from the European Union FP7/2007-2013 under grant agreement n^o 205025 - IPERA



Etude des effets cohérents dans la vapeur de rubidium atomique sous irradiation laser bi-chromatique

L'intérêt continu du piégeage cohérent de population (Coherent Population Trapping CPT) et du phénomène associé de transparence induite électromagnétiquement (Electromagnetically Induced Transparency EIT) s'explique par un nombre important d'applications dans divers domaines de la physique tels que le refroidissement laser, le stockage d'informations, la magnétométrie, la spectroscopie, les étalons de fréquence atomique etc. [1].

La résonance EIT est usuellement formée dans un système Λ ayant deux états de grande durée de vie et un état excité couplés par deux diodes laser CW. Cette résonance indique une forte décroissance de l'absorption alors qu'un maximum est attendu en l'absence de champ laser de couplage (une résonance EIT peut aussi se former dans des systèmes échelle Ξ et V). D'un point de vue applicatif, il est important de réduire les dimensions de la cellule contenant la vapeur d'atomes métalliques où se forme la résonance EIT, mais de conserver en même temps de bons paramètres de résonance, ce qui permettra la mise au point de dispositifs compacts basés sur des effets cohérents.

En 2002, une première publication décrit une nouvelle résonance (appelée résonance N) qui peut apparaître dans des systèmes Λ dans des conditions similaires à la formation de la résonance EIT. Le nombre de possibles applications de cette résonance N apparaît aussi important que dans le cas des résonances. Là encore, d'un point de vue applicatif, il est important de réduire les dimensions de la cellule où se forme la résonance N.

Les premiers résultats préliminaires indiquent que l'utilisation de cellules minces et ultraminces, contenant des vapeurs d'atomes métalliques, afin de former des résonances EIT ou N nécessitent de bons paramètres pour une utilisation ultérieure. Il est important de noter qu'il n'y avait, dans la littérature scientifique, que deux publications relatives à la formation des résonances EIT dans des cellules minces submicroniques (avant le début de cette thèse) et aucune relative à la formation de résonance N dans des cellules minces de cette épaisseur.

En conséquence, l'étude de ces problèmes était important tout à la fois d'un point de vue scientifique et du point de vue des applications pratiques.

Dans le **chapitre I**, un état de l'art, c'est-à-dire un examen de la littérature existante, sur l'effet EIT est présenté. Nous y décrivons dans quel type de système atomique peut se former le phénomène EIT. La physique appropriée à la technique EIT est décrite en détail. La théorie de l'effet EIT est expliquée en détail. Les motivations et objectifs de l'observation

de la résonance EIT dans des cellules minces sont présentés.

Le dispositif expérimental d'étude de la résonance EIT est expliqué. Les paramètres techniques de tous les dispositifs sont décrits. La construction de nano et micro cellules contenant des vapeurs d'atomes métalliques est explicitée. La détermination de l'épaisseur d'une nanocellule à l'aide d'un faisceau laser est démontrée.

Nous démontrons de même la formation de résonances N dans des nanocellules d'épaisseur $L = \lambda$. Le spectre de la transition sonde dans une nanocellule d'épaisseur $L = \lambda$ est comparé avec le spectre théorique avec un bon accord qualitatif. La formation d'une résonance EIT dans une nanocellule d'épaisseur $L = \lambda/2$ est réalisée pour la première fois. Le spectre de la transition sonde dans une nanocellule d'épaisseur $L = \lambda/2$ est comparé avec le spectre théorique avec un bon accord qualitatif.

Dans le **chapitre II**, nous présentons le comportement de la résonance EIT dans un champ magnétique, pour la transition D_1 d'atomes de rubidium. Une brève présentation de la littérature concernant ce phénomène est énoncée. Nous montrons que, dans un champ magnétique B , la résonance EIT éclate en 3 nouvelles résonances EIT (3 composantes) dans le cas de la transition D_1 du rubidium ^{87}Rb . Nous présentons le diagramme montrant tous les systèmes Λ possibles et nous examinons toutes les composantes. Il est ainsi démontré que, dans le cas de la transition D_1 du rubidium ^{87}Rb , le comportement des 3 composantes dépend de l'écart à la résonance de la fréquence du laser de couplage des sous-niveaux correspondants. Ainsi pour un champ magnétique $B > 350$ G, seulement deux composantes sont détectables, et pour $B > 1200$ G, une seule des composantes EIT est visible. Les résultats expérimentaux ainsi que les calculs théoriques pour l'isotope 87 du rubidium sont présentés et la comparaison théorie-expérience indique un très bon accord.

Nous présentons ensuite l'étude expérimentale du comportement de la résonance EIT dans des champs magnétiques intenses jusqu'à 1,7 kG dans le cas d'une cellule de $30 \mu\text{m}$ remplie de vapeur de rubidium atomique et de néon comme gaz tampon. Nous montrons que la résonance EIT pour le système Λ de la transition D_1 du ^{87}Rb dans un champ magnétique longitudinal se scinde en cinq composantes, dont le comportement en fréquence dépend de la configuration en fréquence des lasers pompe et sonde ainsi que de l'amplitude du champ magnétique. Nous montrons aussi que l'étude des caractéristiques des composantes de la résonance EIT dans des champs magnétiques intenses permet facilement de révéler l'apparition du régime Paschen-Back pour la structure hyperfine de ces atomes.

Le **chapitre III** décrit la formation d'une résonance N dans une microcellule. Une

présentation de la littérature concernant le phénomène de résonance N est énoncée. La technique expérimentale utilisée est décrite. Le diagramme de formation de résonance N pour la transition D_1 du rubidium 85 est décrit. L'observation d'une résonance N en cascade à bande étroite se formant dans un système Λ d'atomes de rubidium pour des cellules telles que $L = 8$ mm et $L = 40-90$ μm en présence de gaz néon à la pression de 6, 20, 200 et 400 Torr est explicitée. La détection de la résonance N au minimum d'épaisseur de la colonne de vapeur à 40 μm est réalisée. La dépendance des paramètres de la résonance N avec l'angle formé par les deux lasers (qui sont utilisés pour former la résonance) est décrite. Nous reportons aussi l'observation simultanée de la formation de résonances N et EIT à l'aide d'une cellule multi-régions remplie de rubidium naturel et de 150 Torr de néon (pour des régions micrométriques d'épaisseur L variant de 1 μm à 90 μm). Nous avons effectué la détection simultanée d'un signal de battement à basse fréquence et d'une résonance N, ce qui permet la détermination direct de la fréquence du laser de couplage. Les applications possibles sont énumérées.

Enfin dans le **chapitre IV**, nous examinons l'éclatement d'une résonance N dans un champ magnétique en utilisant une microcellule remplie de rubidium et de néon comme gaz tampon. Nous présentons les résultats des études du comportement d'une résonance N formée dans un système Λ de la transition D_1 de vapeur atomique de ^{87}Rb dans des champs magnétiques variant de 1 à 200 G pour une microcellule d'épaisseur $L = 50$ μm . Le modèle théorique utilisé explique très bien l'éclatement de la résonance N en trois composantes dans un champ magnétique externe pour la transition D_1 du ^{87}Rb . L'éclatement de la résonance N en cinq composantes pour la transition D_1 du ^{85}Rb pour des champs magnétiques longitudinaux de 1 à 2100 G est décrit. Les résultats expérimentaux sont présentés. Les calculs théoriques du décalage en fréquence des composantes de la résonance N sont explicités. La comparaison des résultats expérimentaux et théoriques indique un très bon accord. L'éclatement de la résonance N en six composantes pour la transition D_1 du ^{85}Rb dans un champ magnétique est décrit. Le diagramme décrivant les systèmes Λ participant au processus de formation des composantes d'une résonance N est présenté. La comparaison des résultats expérimentaux et théoriques indique un très bon accord.

Les mécanismes physiques de formation d'une résonance N sont décrits.

Contents

Introduction	9
1 Formation of narrow resonances using the process of electromagnetically induced transparency (EIT) in cells of micrometer and nanometer thickness filled with Rb vapor	15
1.1 Survey of EIT	15
1.1.1 Introduction to EIT	15
1.1.2 Applications using EIT	18
1.1.3 Physical constraints on EIT	21
1.2 EIT Hamiltonian	23
1.2.1 Outline	23
1.2.2 Deriving the EIT Hamiltonian	24
1.2.3 Rotating Wave Approximation	27
1.2.4 Corotating frame	29
1.2.5 Analysis in terms of dressed and dark states	31
1.3 Motivations and objectives	35
1.4 Theory of EIT in nanocells	37
1.4.1 Interacting systems: atomic vapor and electromagnetic fields	37
1.4.2 Modeling of the rubidium atom within the D_1 -line	38
1.4.3 Assumptions and hypotheses	39
1.4.4 Basic equations	40
1.4.5 Absorption spectra	42
1.5 The experimental setup for the study of EIT	45

1.5.1	Construction of thin cells containing atomic vapors (of width from a few to hundreds of μm)	54
1.5.2	Construction of nanocells containing atomic vapors	57
1.5.3	Determination of the thickness of a nanocell using a laser beam	58
1.6	EIT: The coupling laser frequency is on resonance with atomic transition.	61
1.6.1	EIT: thickness of the cell $L = \lambda$	63
1.6.2	EIT: thickness of the cell $L = \lambda/2$	67
2	The EIT-resonance splitting in a magnetic field using a nanocell and a microcell.	70
	Introduction	70
2.1	Experimental technique	72
2.2	The splitting of the EIT-resonance on three components: ^{87}Rb , D_1 -line, the vapor thickness $L = \lambda$	75
2.3	The EIT-resonance splitting in a magnetic field in case of microcell: magnetic field $B < 2000$ G	84
3	N-resonance formation in micron thickness cells, filled with the Rb atom vapors and neon buffer gas	92
	Introduction	92
3.1	Literature overview of N -type resonance	93
3.2	Experimental technique	94
3.3	Formation of N -type resonance in the vapor of atoms Rb, D_1 -line, in the presence of neon buffer gas	96
3.4	The low-frequency beating signal when the condition $\nu_C \approx \nu_P$ is fulfilled	104
3.5	Simultaneous Observation of N - and EIT-Resonances in Micrometric Thin Cell	105
4	The N-type resonance splitting in magnetic field using microcell with the addition of neon buffer gas	108
4.1	The N -type resonance splitting on three components: ^{87}Rb , D_1 -line	108
4.2	The N -type resonance splitting on five components: ^{85}Rb , D_1 -line	114

4.3	The N -type resonance splitting into six components: ^{85}Rb , D_1 -line	119
4.4	Physical mechanisms of N -type resonance formation	123
	Conclusion	129
	Bibliography	132

Introduction

The relevance of the subject

Continuous interest to coherent population trapping (CPT) and related electromagnetically induced transparency (EIT) phenomena is stipulated by a number of important applications in a variety of fields such as laser cooling, information storage, magnetometry, spectroscopy, atomic frequency references etc. [1].

EIT-resonance is usually formed in a Λ -system with two long-lived states and one excited state coupled by two cw diode laser fields and displays a strong reduction in absorption where a maximum is expected in the absence of the coupling laser field (EIT can occur also in ladder Ξ - and V -systems). From application point of view, it is important to reduce the dimensions of a cell containing atomic metal vapor where the EIT-resonance is formed, at the same time keeping good resonance parameters, which will allow creation of compact devices based on coherent effects.

In 2002 it was reported about a new resonance (so-called N -type resonance) that can appear in Λ -system under the conditions similar to that for the EIT-resonance formation [2]. A number of applications of this N -type resonance could be as wide as in the case of the EIT and CPT-resonances. From application point of view, it is important to reduce the dimensions of the cell, where the N -resonance is formed.

The obtained preliminary results indicate, that a successful application of thin and ultra-thin cells containing vapors of metal atoms to form the EIT-resonances and N -type resonances with good parameters is necessary for their further use. Note, that there were only two publications concerning the formation of the EIT-resonances in submicron thick cells in the literature (before the beginning of the thesis), and no any publication for the formation of

N -type resonances in thin cells of this thickness. Thus, the study of these problems was important from both the scientific point of view and for practical applications.

The aim of the work is a detailed study of the EIT-resonance and the N -type resonance formation in ultrathin (20-1000 nm) and thin (10-700 μm) cells filled with vapors of Rb atoms under the radiation of two narrow-band cw lasers (couple, ν_c and probe, ν_p). Particularly, it was important to study the influence of laser intensity, temperature, density of atoms and atomic collisions with the walls of cells. Also of practical interest is to study the EIT-resonance and N -type resonance under the influence of external magnetic field.

Objectives of the thesis:

1. Development of thin and ultrathin sealed off cells containing vapors of Rb, with the possibility of thickness variation in the range of 20 nm - 2 mm.
2. Investigation of different Λ -systems in vapors of Rb atoms (D_1 and D_2 -lines) for the formation of narrow EIT- and N -type resonances depending on the thickness L in the range of 20 nm - 2 mm.
3. Investigation of the influence of an external magnetic field on the EIT-resonances in ^{85}Rb and ^{87}Rb .

Scientific novelty:

1. For the first time the resonance of electromagnetically induced transparency is registered in a nanocell filled with the vapors of Rb atoms (vapor column thickness $L = \lambda = 795$ nm, Rb D_1 -line) with the high 40% contrast. EIT-resonance is registered at an extremely low thickness $L = \lambda/2 = 397$ nm, but with a lower contrast. The experimental results are in good agreement with theory.
2. It is demonstrated that the addition of a buffer gas in a nanocell with rubidium vapor can significantly increase (compared to the nanocell without buffer gas) frequency tuning range of the EIT-resonance in atomic vapor column of thickness $L = \lambda = 795$ nm.
3. For the ^{85}Rb atoms, for the first time, the splitting of EIT-resonance into five components in a thin cell is observed under influence of strong external magnetic field ($<$

1700 G). It is shown, that in the case of a magnetic field higher than 1000 G, the Paschen-Back regime for the hyperfine structure starts.

4. For the first time the N -resonance with $\sim 10\%$ contrast is detected in a $40\ \mu\text{m}$ cell filled with Rb and neon buffer gas (~ 100 torr).
5. For the first time the splitting of N -resonance into five components is observed in a thin cell filled with atomic vapors of Rb and buffer gas under influence of external magnetic fields (< 2200 G), and for magnetic fields higher than 1000 G the hyperfine Paschen-Back regime is identified.

The practical value of the work:

1. Narrow and high-contrast EIT-resonances formed in the column of atomic vapors of thickness less than 800 nm can be successfully applied in practical problems, which require miniaturization.
2. Using the EIT-resonance splitting in $30\ \mu\text{m}$ -cells filled with Rb, in strong magnetic fields, the formation of narrow EIT-resonances (showing a decrease in absorption of the probe radiation) over a wide frequency range of several GHz (shifted relative to the atomic transition at zero magnetic field) is possible.
3. Using the EIT-resonance splitting in $30\ \mu\text{m}$ -cells filled with Rb and buffer gas, in strong magnetic fields the formation of narrow N -type resonances (showing an increase in absorption of the probe radiation) over a wide frequency range of 1-4 GHz (shifted relative to the atomic transition at zero magnetic field) is possible.
4. Narrow N -type resonances, formed in the transmission spectrum of $40\ \mu\text{m}$ -Rb cell filled with a buffer gas, allow the measurement of both homogeneous and strongly inhomogeneous magnetic fields (with $40\ \mu\text{m}$ -spatial resolution) in the range of magnetic field B from 30 to 2200 gauss.

The statements of the thesis:

1. In the absorption spectra of the D_1 -line of Rb atoms placed inside nanocell with thickness $L = \lambda = 795$ nm under the radiation of two lasers, the EIT-resonance with high 40% contrast can be detected. EIT-resonance also can be recorded at extremely low thickness $L = \lambda/2 = 397$ nm, but its contrast is lower than that for the case of $L = \lambda$. The experimental results are in good agreement with theory. Compared to the nanocell with no buffer gas, addition of a buffer gas in the nanocell with rubidium vapor can significantly increase frequency tuning range of the EIT-resonance.
2. For the ^{85}Rb (in a $L = 30$ μm cell) under the influence of magnetic field up to 1700 G the EIT-resonance splits into five components. With the use of magnetic field higher than 1000 G the Paschen-Back regime for the hyperfine structure of ^{85}Rb starts.
3. In the absorption spectra of the D_1 -line of Rb atoms (with addition of ~ 100 torr neon buffer gas) placed inside nanocell with thickness $L = 40$ μm under the radiation of two lasers, the N -type resonance with 10% contrast can be detected.
4. In a $L = 40$ μm cell, with addition of ~ 100 torr neon buffer gas, for the ^{85}Rb under the influence of magnetic field up to 2100 G, the N -resonance splits into five components. With the use of magnetic field higher than 1000 G the Paschen-Back regime for the hyperfine structure of ^{85}Rb starts.

Approbation of the Thesis Statements

The statements of the thesis were presented and discussed at the seminars of the Institute for Physical Research of Armenian NAS; at the Laboratoire Interdisciplinaire Carnot de Bourgogne, UMR CNRS 6303 Université de Bourgogne, as well as reported at the conferences [15-21].

The main results of this dissertation have been published as articles in 12 peer reviewed journals and 7 abstracts in the conference Book of Abstracts represented in bibliography [3-21]. The thesis, which consists of introduction, four chapters and References, comprises 143 pages, contains 70 figures, 1 table and 150 references.

In **Chapter I** a literature overview of EIT effect is given. It is described in which type of systems EIT can be formed. The physical effect behind EIT technique is presented. The

theory of EIT effect is explained in details. Motivations and objectives of EIT-resonance observation in thick cells are presented. The theory of EIT in nanocell is described.

Also the experimental setup for studying EIT-resonance is presented. The technical parameters of all the devices are described. Construction of (nano- and micro-thin) cells containing atomic vapor is presented. Determination of the thickness of nanocell using a laser beam is shown.

The EIT-resonance formation in nanocell on thickness $L = \lambda$ is shown. The spectra of probe transition in nanocell on thickness $L = \lambda$ is compared with the theory, and the qualitative similarity is shown. The EIT-resonance formation in nanocell on lowest thickness $L = \lambda/2$ is shown for the first time. The spectra of probe transition in nanocell on thickness $L = \lambda/2$ is also compared with the theory, and the qualitative similarity is presented.

In **Chapter II** the behavior of EIT-resonance in magnetic field, for the D_1 -line of Rb atoms, is presented. The short discussion of the papers for this phenomena is given. It is shown, that due to B magnetic field the initial EIT-resonance splits into new 3 EIT-resonances (3 components) in case of ^{87}Rb D_1 -line. The diagram, showing all the possible Λ -systems is presented, and all components are discussed. It is shown, that for the case of ^{87}Rb D_1 -line, the three components behavior is depending on the frequency detuning of the couple radiation from the corresponding sublevels. It is shown, that for a magnetic field $B > 350$ G only two components are detectable, and for $B > 1200$ G only one of EIT components is seen. The experimental results for the isotope 87 of Rb are presented. The theoretical calculations for ^{87}Rb are made. Comparison of theoretical and experimental results is made and good agreement between them is presented.

Also the report on the experimental investigation of the behavior of the EIT-resonance in strong magnetic fields up to 1.7 kG with the use of the $30\ \mu\text{m}$ cell filled with an atomic rubidium vapor and a buffer gas (neon) is given. It is shown that the EIT-resonance in the Λ -system of the D_1 -line of ^{87}Rb atoms splits in a longitudinal magnetic field into five components, whose frequency behavior depends on the frequency configuration of the probe and coupling fields and the magnitude of the magnetic field. It is also shown that the study of the characteristics of the EIT-resonance components in high magnetic fields can readily reveal the onset of the Paschen-Back regime for the hyperfine structure of the atoms.

In **Chapter III** the N -type resonance formation in microcell is presented. Literature overview of N -type resonance is given. The experimental technique is described. The diagram of D_1 -line of ^{85}Rb for N -resonance formation is presented. Observation of narrow-band cascade N -resonance that forms in a Λ -system of rubidium atoms in cells with $L = 8$ mm and $40\text{-}90$ μm in the presence of neon gas at a pressure of 6, 20, 200, and 400 Torr is done. Detection of the N -resonance at a minimum vapor column thickness of 40 μm is presented. The dependence of N -resonance parameters on the angle between two lasers (which are used to form the resonance) is presented.

Also the report of simultaneous observation of the N - and EIT-resonance formation using multi-region cell filled with natural Rb and 150 Torr neon gas (containing micrometric-thin region with the thickness L varying in the range of 1 μm - 90 μm) is made. Simultaneous detection of the low-frequency beating signal and N -resonance is made, which allows the coupling laser frequency direct determination. Possible applications are addressed.

In **Chapter IV** the N -type resonance splitting in magnetic field using microcell with the addition of neon buffer gas is presented. Results of studies of behavior of N -resonance formed in a Λ -system of D_1 -line of atomic ^{87}Rb vapor in external magnetic fields in the range of $1\text{-}200$ G, with the use of microcell with the thickness of column of rubidium atoms $L = 50$ μm are presented. Considered theoretical model explains well the splitting of N -resonance into three components in the external magnetic field for the case of D_1 -line of ^{87}Rb .

The N -type resonance splitting on five components in D_1 -line of atomic ^{85}Rb in range of longitudinal magnetic field $1\text{-}2100$ G is presented. Experimental results are shown. The theoretical calculations of the frequency shift of N -resonance components are made. Comparison of theoretical and experimental results is made and good agreement between them is presented.

The N -resonance splitting on six components in D_1 -line of atomic ^{85}Rb in magnetic field is presented. The diagram, describing the Λ -systems involved in N -resonance components formation is shown. The experimental results and theoretical calculations are presented and the good agreement between them is achieved.

Physical mechanisms of N -type resonance formation is described.

Chapter 1

Formation of narrow resonances using the process of electromagnetically induced transparency (EIT) in cells of micrometer and nanometer thickness filled with Rb vapor

This chapter explores electromagnetically induced transparency (EIT) [30], a quantum coherence effect by which a strong laser is used to cancel absorption for a second, weaker laser propagating in the same medium. The phenomenon will be studied in nanometric cells with atomic vapor column length less or comparable with the resonant wavelengths.

1.1 Survey of EIT

1.1.1 Introduction to EIT

EIT [30] is a technique capable of drastically modifying a medium's optical properties near an atomic resonance when an electromagnetic field is applied [31]. As the name indicates, these properties include a transparency window at a normally highly absorbing resonance, but in addition to this, the dispersion properties of the medium are greatly enhanced. The essence

of the phenomenon is the possibility of propagation without absorption of a two-component strong field under the condition of two-photon resonance while each component would be strongly absorbed if propagates through the medium alone.

EIT was first predicted in 1989 in a theoretical work employing aspects of coherent

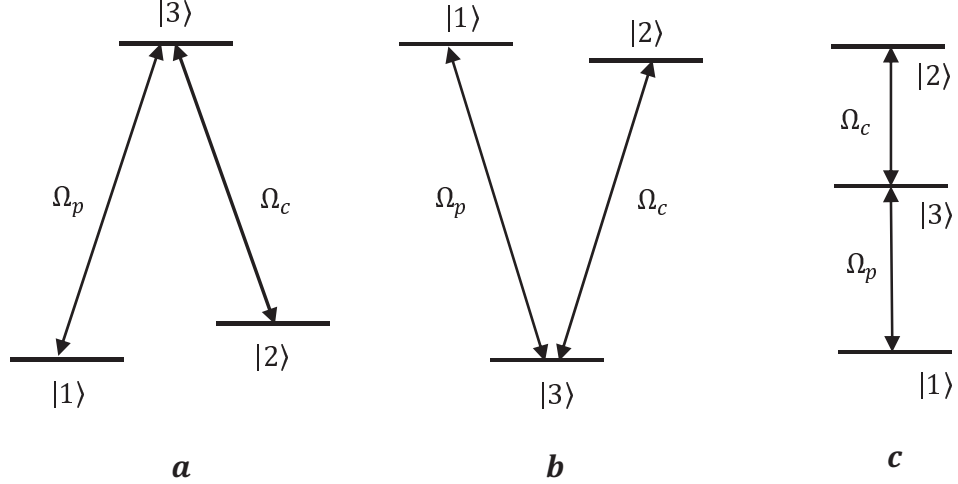


Figure 1.1: EIT capable three-level atomic or molecular systems coupled with two electromagnetic fields: a) Λ scheme; b) V scheme; c) Ξ (ladder) scheme. Each has two dipole allowed transitions and one dipole forbidden transition, with the only difference being the relative arrangement of the energy levels.

population trapping by Harris *et al.* [22]. An experimental realization of the effect was demonstrated shortly thereafter by Boller *et al.* [24] in strontium vapor, and by Field *et al.* [25] in lead vapor. Ever since the first few papers on EIT were published by Harris *et al.*, the number of papers mentioning the term have exponentially increased, and a wide range of phenomenon have been investigated that employ EIT. Some of the more important advances and potential applications are presented in Section 1.1.2.

EIT takes place in multilevel atomic and molecular systems interacting with coherent electromagnetic fields. The simplest system in which it is observed is a three-level atomic or molecular system (see Fig. 1.1) coupled to two laser fields in such a way that the laser driven transitions ($|1\rangle \rightarrow |3\rangle$ and $|2\rangle \rightarrow |3\rangle$) are dipole allowed while the third transition ($|1\rangle \rightarrow |2\rangle$), typically Zeeman or hyperfine, is dipole forbidden. A strong laser, what we term the coupling laser, is tuned to the resonant frequency of one transition. Then, a weak probe laser is scanned in frequency across the other transition. Under the two-photon (Raman) resonance the medium is observed to have the properties plotted in Fig. 1.2 in response to the probe beam. One can see that, the absorption of the probe field (tuned in resonance to the

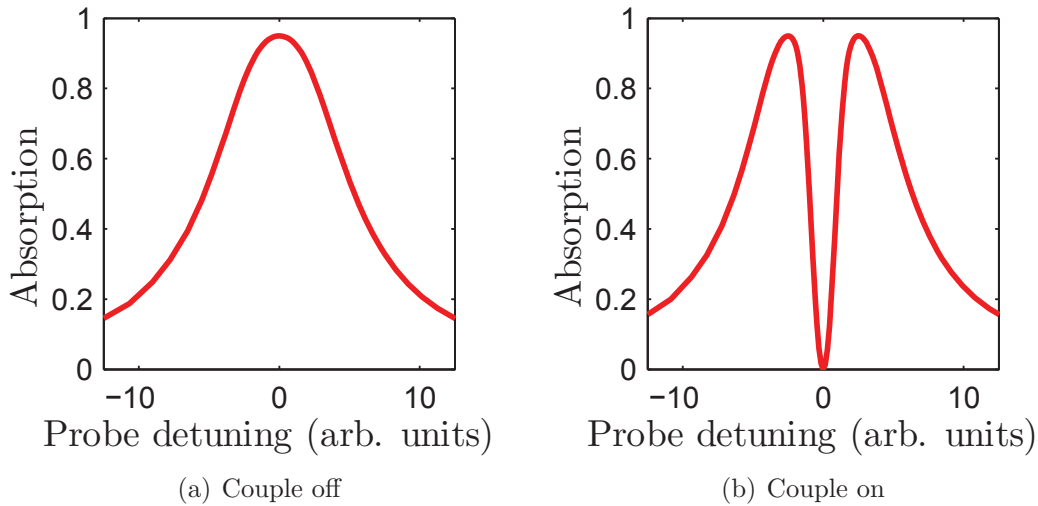


Figure 1.2: Simple EIT Plot. When the control laser is applied, the absorption peak splits revealing a transparency at what was the maximal absorption.

transition) is cancelled leading to an initially opaque medium being rendered transparent for the probe field. This effect is termed Electromagnetically Induced Transparency [30] owing to the fact that the transparency for the probe field is induced by the other electromagnetic field, coupling laser.

How does EIT work ? The underlying physics is as follows: Quantum mechanics requires that when multiple excitation pathways exist, interference between their probability amplitudes will occur [30]. This leads to one possible picture of EIT as an interference between transition pathways. Consider the three level Λ -system shown in Fig. 1.1. The atoms will primarily accumulate in the lowest energy state $|1\rangle$. Ordinarily, when one applies an electromagnetic field of frequency ω_{31} , atoms in the ground state can absorb energy and transit to state $|3\rangle$. But, when an electromagnetic field resonant with the $|2\rangle \rightarrow |3\rangle$ transition is also applied, there are now two transition pathways by which an atom can get from the ground state to the excited state: it can either transit in the same way as before, $|1\rangle \rightarrow |3\rangle$, or it can transit along $|1\rangle \rightarrow |3\rangle \rightarrow |2\rangle \rightarrow |3\rangle$. According to the Fano interference effect [23], a destructive atomic interference between these two alternative paths (i.e. one is directly induced by a resonant probe laser alone and the other is indirectly induced by the presence of both resonant lasers) associated with the same $|1\rangle \rightarrow |3\rangle$ transition can occur under appropriate conditions resulting in zero probe absorption at resonance. Under this situation, we say an initial opaque $|1\rangle \rightarrow |3\rangle$ transition has been made to be transparent to a probe laser beam by the presence of another strong control laser. This is an illustration of EIT in a so called

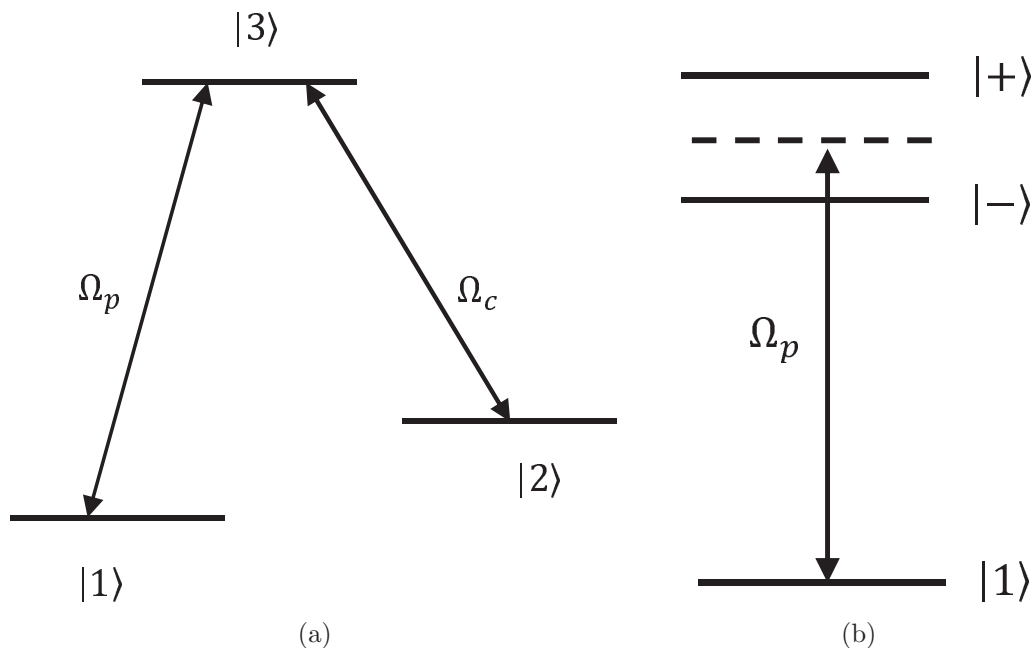


Figure 1.3: A three-state Λ atom interacting with two lasers in (a) a bare-state representation and (b) a dressed-state representation.

bare-state representation (Fig. 1.3(a)).

We can also view the same EIT process in a dressed-state representation. Through a coupling of a strong control laser applied between two bare states $|2\rangle$ and $|3\rangle$, a pair of interfering dressed transition amplitudes are induced for an atomic transition at a resonant probe frequency (i.e. $|1\rangle \rightarrow$ the middle of $|-\rangle$ and $|+\rangle$) (Fig. 1.3(b)). Therefore, a transition probability amplitude from $|1\rangle$ to $|3\rangle$ becomes equivalently a sum of those amplitudes from $|1\rangle$ to $|-\rangle$ and from $|1\rangle$ to $|+\rangle$. Since the latter two transition pathways both couple to the same final state $|3\rangle$, according to the Fano interference effect, a destructive interference between these two transition amplitudes of $|1\rangle \rightarrow |-\rangle$ and $|1\rangle \rightarrow |+\rangle$ can occur under suitable conditions and lead to zero or reduced induced absorption at a resonant probe frequency, thus inducing transparency of an opaque atomic $|1\rangle \rightarrow |3\rangle$ transition to a probe laser beam. EIT also has a particularly simple explanation in terms of so-called "dark" states that will be presented in Section 1.2.5.

1.1.2 Applications using EIT

As stated above EIT is a quantum interference effect in which coherence between atomic states is used to reduce the absorption in a window around an atomic resonance, while

simultaneously generating large dispersion and third order nonlinear susceptibilities within the induced transparency window. Ever since the first few papers on EIT were published by Harris *et al.*, EIT have developed into a very active research area. The number of papers mentioning the term have exponentially increased, and a wide range of phenomenon have been investigated that employ EIT. Some of them are briefly discussed in this subsection.

The induced transparency and a subsequently suggested modification of a refractive index [32–34], is ultimately responsible for the fascinating phenomenon of efficient mixing. Using EIT, Schmidt and Imamoglu [44] showed that it is theoretically possible to achieve resonantly-enhanced nonlinear (third-order) Kerr nonlinearities that are ten orders of magnitude larger than conventional Kerr nonlinearities. Apart from the EIT Kerr nonlinearity, there have been many advances in using EIT to provide more efficient low-light nonlinear optical media. The field of EIT enhanced nonlinear optics began in the mid 1990's only a few years after the first experiments in EIT. In 1995 Hemmer *et al.* demonstrated that EIT could be used to realize efficient phase conjugate effects [45], and in 1996 highly efficient nonlinear mixing was confirmed by Jain *et al.* [46], where an intense 425 nm beam was converted to a 293 nm beam with 40% efficiency. Hahn, King, and Harris [47] have applied EIT technique to generate sum-frequency radiation in the atomic zinc using two UV lasers source. Meanwhile, Hakuta, Marmet, and Stoicheff [48] have extended EIT technique by using dc electric field for a control laser field and have also shown in the atomic hydrogen a possibility of obtaining high conversion efficiency for second-harmonic generation of Lyman- α radiation.

EIT technique has promising applications not only in nonlinear optical processes but also in fields of laser physics. Conventional lasers require pumping more atomic population in upper states than in lower states in order to achieve a condition of population inversion for light amplification by stimulated emission of coherent radiation. Now, with EIT technique, a stimulated absorption of radiation from lower states may be reduced more effectively compared with a competing stimulated emission of radiation from upper states at a particular resonant light frequency, thus making possible for laser operating without the need to achieve population inversion in the atomic medium [35–40]. Three-state lasing without population inversion has been experimentally demonstrated in some atomic systems, e.g., Na [41] and Rb [42].

Another application of EIT is enhanced isotope discrimination. Laser isotope separation technique is based on a fact that different isotopes of an element absorb light at different frequencies. A particular isotope is selectively excited by means of a monochromatic laser tuned to a resonant atomic transition, thus discriminated from the other isotope species. Kasapi [43] has proposed and demonstrated an enhanced laser isotope separation process between two isotopes of the atomic lead using EIT technique. This method combines a resonant cancellation of induced absorption via EIT effect in one isotope with an enhanced stimulated absorption for the same probe laser in the other isotope through ac Stark effect by adjusting a control laser strength to supply enhanced separation signals in photoabsorption spectrum. Compared with a conventional isotope discrimination method using only one resonantly-tuned laser, an enhanced separation signal using EIT technique is about one order of magnitude higher.

EIT has also been applied to various precision measurement tasks such as magnetometry [49–52], spectroscopy [53,54], in atomic clocks and improving frequency standards [55,56]. The value of EIT for precision measurement is due to the fact that a very narrow (subnatural linewidth) transparency resonance can be created. For example, an EIT linewidth with a full width at half maximum (FWHM) of 20 – 100 Hz is not uncommon [55,57], making EIT a very sensitive tool for the Raman detuning and any environmental changes which affect it.

Alongside the modification of the absorption by EIT is the concomitant modification of the dispersion. This is what makes EIT of such interest, the resulting dispersion has very large slope for frequencies near the center of the transparency window; normally such steep dispersion would be coincident with significant absorption. Such as the steep dispersion can lead to extremely slow group velocities for pulses with frequencies near the EIT transparency resonance [58, 59]. Several groups used the steep dispersion of EIT to observe slow light propagation in a variety of media, including hot atomic gases and atomic Bose-Einstein condensates. In 1999 a group at Harvard reported an experiment in which the group velocity of a pulse of light traveling through an ultracold gas had been reduced to a mere 17 m/s [63], a reduction by a factor of 10^7 from the speed of light in vacuum. Some months later, a second group (also at Harvard) reported similarly dramatic results (group velocities of about 90 m/s), this time in a hot gas [64]. Group velocities as slow as 8 m/s were induced by

Budker *et al.* [62]. By 2001, the methods used to slow light have been extended "to stop" a light pulse [65] and store it in an atomic quantum state for a short time before coherently retrieving the pulse [69–71] using ideas developed by Fleischhauer *et al.* [66] (See also [68]). The phase information of the stopped light was stored in the quantum state of the atomic polarization, from which it could be extracted by slowly turning on a second laser field. This fully reversible storage process remains one of the most important potential applications of EIT, as it permits the transmission and storage of quantum information. Storage times of up to ten second for light pulses in EIT media are achieved by Longdell *et al.* [72].

The technique of EIT has been used in coherently prepared media to create single photon states, store these photons, and then retrieve them while preserving their quantum properties [73].

There are many other applications using EIT. For many more see the review articles by Fleischhauer *et al.* [1] and by Marangos [29].

1.1.3 Physical constraints on EIT

A physical effect behind EIT technique is a destructive atomic interference between alternative laser-induced atomic transition amplitudes (or atomic coherences) for a given transition process. Any dephasing of these alternative atomic coherences can diminish and suppress an effective destructive interference, thus making EIT effect become non-observable.

We review some of well-known and frequently discussed physical constraints to EIT which can prevent an effective atomic interference effect in real atomic systems. For the following discussion, we consider a three-state Λ -type atomic system. Physical mechanisms for interrupting and destroying coherent phase relationships of laser induced atomic coherences pertinent to EIT can be summarized as follows:

- Spontaneous decay of state $|2\rangle$ on a two-photon (Raman) transition;
- Collisional damping;
- Doppler broadening;
- Additional non-interfering photo-absorption transition processes;
- Closely spaced hyperfine or Zeeman sublevels;
- Finite linewidth of a coupling laser applied on a $|2\rangle \rightarrow |3\rangle$ transition.

Due to these coherence-dephasing processes, one needs to select suitable atomic states (e.g. metastable or long-lived state for state $|2\rangle$) and appropriate laser sources (e.g. pulsed or CW lasers with single- or multi-mode) with laser system parameters (monochromaticity and peak power value) in order to overcome coherence-degrading effects due to above inherent homogeneous and inhomogeneous linewidths associated with atomic media, laser sources and experimental conditions (e.g. temperature, pressure due to collisions with a buffer gas or walls of a vapor cell, and atom number density).

For a quantitative description of the EIT-resonance, one can use the following expression [74]

$$\frac{\alpha(\Omega_c)}{\alpha(0)} = \frac{K}{1 + \Omega_c^2/4\Gamma_{21}\gamma_N}, \quad (1.1)$$

where $\alpha(\Omega_c)$ is the absorption at the probe radiation frequency ω_p (at which the EIT-resonance is detected) in the presence of the coupling radiation, and $\alpha(0)$ is that in the absence of the coupling radiation. γ_N is the natural linewidth (6 MHz for Rb atoms) of the level, Ω_c is the Rabi frequency for the coupling field, and Γ_{21} is the dephasing rate of coherence. For a given isotope of alkali metal K is a constant and for the ^{85}Rb it is $K \approx 29$. Fig. 1.4 shows the ratio of $\alpha(\Omega_c)$ and $\alpha(0)$. As is seen from the figure, the decrease of $\alpha(\Omega_c)$ results in a better contrast for the EIT-resonance, and the maximum contrast will be observed, when the $\alpha(\Omega_c) = 0$. It is seen from Eq. (1.1) that in case where Ω_c tends to infinity (the coupling laser intensity become very high) or when Γ_{21} tends to zero, the ratio $\alpha(\Omega_c)/\alpha(0)$ tends to zero, i.e. the high contrast EIT-resonance is formed. In case where Γ_{21} tends to infinity the ratio $\alpha(\Omega_c)/\alpha(0)$ increases which leads to the absence of EIT-resonance. Thus for the formation of EIT-resonance the following condition is needed

$$\Omega_c^2 \gg 4\Gamma_{21}\gamma_N. \quad (1.2)$$

Consequently, the EIT process is a nonlinear process and the coupling field intensity I_c and the ground state decay rate Γ_{21} are relevant parameters for EIT. In ordinary size cells Γ_{21} is of the order of 10-20 kHz and is defined by the inverse of time of flight through the diameter of laser beam $t = D/V$, and $\gamma_N \sim 6$ MHz. Consequently in order to satisfy EIT-resonance condition few mW/cm² intensity of coupling laser is sufficient, which can be easily achieved

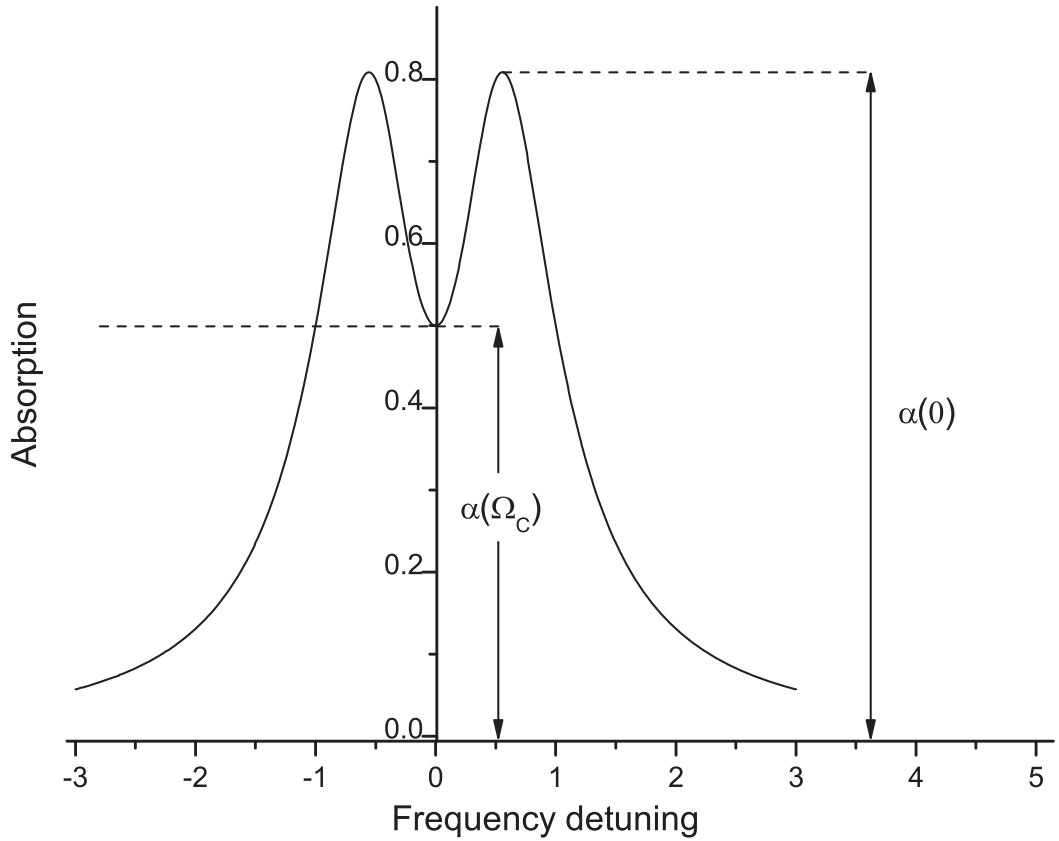


Figure 1.4: . The $\alpha(\Omega_C)$ and $\alpha(0)$ are shown for the case where Δ_C and Δ_P are equal to zero.

experimentally. For the linewidth γ_{EIT} the following expression takes place: $\gamma_{EIT} \approx 2\Gamma_{21} + \Omega_C^2/\gamma_N$ [78]. It must be pointed out that Eq. 1.1 shows the measure of the ratio $\alpha(\Omega_C)/\alpha(0)$ only for cases when Δ_C and Δ_P both are equal to zero.

1.2 EIT Hamiltonian

To properly characterize EIT, we will employ a semiclassical approach. The atoms are treated as fully quantum objects, while all fields are treated as classical vector fields. There are fully quantum derivations of EIT [66], but we will not discuss them in this thesis, as the semiclassical treatment makes excellent predictions for atom-field interactions [67].

1.2.1 Outline

There are three energy level configurations for three level atoms that can demonstrate EIT, shown in Fig. 1.1. While all three systems demonstrate EIT, we will derive EIT for a three

level Λ -atom, as the effects are diminished in cascade and V-systems due to high decay rates from $|2\rangle$, which shortens the coherence lifetime. The Λ -atom's $|2\rangle$ state is a metastable state with greatly reduced decays and longer coherence lifetimes.

We are ultimately interested in the optical properties of the medium, specifically the dispersion and absorption of the probe laser. These characteristics are described to first order by the frequency dependent complex valued linear electric susceptibility, which is defined by

$$\mathbf{P} = \epsilon_0 \chi \mathbf{E}, \quad (1.3)$$

where \mathbf{P} is the dielectric polarization of the medium, \mathbf{E} is the electric field, and ϵ_0 is the permittivity of free space. Knowledge of χ completely determines the material properties we are seeking. Note that \mathbf{P} , \mathbf{E} and χ are all macroscopic quantities. However, in order to find χ , we need to consider individual atoms.

We first need a description of how the quantum mechanical atom behaves in the applied field. For this we construct a Hamiltonian (H_0) describing the three level atom, and approximate the field's effects as a dipole perturbation (H_1), which is given as the energy of the dipole moment operator (d). The full Hamiltonian ($H = H_0 + H_1$) can be massaged with some approximations and transformations to a more agreeable form, what we term the EIT Hamiltonian (H_{EIT}).

The EIT Hamiltonian describes a single atom interacting with the external electromagnetic field, but in our system we have an ensemble of atoms. It is therefore natural to transit from describing the system with single atom wave functions, to describing it with density operators (ρ), which model the state of a population of atoms. From this description of the medium, we can generate an expression of the macroscopic polarization in terms of the expectation of the dipole moment operators ($\mathbf{P} = N\langle \mathbf{d} \rangle$, where N is the density of atoms). We then have the relation $N\langle \mathbf{d} \rangle = \epsilon_0 \chi \mathbf{E}$, from which we can solve for χ .

1.2.2 Deriving the EIT Hamiltonian

The system under investigation is a three level Λ -atom, consisting of the eigenstates $|1\rangle$; $|2\rangle$ and $|3\rangle$, with corresponding eigenvalue energies $\hbar\omega_n$. We have labeled the states in order of

increasing energy, where $|1\rangle$ is a stable ground state, $|2\rangle$ is a metastable state, and both are coupled to the excited state $|3\rangle$.

We will write the Hamiltonian in the form

$$H = H_0 + H_1, \quad (1.4)$$

where H_0 is the Hamiltonian describing the free atom without external fields, and H_1 is the perturbation due to the applied electric field. As we are making the assumption that we only have three states, we can form a complete orthonormal basis consisting of the three states $|n\rangle$, each with a corresponding eigenvalue of $\hbar\omega_n$. Completeness and orthonormality give:

$$\sum_n |n\rangle\langle n| = \mathbb{1}, \quad \langle n|m\rangle = \delta_{nm}. \quad (1.5)$$

Employing these eigenvectors and the eigenvalues, we may write the unperturbed Hamiltonian in terms of states n as:

$$H_0 = \left(\sum_n |n\rangle\langle n| \right) H_0 \left(\sum_n |n\rangle\langle n| \right) = \begin{pmatrix} \hbar\omega_1 & 0 & 0 \\ 0 & \hbar\omega_2 & 0 \\ 0 & 0 & \hbar\omega_3 \end{pmatrix}. \quad (1.6)$$

We will now be perturbing H_0 with an electric field. The $|2\rangle \rightarrow |3\rangle$ transition is driven by a strong control field of amplitude E_c and frequency ω_c , while the $|1\rangle \rightarrow |3\rangle$ transition is driven by a weak probe field of amplitude E_p and frequency ω_p . The $|1\rangle \rightarrow |2\rangle$ transition is assumed to be a dipole forbidden transition. All other energy levels are assumed to be sufficiently off resonance for other transitions to be negligible.

The applied electric field can thus be written as

$$E = E_p \cos(\omega_p t - \mathbf{k}_p \mathbf{r}) + E_c \cos(\omega_c t - \mathbf{k}_c \mathbf{r}), \quad (1.7)$$

where \mathbf{k} are the wave vectors associated with ω . For incident light with wavelengths λ much longer than the effective radius r of the atom, $\lambda \gg r$, we have $kr \ll 1$ and the electric field

becomes

$$E = E_p \cos(\omega_p t) + E_c \cos(\omega_c t). \quad (1.8)$$

The energy of this perturbation will be given by

$$H_1 = -q\mathbf{E} \cdot \mathbf{r}, \quad (1.9)$$

where q is the electron charge, \mathbf{E} is the classical vector valued electric field, and \mathbf{r} is the position operator. The term $-q\mathbf{E} \cdot \mathbf{r}$, is simply the energy associated with a dipole of charge q and separation vector \mathbf{r} in the applied field \mathbf{E} . Thus, the assumption $\lambda \gg r$ is known as the dipole approximation.

Assuming the dipole is aligned with the electric field, we have:

$$H_1 = -qE \cdot r. \quad (1.10)$$

We now will define the dipole moment operator as $d = qr$, and the elements of the operator in the eigenbasis of H_0 by $d_{nm} = d_{mn}^* = \langle n | m \rangle$. The perturbation becomes

$$H_1 = -dE = -\left(\sum_n |n\rangle\langle n|\right)d\left(\sum_n |n\rangle\langle n|\right)E = -E \begin{pmatrix} d_{11} & d_{12} & d_{13} \\ d_{21} & d_{22} & d_{23} \\ d_{31} & d_{32} & d_{33} \end{pmatrix}. \quad (1.11)$$

To simplify the dipole moment operator, we assume $d_{12} = d_{21} = 0$, consistent with the forbidden $|1\rangle \rightarrow |2\rangle$ transition. Additionally we assume $d_{ii} = 0$, removing all the diagonal elements. This amounts to assume that the atoms have no permanent dipole moments, which is true for atoms with spherically symmetric wave functions [91]. This assumption holds for a variety of atomic materials, including rubidium, our species of interest. Under these assumptions, we have:

$$H_1 = -E \begin{pmatrix} 0 & 0 & d_{13} \\ 0 & 0 & d_{23} \\ d_{31} & d_{32} & 0 \end{pmatrix}. \quad (1.12)$$

1.2.3 Rotating Wave Approximation

To find the EIT Hamiltonian, we will invoke the rotating wave approximation, which neglects any rapidly oscillating terms in the Hamiltonian. To reveal these terms, we will transform into the interaction picture using the time evolution operator:

$$U(t) = e^{iH_0t/\hbar} = \begin{pmatrix} e^{i\omega_1 t} & 0 & 0 \\ 0 & e^{i\omega_2 t} & 0 \\ 0 & 0 & e^{i\omega_3 t} \end{pmatrix} \quad (1.13)$$

Applying this transformation to H_1 gives

$$UH_1U^\dagger = -E \begin{pmatrix} 0 & 0 & d_{13}e^{i(\omega_1-\omega_3)t} \\ 0 & 0 & d_{23}e^{i(\omega_2-\omega_3)t} \\ d_{31}e^{i(\omega_3-\omega_1)t} & d_{32}e^{i(\omega_3-\omega_2)t} & 0 \end{pmatrix}, \quad (1.14)$$

where dagger denotes hermitian conjugate. We express the electric field in the complex notation

$$E = E_p \cos \omega_p t + E_c \cos \omega_c t = \frac{E_p}{2}(e^{i\omega_p t} + e^{-i\omega_p t}) + \frac{E_c}{2}(e^{i\omega_c t} + e^{-i\omega_c t}). \quad (1.15)$$

Now we apply the rotating wave approximation, which amounts to assume that any quickly oscillating term will be averaged out on the time scale of observation. Recall that ω_p is near resonance with the $\omega_3 \rightarrow \omega_1$ transition, so the difference $\omega_3 - \omega_1 - \omega_p$ will be small, and any exponentials with these terms will remain since they oscillate slowly. However, terms containing the sum $\omega_3 - \omega_1 + \omega_p$ will be large, and so these quickly oscillating terms can be dropped in the rotating wave approximation. Similar reasoning is applied to all terms. So neglecting all terms with sums in the exponents as rapidly varying, we obtain for the non-zero

matrix elements

$$\begin{aligned}
(UH_1U^\dagger)_{13} &= -\frac{1}{2}E_p d_{13} e^{i(\omega_1 - \omega_3 + \omega_p)t} \\
(UH_1U^\dagger)_{23} &= -\frac{1}{2}E_c d_{23} e^{i(\omega_2 - \omega_3 + \omega_c)t} \\
(UH_1U^\dagger)_{31} &= -\frac{1}{2}E_p d_{31} e^{i(\omega_3 - \omega_1 - \omega_p)t} \\
(UH_1U^\dagger)_{32} &= -\frac{1}{2}E_c d_{32} e^{i(\omega_3 - \omega_2 - \omega_c)t}
\end{aligned} \tag{1.16}$$

Reversing the transformation to move back into the Schrödinger picture, we find the EIT Hamiltonian

$$H_1 = -\frac{1}{2} \begin{pmatrix} 0 & 0 & d_{13}E_p e^{i\omega_p t} \\ 0 & 0 & d_{23}E_c e^{i\omega_c t} \\ d_{31}E_p e^{-i\omega_p t} & d_{32}E_c e^{-i\omega_c t} & 0 \end{pmatrix}. \tag{1.17}$$

We write the Hamiltonian in terms of the Rabi frequencies. First, let us separate the dipole operator into magnitude and phase:

$$\begin{aligned}
d_{13} &= d_{31}^* = |d_{13}| e^{i\varphi_p}, \\
d_{23} &= d_{32}^* = |d_{23}| e^{i\varphi_c}.
\end{aligned} \tag{1.18}$$

Now define the Rabi frequencies

$$\begin{aligned}
\Omega_p &= \frac{E_p |d_{13}|}{\hbar}, \\
\Omega_c &= \frac{E_c |d_{23}|}{\hbar}.
\end{aligned} \tag{1.19}$$

This gives us

$$H_1 = -\frac{\hbar}{2} \begin{pmatrix} 0 & 0 & \Omega_p e^{i\varphi_p} e^{i\omega_p t} \\ 0 & 0 & \Omega_c e^{i\varphi_c} e^{i\omega_c t} \\ \Omega_p e^{-i\varphi_p} e^{-i\omega_p t} & \Omega_c e^{-i\varphi_c} e^{-i\omega_c t} & 0 \end{pmatrix}. \tag{1.20}$$

Combining H_0 and H_1 , we have the complete EIT Hamiltonian

$$H_{EIT} = \frac{\hbar}{2} \begin{pmatrix} 2\omega_1 & 0 & -\Omega_p e^{i\varphi_p} e^{i\omega_p t} \\ 0 & 2\omega_2 & -\Omega_c e^{i\varphi_c} e^{i\omega_c t} \\ -\Omega_p e^{-i\varphi_p} e^{-i\omega_p t} & -\Omega_c e^{-i\varphi_c} e^{-i\omega_c t} & 2\omega_3 \end{pmatrix}. \quad (1.21)$$

1.2.4 Corotating frame

While the previous transformation makes clear the simplifications of the rotating wave approximation, the next transformation we apply is constructed to remove all time dependence from the Hamiltonian, as well as the phase of the dipole moment operator. This new basis is known as the rotating basis, which we will denote with tilde's symbol " \sim " on the transformed elements. The new basis $|\tilde{n}\rangle$ is related to the Schrödinger picture by the transformation $|\tilde{n}\rangle = \tilde{U}|n\rangle$ where \tilde{U} is given by

$$\tilde{U}(t) = \begin{pmatrix} e^{-i\varphi_p} e^{-i\omega_p t} & 0 & 0 \\ 0 & e^{-i\varphi_c} e^{-i\omega_c t} & 0 \\ 0 & 0 & 1 \end{pmatrix}. \quad (1.22)$$

By applying the matrix $\tilde{U}(t)$ to the left of both sides of the time-dependent Schrödinger equation we have

$$\begin{aligned} i\hbar \tilde{U}(t) \frac{\partial}{\partial t} |n\rangle &= \tilde{U}(t) H_{EIT} |n\rangle, \\ i\hbar \left(\frac{\partial}{\partial t} \tilde{U}(t) |n\rangle - \frac{\partial \tilde{U}(t)}{\partial t} |n\rangle \right) &= \tilde{U} H_{EIT} \tilde{U}^\dagger(t) \tilde{U}(t) |n\rangle, \\ i\hbar \frac{\partial}{\partial t} \tilde{U}(t) |n\rangle &= \left(i\hbar \frac{\partial \tilde{U}(t)}{\partial t} \tilde{U}^\dagger(t) + \tilde{U}(t) H_{EIT} \tilde{U}^\dagger(t) \right) \tilde{U}(t) |n\rangle, \\ i\hbar \frac{\partial}{\partial t} |\tilde{n}\rangle &= \left(i\hbar \frac{\partial \tilde{U}(t)}{\partial t} \tilde{U}^\dagger(t) + \tilde{U}(t) H_{EIT} \tilde{U}^\dagger(t) \right) |\tilde{n}\rangle. \end{aligned} \quad (1.23)$$

Thus in the new basis $|\tilde{n}\rangle = \tilde{U}(t)|n\rangle$ the transformed Hamiltonian also satisfies the Schrödinger equation:

$$i\hbar \frac{\partial}{\partial t} |\tilde{n}\rangle = \tilde{H}_{EIT} |\tilde{n}\rangle, \quad (1.24)$$

with

$$\tilde{H}_{EIT} = i\hbar \frac{\partial \tilde{U}}{\partial t} \tilde{U}^\dagger + \tilde{U} H_{EIT} \tilde{U}^\dagger. \quad (1.25)$$

The use of transformation (1.22) leads to a simplified Hamiltonian \tilde{H}_{EIT} , that is

$$\begin{aligned} \tilde{H}_{EIT} &= i\hbar \frac{\partial \tilde{U}}{\partial t} \tilde{U}^\dagger + \tilde{U} H_{EIT} \tilde{U}^\dagger \\ &= \frac{\hbar}{2} \begin{bmatrix} 2\omega_p & 0 & 0 \\ 0 & 2\omega_c & 0 \\ 0 & 0 & 0 \end{bmatrix} + \frac{\hbar}{2} \begin{bmatrix} 2\omega_1 & 0 & -\Omega_p \\ 0 & 2\omega_2 & -\Omega_c \\ -\Omega_p & -\Omega_c & 2\omega_3 \end{bmatrix}, \end{aligned} \quad (1.26)$$

$$\tilde{H}_{EIT} = \frac{\hbar}{2} \begin{bmatrix} 2(\omega_1 + \omega_p) & 0 & -\Omega_p \\ 0 & 2(\omega_2 + \omega_c) & -\Omega_c \\ -\Omega_p & -\Omega_c & 2\omega_3 \end{bmatrix}. \quad (1.27)$$

\tilde{H}_{EIT} no longer contains any time dependent terms and can be rewritten as

$$\tilde{H}_{EIT} = -(\omega_1 + \omega_p)\mathbb{1} + \frac{\hbar}{2} \begin{bmatrix} 0 & 0 & -\Omega_p \\ 0 & 2(\omega_2 + \omega_c - \omega_1 - \omega_p) & -\Omega_c \\ -\Omega_p & -\Omega_c & 2(\omega_3 - \omega_1 - \omega_p) \end{bmatrix}. \quad (1.28)$$

As $-(\omega_1 + \omega_p)\mathbb{1}$ is not physically relevant, it can be dropped out from Eq. 1.28. Thus, one arrives at

$$\tilde{H}_{EIT} = \frac{\hbar}{2} \begin{bmatrix} 0 & 0 & -\Omega_p \\ 0 & 2(\omega_2 + \omega_c - \omega_1 - \omega_p) & -\Omega_c \\ -\Omega_p & -\Omega_c & 2(\omega_3 - \omega_1 - \omega_p) \end{bmatrix}. \quad (1.29)$$

Defining the one-photon laser detunings $\Delta_p = \omega_3 - \omega_1 - \omega_p$ and $\Delta_c = \omega_3 - \omega_2 - \omega_c$, and the two-photon detuning $\delta = \Delta_p - \Delta_c$, we obtain

$$\tilde{H}_{EIT} = -\frac{\hbar}{2} \begin{bmatrix} 0 & 0 & \Omega_p \\ 0 & -2\delta & \Omega_c \\ \Omega_p & \Omega_c & -2\Delta_p \end{bmatrix}. \quad (1.30)$$

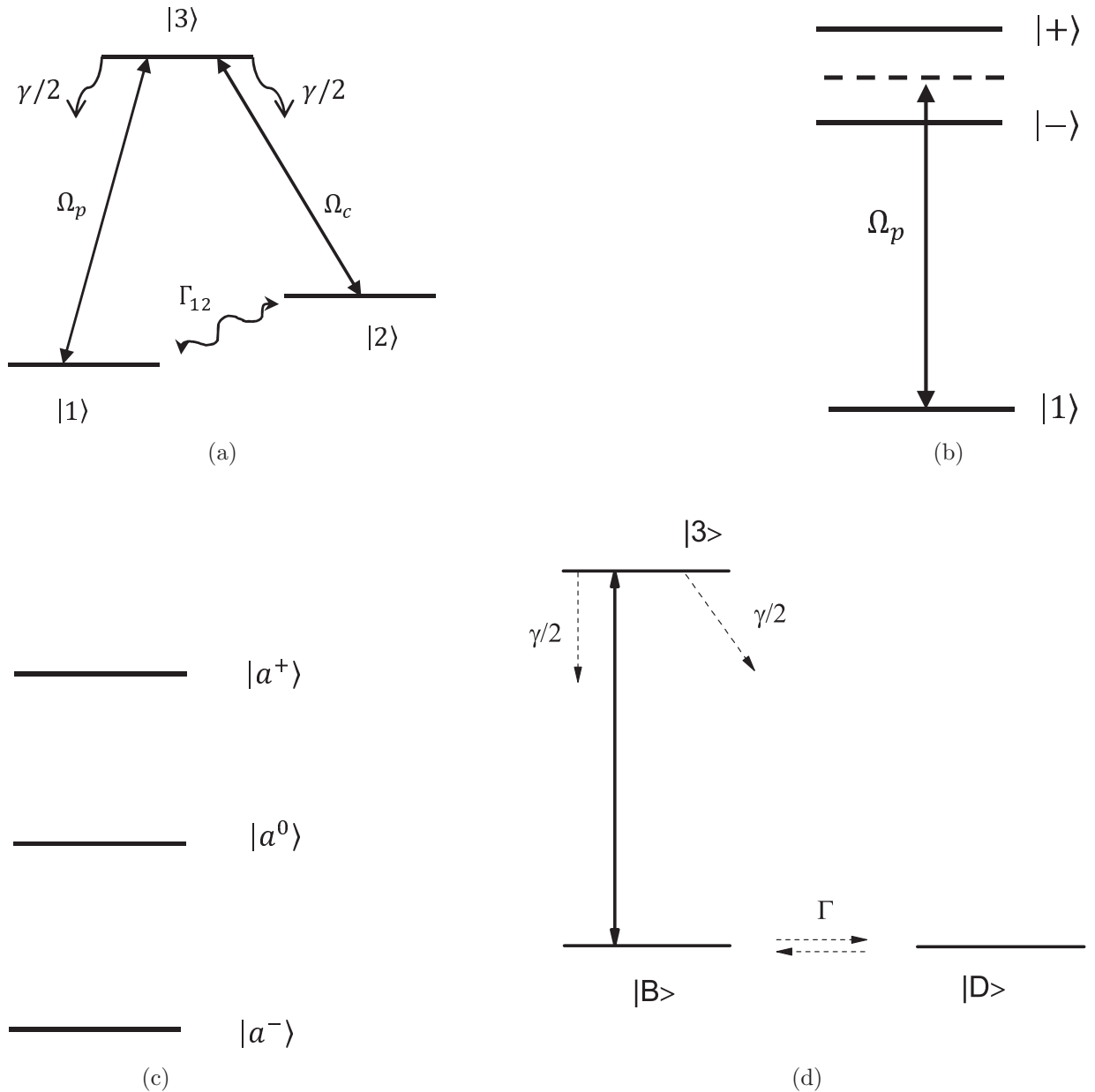


Figure 1.5: The EIT atom under various unitary transformations into dressed states. (a) The bare, unperturbed basis. (b) The dressed basis producing two split excited states. (c) The dressed basis in which the entire Hamiltonian is diagonalized. The center state is the "dark state," which cannot decay or absorb photons; no states are coupled by electric fields. (d) The dark/light state basis. One state, the dark state, decouples from the excited state, while the light state couples more strongly.

1.2.5 Analysis in terms of dressed and dark states

Many phenomena that seem surprising when presented in terms of interactions between lasers and the "bare" (ie. unperturbed) atomic states have simple interpretations under a change of basis. The underlying physics of EIT can be explained in terms of so-called "dressed states". The dressed states are simply superpositions of the bare states and typically correspond to

the eigenvectors of the full ($H_0 + H_1$) Hamiltonian.

On two-photon resonance ($\Delta_p = \Delta_c = \Delta$, or $\delta = 0$) the diagonalisation of Eq. (1.30) gives the following eigenstates for the coupled atom-light system in terms of the atomic bare states [1]

$$|a^+\rangle = \sin\theta \sin\psi|1\rangle + \cos\psi|3\rangle + \cos\theta \sin\psi|2\rangle, \quad (1.31a)$$

$$|a^-\rangle = \sin\theta \cos\psi|1\rangle - \sin\psi|3\rangle + \cos\theta \cos\psi|2\rangle, \quad (1.31b)$$

$$|a^0\rangle = \cos\theta|1\rangle - \sin\theta|2\rangle. \quad (1.31c)$$

with the mixing angles defined as $\tan\theta = \Omega_p/\Omega_s$, $\tan 2\psi = \Omega/\Delta$, and $\Omega = \sqrt{\Omega_p^2 + \Omega_c^2}$ being the generalized Rabi frequency. The level diagram for this case is presented in Fig. 1.5(c).

The corresponding eigenvalues read

$$\lambda_{a^+} = \frac{\hbar}{2} \left(\Delta - \sqrt{\Omega^2 + \Delta^2} \right), \quad (1.32a)$$

$$\lambda_{a^-} = \frac{\hbar}{2} \left(\Delta + \sqrt{\Omega^2 + \Delta^2} \right), \quad (1.32b)$$

$$\lambda_{a^0} = 0. \quad (1.32c)$$

The interesting physics in the dressed state picture is that the eigenstate $|a^0\rangle$ contains no contribution from the excited state $|3\rangle$. Moreover, $|a^0\rangle$ does not interact with $|3\rangle$, i.e., $\langle 3|H_{EIT}|a^0\rangle = 0$ vanishes, since $|a^0\rangle$ is one of the eigenvectors of the system. This means that no interaction can drive the transition between $|a^0\rangle$ and $|3\rangle$, and an atom has no probability of absorbing or emitting a photon when being in $|a^0\rangle$. So medium physically becomes transparent to the probe beam when its initial state is prepared to be $|a^0\rangle$. For this reason, $|a^0\rangle$ is often called the "dark" or "trapped" state.

Note that state $|a^0\rangle$ decouples from the other two eigenstates entirely, and so an atom in $|a^0\rangle$ cannot evolve into either of the other states. It is possible to populate the dark state by optical pumping: population from $|3\rangle$ can decay via spontaneous emission into either of eigenstates. However, population in $|a^0\rangle$ cannot be re-excited into $|3\rangle$, leading to a net accumulating in $|a^0\rangle$. This process is one of the methods behind coherent population trapping (CPT) [75].

The important point to draw from Eqs. 1.31 is that, in the limit of a strong coupling laser and a weak probe laser, i.e. $\Omega_p \ll \Omega_c$ (usual situation in many EIT schemes), $\sin \theta \rightarrow 0$ and $\cos \theta \rightarrow 1$. This leads to the new eigenstates

$$|+\rangle = \sin \psi |2\rangle + \cos \psi |3\rangle, \quad (1.33a)$$

$$|-\rangle = \cos \psi |2\rangle - \sin \psi |3\rangle, \quad (1.33b)$$

$$|a^0\rangle = |1\rangle. \quad (1.33c)$$

If now the probe laser comes into resonance, i.e. $\Delta = 0$, one has $\psi = \pi/4$ and $\tan \psi \rightarrow 1$, and then the states are

$$\begin{aligned} |+\rangle &= \frac{1}{\sqrt{2}} (|2\rangle + |3\rangle), \\ |-\rangle &= \frac{1}{\sqrt{2}} (|2\rangle - |3\rangle), \\ |a^0\rangle &= |1\rangle. \end{aligned} \quad (1.34)$$

The dressed atom picture for this case is shown in Fig. 1.5(b). One sees a splitting of the new eigenstates by Ω due the atom light interaction. This splitting can be detected by using the probe transition. The probe light couples only to the $|3\rangle$ part of $|+\rangle$ and $|-\rangle$ which have opposite signs in these states. This causes Fano-type interference [23] of the two excitation paths from $|1\rangle$ to $|+\rangle$ and $|1\rangle$ to $|-\rangle$, leading to zero absorption on the probe transition from $|1\rangle$ to $|3\rangle$.

As one can see from Eqs. (1.34), in the case considered ($\Omega_p \ll \Omega_c$ and all lasers on resonance), the ground state $|1\rangle$ coincides with the dark state $|a^0\rangle$ from which excitation cannot occur. So, EIT offers an alternative way of populating the dark state. If one ensures an adiabatic evolution of the fields [76], then the state $|1\rangle$ will evolve into the dark state and decouple from the other states. Unlike the case of CPT, where the time scale for population trapping in the dark state is several radiative lifetimes, in the case of EIT the effect is established (within a single atom) in a time of the order of $1/\Omega_c$, which is generally much faster.

Ultimately, EIT can be explained in terms in terms of the coupled ("bright" $|B\rangle$) and

decoupled ("dark" $|D\rangle$) superposition states [83, 84] of the lower levels $|1\rangle$ and $|2\rangle$:

$$\begin{aligned} |3\rangle &= |3\rangle, \\ |B\rangle &= \frac{1}{\Omega} (\Omega_p^*|1\rangle + \Omega_c^*|2\rangle), \\ |D\rangle &= \frac{1}{\Omega} (\Omega_c|1\rangle - \Omega_p|2\rangle), \end{aligned} \quad (1.35)$$

that in the case of pulses read

$$\begin{aligned} |B\rangle(t) &= \frac{1}{\Omega} e^{-i\omega_1 t} (\Omega_p^*|1\rangle + e^{-i\omega_{21} t} \Omega_c^*|2\rangle) \\ |D\rangle(t) &= \frac{1}{\Omega} e^{-i\omega_1 t} (\Omega_c|1\rangle - e^{-i\omega_{21} t} \Omega_p|2\rangle). \end{aligned} \quad (1.36)$$

In the rotating wave approximation the electric dipole operator coupling ground and excited states is

$$\begin{aligned} V_{dip} &= \frac{\hbar\Omega_p}{2} \exp(-i\omega_p t - i\varphi_p) |3\rangle\langle 1| + c.c. \\ &+ \frac{\hbar\Omega_c}{2} \exp(-i\omega_c t - i\varphi_c) |3\rangle\langle 2| + c.c. \end{aligned} \quad (1.37)$$

so that with $\Delta\varphi = \varphi_1 - \varphi_2$ the transition dipole matrix elements into the excited state are

$$\begin{aligned} \langle 3|V_{dip}|B\rangle &= \frac{\hbar}{2\Omega} \exp[-i(\omega_1 + \omega_p)t - i\varphi_p] \\ &\times (|\Omega_p|^2 + |\Omega_c|^2 \exp[i\delta t + i\Delta\varphi]) \end{aligned} \quad (1.38)$$

$$\begin{aligned} \langle 3|V_{dip}|D\rangle &= \frac{\hbar\Omega_p\Omega_c}{2\Omega} \exp[-i(\omega_1 + \omega_p)t - i\varphi_p] \\ &\times (1 - \exp[i\delta t + i\Delta\varphi]). \end{aligned} \quad (1.39)$$

When the difference frequency of the two light fields matches the ground state splitting ($\delta = 0$) at proper relative phase ($\Delta\varphi = 0$) only transitions starting from $|B\rangle$ are possible:

$$\langle 3|V_{dip}|B\rangle = \frac{\hbar\Omega}{2} \exp[-i(\omega_1 + \omega_p)t - i\varphi_p] \quad (1.40a)$$

$$\langle 3|V_{dip}|D\rangle = 0. \quad (1.40b)$$

As in the limit that $\Omega_p \ll \Omega_c$ we saw that $|a^0\rangle \rightarrow |1\rangle$, in the same limit $|B\rangle \rightarrow |2\rangle$ here. So EIT occurs because, for a strong couple and weak probe, $|1\rangle$ and $|2\rangle$ evolve adiabatically

into two superpositions. One superposition, state $|D\rangle$, decouples from the excited state, and it is the "dark" state. Once in the dark state an atom is "trapped" and cannot be excited to state $|3\rangle$ making the medium transparent to the optical fields. In contrast to $|D\rangle$, $|B\rangle$ is coupled to the excited state and is called the "bright" state, as it is responsible for all absorption and emission in this scheme. Once an atom is excited from the bright state to level $|3\rangle$ it spontaneously decays into either the bright or dark states with equal probability. This results in coherent preparation and eventual trapping of atoms in $|D\rangle$ state which makes the medium appear "darker".

1.3 Motivations and objectives

As stated above, continuous interest to EIT phenomena is stipulated by a number of applications in a variety of fields such as laser cooling, information storage, magnetometry, spectroscopy, atomic frequency references etc. [1]. In many important applications (e.g. quantum frequency standards, compact atomic clocks), the EIT-resonance in cells containing alkali metal vapors is used. Until recently, the cell sizes considered in the majority of works varied in the range of 0 – 10 cm. However, for some applications from practical point of view it is important to reduce the dimensions of cells where the EIT-resonance is formed, at the same time keeping good resonance parameters.

The relevant parameter for the linewidth of EIT-resonance is the dephasing rate of coherence between the ground states that is inversely related to the duration of coherent interaction between an atom and a field: $\Gamma_{21} = (2\pi t)^{-1}$, where $t = L/v$ (L is the distance between cell windows and v is the most probable thermal atomic velocity). In cases, where an atomic vapor is contained in a cell, the relaxation on the walls gives a dominant contribution to dephasing: in fact every collision with a bare cell wall is sufficient to thermalize the ground hyperfine levels, with depolarization probability 0.5 – 1 (see [79] and references therein). So, one expects that the reduction of the vapor cell size will result in increase of the dephasing rate of coherence Γ_{21} leading to broadening of EIT-resonances, as well as to worsening of the EIT-resonance contrast (defined as the ratio of the EIT depth to the height of the shoulders of

the EIT window). The effect has been observed in sub-millimeter thin cells [80,81]. Common ways to reduce this wall relaxation for sub-millimeter cells is the use of buffer gas or paraffin-coated walls [52, 80, 117]. Evidently the effect of collisions should be more pronounced with further reduction of cell thickness as the time of coherent interaction of the atom with the fields shortens causing frequent quenching collisions of atoms with the cell windows. Hence, one could expect that the EIT effect would completely wash out in the case where $L < 1 \mu\text{m}$ ($2\Gamma_{21} > 100 \text{ MHz}$).

Nevertheless, it is demonstrated experimentally that the EIT-resonance can be observed in thin cells of the size about optical transition wavelength (hundreds of nanometres), or extremely-thin cells (ETC) [87, 88]. The explanation for this non-intuitive behavior is as follows: when the coupling laser is resonant with an atomic transition, only the atoms flying nearly parallel to cell windows and hence not experiencing wall collisions do contribute to the formation of the EIT resonance.

The possibility to observe the EIT effect in ETC, is of great interest for its potential application to miniaturization of optical devices such as magnetometers with sub-micrometric spatial resolution and precise frequency references. Miniaturization of cells can also result in creating clusters or even matrixes of cells that can be used for storing and processing quantum information, quantum computers, quantum repeaters for telecommunication networks, etc [89]. nanocells make it possible to study the interaction of atoms with a surface through the frequency shift of the EIT resonance [90].

The peculiarities of the EIT effect in ETC with the thickness of Rb vapor column of the order of light wavelength λ (780 nm), varying in the range of $0.5\lambda - 2.5\lambda$ in Λ -systems on the D_2 -line of ^{85}Rb and ^{87}Rb have been studied experimentally [87] and theoretically [87,88]. The results obtained show that thin and extremely thin cells could be used to form EIT-resonances with good parameters necessary for their further applications. By the time we started the present research work, there were no many publications concerning this subject (only two publications), so we have considered it to be important to study this problem.

In [105] it was shown that for an ordinary cm-size cell, the excitation of D_1 -line results in greater EIT contrast as compared to that for D_2 -line. It was of interest to verify whether this statement holds also in the case of NTC by comparing the measured EIT contrast with

that observed earlier for the D_2 -line [87,88]. Switching from D_2 -line to D_1 -line also expected to be favorable for forming the EIT-resonance in the fluorescence spectrum when the cell thickness is $\lambda/2$. Note that the possibility of EIT-resonance formation for $L = \lambda/2$ and less is theoretically predicted in [88]. However, this has not been observed experimentally for D_2 -line excitation.

The main aims of the present study are: (i) to check whether the EIT resonance in a Λ -system on D_1 -line for NTC with $L = \lambda$ is advantageous as compared with the case of D_2 excitation and to study the dependence of EIT contrast and linewidth on coupling laser detuning; (ii) to study the influence of laser intensity, temperature and density of atomic vapor, collisions of atoms with the cell walls; (iii) to investigate the EIT behavior under the further reduction of cell thickness to $L = \lambda/2$, also in fluorescence spectrum. Furthermore, the study addresses the influence of a buffer gas on EIT-resonance formation.

For the realization of these aims the following objectives have been tasked :

- 1) development of sealed-off thin and extremely thin cells containing Rb vapor with the possibility of smooth change of the atomic vapor column in the range of 20 nm – 2 mm;
- 2) the study of different Λ -systems around D_1 and D_2 -lines of Rb for the formation of narrow EIT-resonances depending on the cell thickness in the range of 20 nm – 2 mm.

1.4 Theory of EIT in nanocells

1.4.1 Interacting systems: atomic vapor and electromagnetic fields

We choose an atomic rubidium vapor and two laser fields as an interacting system. A brief overview of the line structure of the ^{85}Rb D_1 -line used for the EIT experiments in this thesis is given in this section. We model here the rubidium atom as a four-state Λ -type atom within its D_1 -line ($5^2S_{1/2} \rightarrow 5^2P_{1/2}$) and correspond these atomic states to energy eigenstates of the bare atom Hamiltonian H_0 , i.e. to the four states $|1\rangle$, $|2\rangle$, $|3\rangle$ and $|4\rangle$.

1.4.2 Modeling of the rubidium atom within the D_1 -line

Rubidium is chosen as our atom species most importantly as for the purposes of EIT, it has a suitable atomic energy structure that can be used as an effective Λ -scheme. We choose the isotope ^{85}Rb , which has previously been used to demonstrate EIT by many authors.

^{85}Rb is an alkali metal atom having only a single electron in its outer shell. Several fundamental interactions contribute to the level structure of the alkali atoms. The fine structure results from the coupling between the orbital angular momentum \mathbf{L} of the valence electron together with its spin angular momentum \mathbf{S} . The total electron angular momentum is

$$\mathbf{J} = \mathbf{L} + \mathbf{S}, \quad (1.41)$$

where \mathbf{J} is a quantum number that may have the values:

$$|L - S| \leq J \leq L + S. \quad (1.42)$$

In the ground state of ^{85}Rb , $L = 0$ and $S = 1/2$, hence $J = 1/2$. In the excited state $L = 1$, therefore $J = 1/2$ or $J = 3/2$. The transition to $J = 3/2$ is known as the D_2 -line ($5^2S_{1/2} \rightarrow 5^2P_{3/2}$), and the transition to $J = 1/2$ is known as the D_1 -line ($5^2S_{1/2} \rightarrow 5^2P_{1/2}$) which is presented in Fig. 1.6.

The hyperfine structure results from the coupling between the total electron angular momentum \mathbf{J} together with the total nuclear angular momentum \mathbf{I} and is given by:

$$\mathbf{F} = \mathbf{J} + \mathbf{I}. \quad (1.43)$$

The magnitude \mathbf{F} (total atom spin) can take values:

$$|J - I| \leq F \leq J + I. \quad (1.44)$$

In the ground state of ^{85}Rb $J = 1/2$ and $I = 5/2$, hence $F = 2$ or 3 (see Fig. 1.6).

Each of the hyperfine energy levels (F) splits into M_F ($= 2F + 1$) hyperfine Zeeman sublevels in the presence of the external Earth magnetic field. We simplify the many-states

problem into four hyperfine states by neglecting the less important hyperfine Zeeman sub-levels due to the weak Earth magnetic field strength, thus resulting in a modeled four-state Λ -type atomic system.

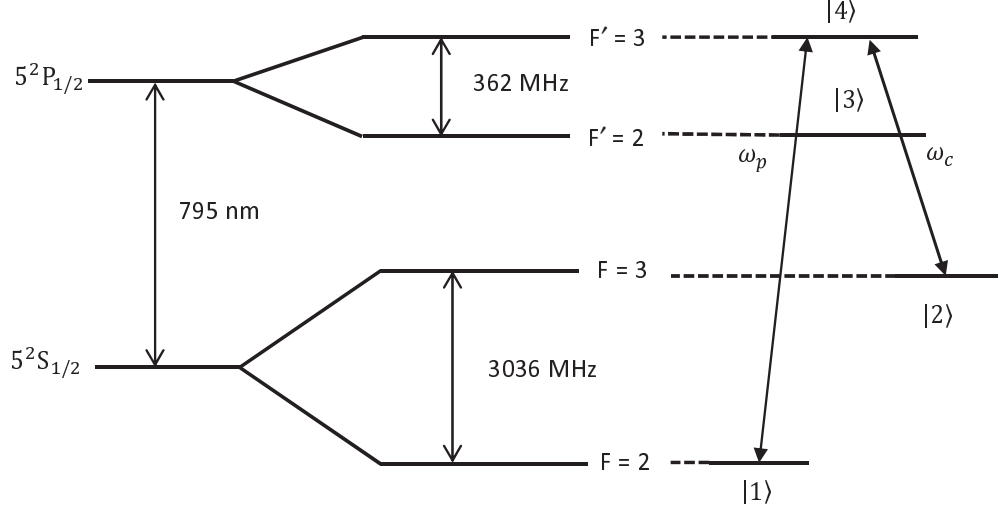


Figure 1.6: ^{85}Rb D_1 -line. The dotted lines show the states used as for a Λ -atom. The data are taken from [77].

1.4.3 Assumptions and hypotheses

- We assume that the atomic density N is low enough so that the effect of collisions between the atoms can be ignored and only atom-surface collisions are to be considered;
- An important point for our theoretical consideration consists in supposition that the atoms lose optical excitation and all memory about the previous state when colliding with the cell windows;
- The incident laser beam diameter largely exceeds the cell thickness;
- The velocity distribution is considered to be Maxwellian and is given by $W(v) = \frac{N}{u\sqrt{\pi}} \exp[-(\frac{v}{u})^2]$, where v is the atomic velocity, N is the atomic density, and u is the most probable velocity given by $u = \sqrt{2k_B T/M}$ with k_B being the Boltzmann constant, T the temperature of the vapor in Kelvin and M the atomic mass.

1.4.4 Basic equations

To interpret the experimental results, we consider four-level Λ -type atomic systems (shown in Fig. 1.7) confined in a cell of thickness L . Level $5^2S_{1/2}$ ($F_g = 2$) is coupled with level $5^2P_{1/2}$ ($F_e = 2, 3$) by a probe field E_p (with angular frequency ω_p) forming transitions $|1\rangle \rightarrow |3\rangle, |4\rangle$, and level $5^2S_{1/2}$ ($F_g = 3$) is coupled with $5^2P_{1/2}$ ($F_e = 2, 3$) by a coupling field E_c (with angular frequency ω_c) for the transitions $|2\rangle \rightarrow |3\rangle, |4\rangle$: these transitions will be referred to as the $F = 2 \rightarrow F' = 2, 3$ and $F = 3 \rightarrow F' = 2, 3$ transitions, respectively. For simplicity, we restrict ourselves to one dimensional situation where the two driving linearly polarized laser radiations are in the z -direction. The probe and coupling lasers are detuned from the corresponding atomic resonances by

$$\begin{aligned}\Delta_{p1(p2)} &= \omega_p - \omega_{31(41)}, \\ \Delta_{c1(c2)} &= \omega_c - \omega_{32(42)},\end{aligned}\tag{1.45}$$

where the subscripts p (c) mark the detunings for the probe (coupling) lasers, ω_{ij} is the frequency difference between levels i and j . The total Hamiltonian of the system is given by $\hat{H} = \hat{H}_0 + \hat{H}_I$, where \hat{H}_0 describes a free atom and \hat{H}_I describes the interaction between the atom and the electric fields. With electric-dipole and rotating-wave approximations, the interaction Hamiltonian \hat{H}_I of the system is given by

$$\hat{H}_I = -\hbar(\Omega_{p1}|3\rangle\langle 1| + \Omega_{p2}|4\rangle\langle 1| + \Omega_{c1}|3\rangle\langle 2| + \Omega_{c2}|4\rangle\langle 2|) + \text{H.c.},\tag{1.46}$$

where $\Omega_{p1,p2} = \mu_{1,3,4}E_p/2\hbar$ and $\Omega_{c1,c2} = \mu_{2,3,4}E_c/2\hbar$ are the Rabi frequencies of the probe and coupling fields, respectively, with μ_{ij} being the electric-dipole matrix element associated with the transition from j to i , and H.c. represents Hermitian conjugate.

The internal atomic dynamics is described by a semiclassical density matrix $\rho = \sum \rho_{ij}|i\rangle\langle j|$, the time evolution of which is given by the Liouville equation of motion:

$$\dot{\rho} = -i/\hbar[\hat{H}, \rho] + \Gamma\rho,\tag{1.47}$$

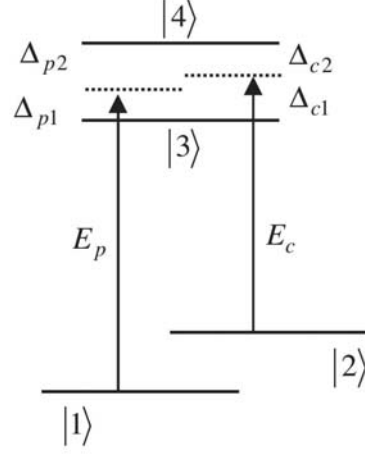


Figure 1.7: Λ -type four-level atomic system.

where Γ is the relaxation operator : $\Gamma_{ij} = \frac{1}{2}(\gamma_i + \gamma_j) + \gamma_{ij}\delta_{ij}$. Here γ_i , γ_j are the natural decay rates of states $|i\rangle$ and $|j\rangle$, and γ_{ij} is the pure dephasing rate.

The density-matrix equations of motion for the system in the rotating frame read

$$\begin{aligned}
\dot{\rho}_{11} &= -2 \operatorname{Im}(\Omega_2^* \rho_{31}) - 2 \operatorname{Im}(\Omega_1^* \rho_{41}) + \gamma_{31} \rho_{33} + \gamma_{41} \rho_{44}, \\
\dot{\rho}_{22} &= -2 \operatorname{Im}(\Omega_4^* \rho_{32}) - 2 \operatorname{Im}(\Omega_3^* \rho_{42}) + \gamma_{32} \rho_{33} + \gamma_{42} \rho_{44}, \\
\dot{\rho}_{33} &= 2 \operatorname{Im}(\Omega_2^* \rho_{31}) + 2 \operatorname{Im}(\Omega_4^* \rho_{32}) - \Gamma_{33} \rho_{33}, \\
\dot{\rho}_{44} &= 2 \operatorname{Im}(\Omega_1^* \rho_{41}) + 2 \operatorname{Im}(\Omega_3^* \rho_{42}) - \Gamma_{44} \rho_{44}, \\
\dot{\rho}_{43} &= i\Omega_1 \rho_{31}^* - i\Omega_2^* \rho_{41} + i\Omega_3 \rho_{32}^* - i\Omega_4^* \rho_{42} - (i\Delta_{hsp} + \Gamma_{43}) \rho_{43}, \\
\dot{\rho}_{42} &= i\Omega_3 (\rho_{22} - \rho_{44}) + i\Omega_1 \rho_{21}^* - i\Omega_4 \rho_{43} + (i\Delta_{c2} - \Gamma_{42}) \rho_{42}, \\
\dot{\rho}_{41} &= i\Omega_1 (\rho_{11} - \rho_{44}) + i\Omega_3 \rho_{21} - i\Omega_2 \rho_{43} + (i\Delta_{p2} - \Gamma_{41}) \rho_{41}, \\
\dot{\rho}_{32} &= i\Omega_4 (\rho_{22} - \rho_{33}) + i\Omega_2 \rho_{21}^* - i\Omega_3 \rho_{43}^* + (i\Delta_{c1} - \Gamma_{32}) \rho_{32}, \\
\dot{\rho}_{31} &= i\Omega_2 (\rho_{11} - \rho_{33}) + i\Omega_4 \rho_{21} - i\Omega_1 \rho_{43}^* + (i\Delta_{p1} - \Gamma_{31}) \rho_{31}, \\
\dot{\rho}_{21} &= i\Omega_4^* \rho_{31} - i\Omega_2 \rho_{32}^* + i\Omega_3^* \rho_{41} - i\Omega_1 \rho_{42}^* - (i\delta + \Gamma_{21}) \rho_{21}.
\end{aligned} \tag{1.48}$$

Here Δ_{hsp} is the hyperfine splitting of the upper levels, and δ is the two-photon Raman detuning. For the Rabi frequency the estimates are obtained from $\Omega/2\pi = a\gamma(I/8)^{1/2}$, where I is the laser intensity in mW/cm^2 , γ is the decay rate of the excited state, and a is a fit parameter (for our case $a \approx 0.2$) [97].

Consistent with the above assumptions (see Sec. 1.4.3), we ignore the collisional broad-

ening of optical transitions compared to the spontaneous decay rate and to the relaxation of atoms traveling out of the diameter of the laser beam. The dephasing rate of the ground-state coherence, Γ_{21} , is determined in the model by the finite time of flight of atoms between the cell windows. Under the assumptions made, this parameter, usually introduced into theoretical calculations as a phenomenological constant to fit the experimental data, is taken into account in the model exactly by solving the temporal density-matrix equations with proper boundary conditions for each atom separately.

A number of relevant parameters, both inherent to the atomic system and the experimental setup, are included into the model such as hyperfine pumping, phase fluctuations in the laser fields [92,94], non-correlation of the laser fields [78]. To describe the effects of the finite bandwidth of the laser field to the coherence of the interaction, we use the Wiener-Levy phase diffusion model (see, e.g., [93,94]). We assume that both lasers have a Lorentzian spectrum with a full frequency width at half maximum γ_L (as obtained from the model adopted). The laser bandwidths are incorporated into the calculations by introducing relaxation terms for the nondiagonal density-matrix elements using the procedure developed in [92,95].

1.4.5 Absorption spectra

We are concerned with the probe field transmitted through the second window

$$E_{out} = t_2 E_{p0}. \quad (1.49)$$

Here $t_2 = 2/(n_2 + 1)$ is the transmission coefficient of the second window, and E_{p0} is the probe field inside the cell

$$E_{p0}(z, t) = \frac{1}{2} \mathcal{E}_{p0}(z) \exp[-i(\omega_p t - k_p z)] + c.c. \quad (1.50)$$

The goal is to find an expression for the field $E_{p0}(z)$ at any position z inside the vapor in order to obtain the transmitted signal $I_p \propto |E_{out}|^2$.

The field transmitted inside the cell obeys the Maxwell equation for the wave propagation

through the resonant medium

$$\nabla^2 E_{p0} - \frac{1}{c^2} \frac{\partial^2 E_{p0}}{\partial t^2} = \mu_0 \frac{\partial^2 P_0}{\partial t^2}, \quad (1.51)$$

with μ_0 being the magnetic permeability, c the velocity of the light in the vacuum, and where we define the amplitude of the polarization induced inside the vapor at the probe frequency $\mathcal{P}_0(z)$ as

$$P_0(z, t) = \frac{1}{2} \mathcal{P}_0(z) \exp[-i(\omega_p t - k_p z)] + c.c. \quad (1.52)$$

The field inside the cell can be represented as

$$E_{p0}(z) = E'_{p0}(z) + E''_{p0}(z). \quad (1.53)$$

Here $E'_{p0}(z)$ is the probe field inside the empty cell, and $E''_{p0}(z)$ is the resonant contribution of the medium to the field that consists of two parts : the total backward E_b and forward E_f propagating responses generated in the medium. These fields can be calculated from Maxwell equation (1.51) by the Green function method and read [96, 98]

$$\begin{aligned} E_f(z = L) &= 2\pi i k_p \int_0^L \mathcal{P}_0(z) dz, \\ E_b(z = 0) &= 2\pi i k_p \int_0^L \mathcal{P}_0(z) e^{2ik_p z} dz. \end{aligned} \quad (1.54)$$

Note that in a very dilute medium, i.e. $E''_{p0}(z) \ll E'_{p0}(z)$, the field $E_{p0}(z)$ that drives the probe polarization $P_0(z)$ in the medium is essentially the field $E'_{p0}(z)$ of an empty cell. Under this assumption, considering the effects of interference and multiple reflections from the cell windows together with the boundary conditions at $z = 0$ and $z = L$, one obtains for the probe field inside the empty cell [96]

$$E'_{p0}(z) = \mathcal{E}_p t_1 \frac{1 - r_2 \exp[2ik_p(L - z)]}{F}, \quad (1.55)$$

and for the resonant contribution at the cell exit $z = L$

$$E''_{p0}(z = L) = \frac{1}{F} (E_f(z = L) - r_1 E_b(z = 0)), \quad (1.56)$$

where \mathcal{E}_p is the amplitude of the probe incident field, and the factor $F = 1 - r_1 r_2 \exp(2ik_p L)$ takes into account the influence of the beam reflected by the second wall of the cell (which is important in the case where the cell thickness is $L \sim \lambda$), i.e. the Fabry-Perot effect. Here $r_1 = \frac{n_1 - 1}{n_2 + 1}$ and $r_2 = \frac{n_2 - 1}{n_2 + 1}$ are the reflection coefficients of the first and second windows, respectively, and $t_1 = \frac{2n_1}{n_1 + 1}$ is the transmission coefficient of the first window.

Using the expressions given in (1.54) one obtains for E''_{p0} :

$$E''_{p0}(z = L) = \frac{2\pi i k_p}{F} \int_0^{z'=L} \mathcal{P}_0(z') \left[1 - r_1 e^{2ik_p z'} \right] dz'. \quad (1.57)$$

Taking into account the dilute character of the medium ($E''_{p0} \ll E'_{p0}$), we obtain for the transmitted signal:

$$I_p \approx t_2^2 \left[|E'_{p0}(L)|^2 + 2 \operatorname{Re} \left\{ E''_{p0}(z = L) E'^*_{p0}(z = L) \right\} \right]. \quad (1.58)$$

The absorption signal of the probe field is given by the second term in the brackets

$$S_{abs} \sim 2 \operatorname{Re} \left\{ E''_{p0}(z = L) E'^*_{p0}(z = L) \right\}. \quad (1.59)$$

To obtain the probe absorption spectra, we need to calculate the polarization of the medium on the frequency of the probe field that is determined by

$$P_0(z) = Nd_{31} (\rho_{31}^+ + \rho_{31}^-) + Nd_{34} (\rho_{41}^+ + \rho_{41}^-), \quad (1.60)$$

where nondiagonal matrix elements $\rho_{j1}^+ \equiv \rho_{j1}(z = v_z t)$ and $\rho_{j1}^- \equiv \rho_{j1}(z = L - v_z t)$ with $j = 3, 4$ relate to the atoms flying with the velocity in the positive and negative directions of the cell axis, respectively. We provide this by exact numerical solution of the set of optical Bloch equations as given by Eqs. (1.48). To include the Doppler-broadening effect, we average the density-matrix elements obtained for a single atom over the Maxwellian velocity distribution of the atoms. Inserting formulas (1.55), (1.57), (1.60) to Eq. (1.59) one gets for

the Doppler broadened absorption profile

$$\begin{aligned} \frac{1}{\mathcal{E}_p^2} \langle S_{abs} \rangle = & - \frac{4\pi\omega_p N t_2^2 t_1}{cu\sqrt{u}} \frac{1}{\mathcal{E}_p |F|^2} \int_0^\infty e^{-v_z^2/u^2} v_z dv_z \int_0^{L/v} dt \\ & \times \text{Im} \left\{ \sum_{i=3,4} d_{i1} \left[\rho_{i1}^+(t, \Delta_p^+, E_{p0}(v_z t)) (1 - r_1 e^{2ik_p v_z t}) \right. \right. \\ & \left. \left. \rho_{i1}^+(t, \Delta_p^-, E_{p0}(L - v_z t)) (1 - r_1 e^{2ik_p(L - v_z t)}) \right] \right\}. \end{aligned} \quad (1.61)$$

Here $\Delta_p^\pm = \Delta_p \pm k_p v_z$ are the Doppler shifted detunings of the probe field. The plus sign refers to the atoms with the velocity \mathbf{v} in the positive direction of the cell axis, and the minus sign refers to the atoms with the velocity \mathbf{v} in the negative direction of the cell axis. A general agreement between the results of our theoretical calculations and those of the experiment is seen.

1.5 The experimental setup for the study of EIT

The experimental arrangement is sketched in Fig. 1.8. The beams of two separate single-frequency extended cavity diode lasers (ECDL) with $\lambda \approx 794$ nm and ~ 1 MHz linewidth are well superimposed and directed onto the Nanometric-thin cell (NTC) at near-normal incidence by the first Glan prism (G_1). The coupling and probe beams of 3×2 mm elliptical shape have linear and mutually perpendicular polarizations. Faraday isolators (1) are used to prevent an extraneous feedback from reflected beams. NTC (4) is placed inside the three pairs of mutually perpendicular Helmholtz coils (2) providing the possibility to cancel laboratory magnetic field as well as to apply homogeneous magnetic field. The transmission and fluorescence radiations are recorded by the photodiodes (3) followed by operation amplifiers; the signal of the photodiodes is recorded by a two-channel digital storage oscilloscope Tektronix TDS 3032B.

The radiation power of the coupling and probe lasers was varied throughout the measurement in the range of 1 - 30 mW and 0.01 - 3 mW, respectively using neutral density filters F . An improved Dichroic-Atomic-Vapor-Laser-Locking technique realized with the help of a separate NTC with $L = \lambda/2$, a permanent ring magnet (7), $\lambda/4$ plate, Glan prism (G_3), and an error signal unit for electronic subtraction of two photodiodes signals is used for the cou-

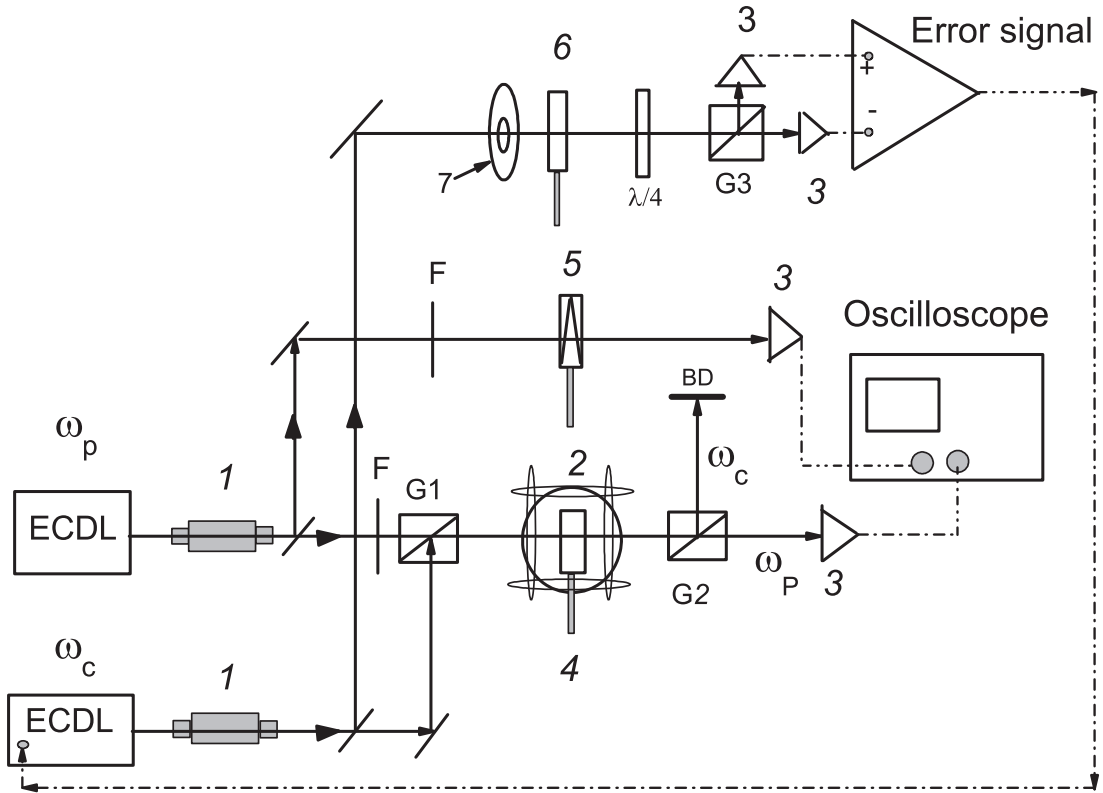


Figure 1.8: Sketch of the experimental setup. 1- Faraday isolators (FI); $G_{1,2,3}$ - Glan prisms; 2- Helmholtz coils; 3- photodiodes; 4- main NTC; 5- auxiliary NTC of $L = \lambda$; 6- auxiliary NTC of $L = \lambda/2$; 7- permanent ring magnet (for details, see the text); BD- beam damp.

pling laser frequency stabilization (see [99]). The frequency reference spectrum was formed with the help of an auxiliary NTC (5) with $L = \lambda$ [99]. A second Glan prism (G_2) was used for separating the coupling and probe beams, so that only the probe beam transmission could be monitored.

All the main parameters of the experimental technique are given here after.

a) Semiconductor CW diode lasers

Active development of techniques leads to fabrication of diode lasers radiating in the range 400 – 1000 nm with high spectral and specific technical characteristics. These lasers have narrowband radiation with line $\gamma_L = 0.5 - 10$ MHz and intensity of radiation in the range 10 – 100 mW. The more attractive characteristics of diode lasers are: the narrowband radiation, compactness and low power consumption and comparatively easy way to vary the wavelength of radiation. The high efficiency of diode lasers is conditioned by the way of

the radiation generation which is realized by direct pumping of active media by electric current. The temperature and the pumping current determine wavelength of the radiation and due to that, it is thus important to have stable and noiseless power supply as well as good thermocontroller for stabilization of temperature of diode's case. For linewidth narrowing a external-cavity is used. Tunable ECDL usually use a diffraction grating as the wavelength selective element in the external resonator. They are also called grating-stabilized diode lasers. In our experiments we use the ECDLs with common Littrow configuration.

The common Littrow configuration contains a collimating lens and a diffraction grating as the end mirror. The first-order diffraction beam provides optical feedback to the laser diode chip, which has an anti-reflection coating on the side near end mirror.

Block-scheme of control module and construction of external cavity is represented on fig. 1.19. Stabilized noiseless current generator and thermo-stabilisation supply with feedback

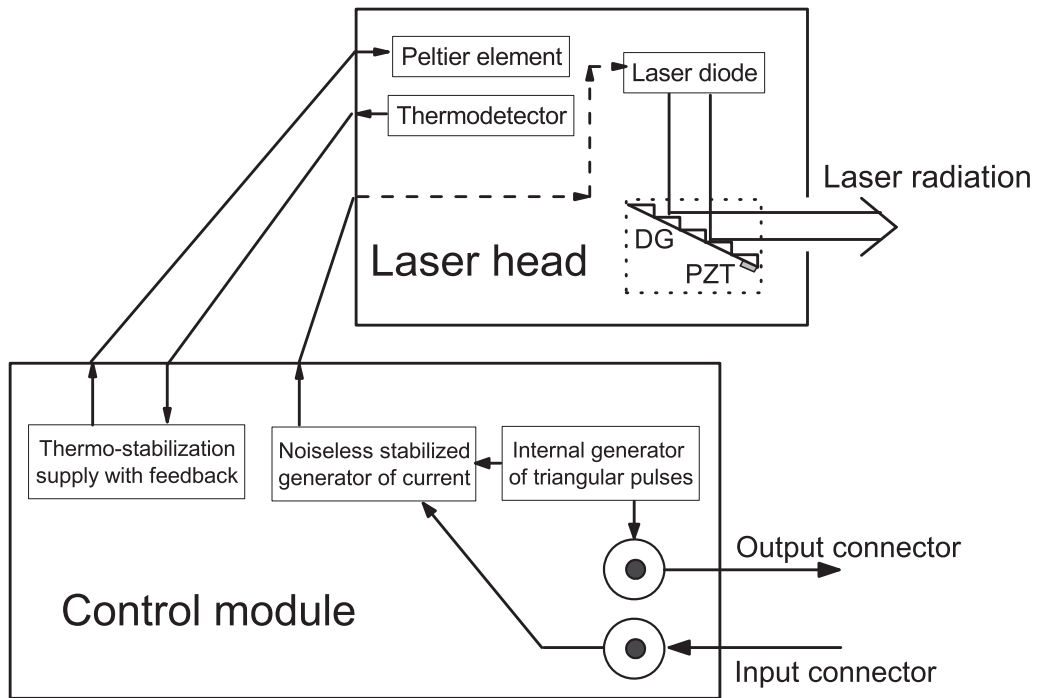


Figure 1.9: Block-scheme of control module and construction of external cavity.

are the main parts of the control module.

The emission wavelength can be tuned by rotating the diffraction grating. For this purpose diffraction grating (DG) is installed on a piezoelectrical (PZT) mount, which may rotate by

DL parameters	DL without external cavity	ECDL
Emission wavelength	780 nm, 795 nm, 894 nm, 852 nm	780 nm, 795 nm, 894 nm, 852 nm
Spectral linewidth	5 – 30 MHz	0.7 – 1 MHz
Emission power	10 – 80 mW	10 – 40 mW
Divergence	~ 1 mrad	~ 1 mrad
Power supply parameters		
Injection maximal current	200 mA	200 mA
Current setting precision	0.1 mA	0.1 mA
Stabilization of current	±0.03 mA	±0.01 mA
Internal modulation	10 – 3000 Hz	10 – 3000 Hz
Current of modulation	0 – 5 mA	0 – 4 mA
External modulation	0 – 100 mA	0 – 100 mA
Temperature range	+5 .. + 55 °C	+15 .. + 30 °C
Precision of temperature measurement	0.1 °C	0.1 °C
Temperature setting precision	0.1 °C	0.1 °C
Temperature stabilization	0.03 °C	0.01 °C

Table 1.1: Technical characteristics of DLs

changing the voltage applied on PZT chip.

Peltier element realizes the thermo-stabilization of the diode chip. In order to measure the diode chip temperature the chip is installed on a mount with a thermo-detector, which realizes a feedback with the control module.

The control module is equipped with input connector for the external modulation of the laser diode current. That allows to change the laser radiation wavelength (in case of low frequency modulation ~ 0.1 – 10 Hz) as well as frequency modulation (FM) (high frequency modulation ~ 0.5 – 100 kHz).

For synchronization with external devices, control module is also equipped with an output connector which passes train of triangular pulses from internal generator to external devices.

Main characteristics of diode lasers are represented in table 1.1. In our experiments we use ECDL producing a wavelength $\lambda = 780$ nm (D_2 -line of Rb) and 794.7 nm (D_1 -line of Rb) with tuning range 10 – 40 GHz. For beam collimation a 2 – 4 mm focal length lens is used. It results a divergence of 1 mrad of the outgoing beam.

b) Faraday isolator

In fact ECDL have big gain coefficient and it leads to high sensitivity of ECDL to feedback. It means that ECDL are very sensitive to reflections of the laser beam from optical elements

of experimental setup. Strongest reflections appear when it is necessary to direct the laser beam perpendicularly to optical surfaces, for instance perpendicularly to the windows of a nanocell filled with atomic vapors. In this case the nanocell reflects $\sim 7\%$ of the incident beam intensity and back-reflected beam (feedback) causes non-stable regime of the laser process. In order to avoid the feedback of the laser radiation, FI are used. The principle of working of the FI is as follows: the laser beam is directed on a FI at first pass through a first Glan polarizer enlightened by a plane polarized laser radiation. After a first polarizer, the linearly polarized laser radiation passes through a magneto-active element and under the influence of the external magnetic field applied to the magneto-active element undergoes a rotation of the polarization plane of the laser radiation. The magnitude of the magnetic field applied to the magneto-active element is specially adjusted to rotate the plane of polarization of 45° . After the magneto-active element, the radiation passes through a second Glan polarizer which is rotated of 45° in respect with the first polarizer and transmits the laser radiation without losses. In this case the back reflected beam, after passing through a second polarizer and magneto-active element, will be rotated one more time of 45° and will not be passed through the first Glan polarizer due to perpendicular polarization of reflected beam in respect with the initial polarization. FI used in our experiments have return losses equal to 40 dB. It means that the reflected beam is 10^4 times attenuated. It is enough for stable work of ECDL.

c) Helmholtz coils and permanent ring neodymium magnets

In order to apply the magnetic field to the cell filled with alkali metal vapor, we used Helmholtz coils and permanent ring magnets .

A pair of Helmholtz coils consists of two identical circular magnetic coils that are placed symmetrically one on each side of the experimental area along a common axis, and separated by a distance h equal to the radius R of the coil (see Fig. 1.10). Each coil carries an equal electrical current flowing in the same direction (see Fig. 1.11).

In Fig.1.12 cross section view of ideal Helmholtz coil is demonstrated.

Setting $h = R$, which is what defines a Helmholtz pair, minimizes the nonuniformity of the field at the center of the coils, in the sense of setting $\partial^2 B / \partial x^2 = 0$ (meaning that the first nonzero derivative is $\partial^4 B / \partial x^4$ as explained below), but leaves about 7% variation in

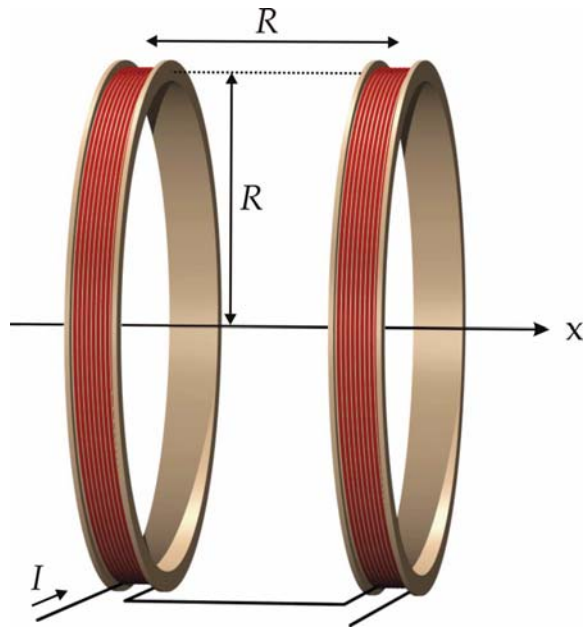


Figure 1.10: Helmholtz coil schematic drawing.

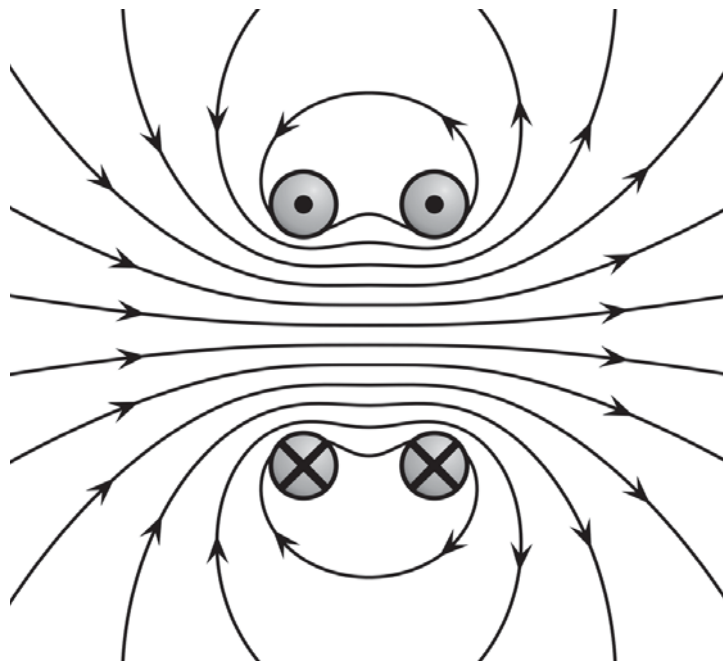


Figure 1.11: Magnetic field lines in a plane bisecting the current loops. Note the field is approximately uniform in between the coil pair. (In this picture the coils are placed one beside the other: the axis is horizontal)

field strength between the center and the planes of the coils. A slightly larger value of h reduces the difference in field between the center and the planes of the coils, at the expense of worsening the fields uniformity in the region near the center, as measured by $\partial^2 B / \partial x^2$.

These simple formulas use the formula for field due to a current loop to obtain the

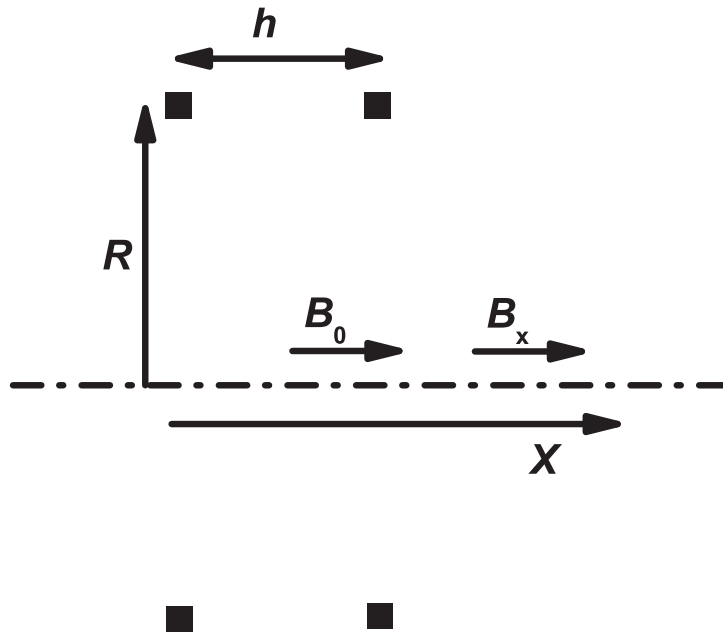


Figure 1.12: Ideal Helmholtz coil in cross section view

magnetic field at any point along the axis of an ideal Helmholtz coil (see eq.1.62).

$$B_x = \frac{\mu_0 i}{2R} \left[\frac{1}{(\gamma^2 + \gamma + 5/4)^{3/2}} + \frac{1}{(\gamma^2 - \gamma + 5/4)^{3/2}} \right] \quad (1.62)$$

Where B_x is the magnetic field, in teslas, at any point on the axis of the Helmholtz coil. The direction of the field is perpendicular to the plane of the loops.

μ_0 is the permeability constant (1.26×10^{-6} H/m)

i is the current in the wire, in amperes.

R is the radius of the current loops, in meters.

γ is the ratio, x/R , where x is the distance, on axis, from the center of the Helmholtz coil, and R is the radius of the coil.

Figure 1.13 demonstrates the superior central field uniformity of an ideal Helmholtz coil

The Helmholtz coils are very useful for applying low magnetic fields, and three pair of coils orientated one orthogonal another can be used for compensating the Earth magnetic field. But for applying magnetic field $B > 200$ G it is much easier to use neodymium permanent ring magnets.

A neodymium magnet (also known as NdFeB, NIB, or Neo magnet), the most widely-used type of rare-earth magnet, is a permanent magnet made from an alloy of neodymium,

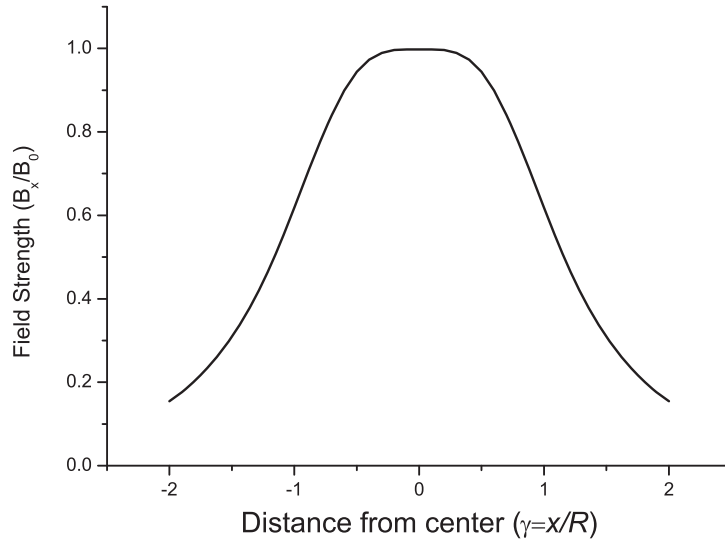


Figure 1.13: Dependence of the magnetic field on distance from center for ideal Helmholtz coil)

iron, and boron to form the $ND_2Fe_{14}B$ tetragonal crystalline structure. Developed in 1982 by General Motors and Sumitomo Special Metals, neodymium magnets are the strongest type of permanent magnet made. They have replaced other types of magnet in many applications in modern products that require strong permanent magnets, such as motors in cordless tools, hard disk drives, and magnetic fasteners.

The tetragonal $ND_2Fe_{14}B$ crystal structure has exceptionally high uniaxial magnetocrystalline anisotropy. This gives the compound the potential to have high coercivity (i.e., resistance to being demagnetized). The compound also has a high saturation magnetization (J_s 1.6 T or 16 kG) and typically 1.3 tesla. Therefore, as the maximum energy density is proportional to J_s^2 , this magnetic phase has the potential for storing large amounts of magnetic energy (BH_{max} 512 kJ/m³ or 64 MGOe), considerably more than samarium cobalt (SmCo) magnets, which were the first type of rare earth magnet to be commercialized. In practice, the magnetic properties of neodymium magnets depend on the alloy composition, microstructure, and manufacturing technique employed. Some important properties used to compare permanent magnets are: remanence (M_r), which measures the strength of the magnetic field; coercivity (H_{ci}), the material's resistance to becoming demagnetized; energy product (BH_{max}), the density of magnetic energy; and Curie temperature (T_C), the temperature at which the material loses its magnetism. Neodymium magnets have higher remanence,

much higher coercivity and energy product, but often lower Curie temperature than other types. Neodymium is alloyed with terbium and dysprosium in order to preserve its magnetic properties at high temperatures. The Fig 1.9 compares the magnetic performance of neodymium magnets with other types of permanent magnets.

Magnet	Mr (T)	Hci (kA/m)	BH _{max} (kJ/m ³)	TC (°C)
Nd ₂ Fe ₁₄ B (sintered)	1.0–1.4	750–2000	200–440	310–400
Nd ₂ Fe ₁₄ B (bonded)	0.6–0.7	600–1200	60–100	310–400
SmCo ₅ (sintered)	0.8–1.1	600–2000	120–200	720
Sm(Co, Fe, Cu, Zr) ₇ (sintered)	0.9–1.15	450–1300	150–240	800
Alnico (sintered)	0.6–1.4	275	10–88	700–860
Sr-ferrite (sintered)	0.2–0.4	100–300	10–40	450

Figure 1.14: The magnetic performance comparison of neodymium magnets with other types of permanent magnets

d) Registration of laser radiation in the range 700 – 1000 nm

In order to register signal of laser radiation absorption, fluorescence spectra, selective reflection, signal of probe radiation in saturated absorption spectroscopy and others, photo-detectors based on FD-24K photodiodes are used. These photodiodes have an aperture about 1 cm² (presence of a big aperture is important for the significant registration of weak fluorescence signals) and good sensitivity in the range 500 – 1100 nm. To amplify the photodiode signal, an amplifier based on operational amplifier KR140UD8 is used. Experimental data are saved in a digital storage oscilloscope.

Our registration technique based on photo-detectors and digital oscilloscope was enough sensitive to register optical signals with power close to ~ 5 nW

e) Measurement of temperature

The temperature T_{SA} of cell's side-arm, which contains metal, determines the density of the atomic vapor of the alkali metals used in our experiments. To avoid condensation of atoms on optical windows of the cell, it is necessary to keep the temperature T_W of the windows 15 – 20 °C higher than the temperature of the side-arm. It implies a permanent control of the temperature of the cell's windows and of the side-arm, thus we used a chromel-alumel thermocouple to measure and adjust the temperature. This thermocouple allows the measurement of the temperature up to 1000 °C, moreover it has very weak magnetic properties, which is important in the case of detection of magneto-optical effects especially with strong magnetic field of thousands gauss. An ordinary milli-voltmeter is used for measuring the voltage of the thermocouple: 0.01 mV corresponds to $T = 0.2$ °C.

1.5.1 Construction of thin cells containing atomic vapors (of width from a few to hundreds of μm)

The description of thin cells (the thickness of tens of μm) is shown on fig. 1.15. Rectangular, well polished plates are chosen as cell windows (1). The sizes of the plates are 20×30 mm of thickness 3 mm. The plates are made from a technical crystalline sapphire (Al_2O_3), which is chemically stable to aggressive hot Rb vapors, or from the crystal of a garnet ($\text{Y}_3\text{Al}_5\text{O}_{12}$), which is also chemically stable to Rb vapors [100, 101]. Since a crystalline sapphire has a natural birefringence, the windows of the cells are prepared in such a way that the c-axis is perpendicular to the surface of the window. In this case, if the laser radiation is oriented perpendicularly to the window, the birefringence significantly decreases.

In the study of the magneto-optical processes a great advantage of using garnet is that the birefringence is absent. The plates of a sapphire are transparent in the range $0.2 - 6 \mu\text{m}$, and for a garnet in the range $0.3 - 5 \mu\text{m}$. A sapphire or garnet plate (1) is made with a small wedge ~ 10 angular minutes in order to avoid overlapping of the reflected radiation from the surfaces of the plate. Since in the experiments it is important to have different thickness L of atomic metal vapors, the gap between the windows of cells, as a rule, is made with variable thickness (that is wedge-shape). For this purpose at the top and the bottom part of the cell, between the windows, thin strips of titanium are placed (noted (2) on fig. 1.15). Note, that

Ti is chemically stable to hot vapors of Rb and Cs. Further, for example, if a

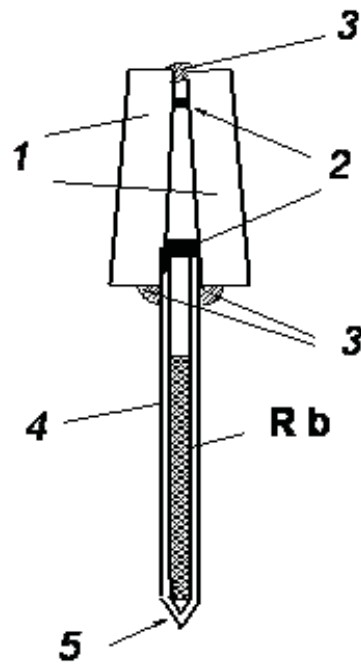


Figure 1.15: Description of thin cell (nanocell): 1 - sapphire or garnet plates, 2 - titanium or platinum strips, 3 - glue, 4 - sapphire tube, 5 - glass side-arm.



(a) The thin cell with Rb.



(b) The nanocell with Rb.

Figure 1.16: The photograph of thin cell and nanocell: (a) thin cell, thickness L varying in range from 50 to 90 μm ; (b) nanocell with thickness L varying in range from 50 nm to 2 μm .

thin rectangular Ti strip of 0.5 mm width, 3 mm length and 50 μm thickness is placed at

the top and a thin strip of $90\ \mu\text{m}$ at the bottom, then after packing of the cell, the thickness L of a vapor column in the vertical plane (top-down) will vary from 50 to $90\ \mu\text{m}$. If the direction of the laser beam is fixed and the cell is placed in the vertical plane, then the laser beam will interact with atomic vapors of column thickness in the range $50 - 90\ \mu\text{m}$.

It is important to note that within a beam of diameter $D_L = 0.5\ \text{mm}$, the thickness of the vapor column changes very slightly (5%). Further at the bottom of the windows a $2\ \text{mm}$ diameter hole is drilled, where a thin crystal sapphire tube with an external diameter $2\ \text{mm}$ and length $50\ \text{mm}$ is placed (4). Then the whole construction is glued into a package (the glue spots are shown on fig. 1.15 (3)) in a vacuum chamber [45]. After the glueing a small glass side-arm is soldered to the sapphire tube (5). The further filling of Rb is done with a glass vacuum post as it is made for glass cells. The quantity of metallic Rb is chosen so that the sapphire tube with an inner diameter of $1\ \text{mm}$ is almost completely filled (see fig. 1.16(a)). As it was demonstrated in [101], the density of Rb vapor is determined by the temperature T of the upper limit of the metallic Rb column in the sapphire tube (consequently a thermocouple is soldered to side-arm, so its tip has a good thermal contact with the upper limit of the column, see. fig. 1.16(b)).

In case of the corresponding construction of the heater, it is possible to obtain the following marginal temperature regime: T on the upper limit of the metallic Rb column $\sim 500\ \text{°C}$ and the temperature T of the glass side-arm (which is outside of the heater) $\sim 80\ \text{°C}$ at which a chemical reaction of Rb with a glass is negligible (a chemical reaction of Rb with a glass becomes significant at $T \sim 150 - 200\ \text{°C}$). Concerning the reaction of Rb with sapphire, our experiments show that the reaction is absent up to temperatures $T \sim 700\ \text{°C}$. Before filling the cell with Rb, it is connected to the vacuum post and pumped out during 4 hours when heated up to $T \sim 400\ \text{°C}$. Due to the small thickness between the cell windows, it is complicated to remove gases and other impurities absorbed by surfaces of the cell windows. Therefore careful and long pumping out of thin cell (as well as nanocell) at high temperatures is important.

The most complicated and important problem is to remove water completely from surface of sapphire or garnet. Note, that in order to get a cell which will have thicknesses of Rb atomic vapor L of several hundreds μm , one should put Ti strip (which works like spacer between

the cell windows) thicker of thickness several hundreds μm . It means that the considered construction of the cell is universal for obtaining of thicknesses L in range from 5 μm to 1 mm.

1.5.2 Construction of nanocells containing atomic vapors

The construction of nanocells (the thickness of an atomic column is varies from 20 nm to several hundreds of micron) is similar with the one demonstrated on fig. 1.15 and considered in detail in [102]. In this case rectangular, smoothly polished sapphire or garnet plates, with the following sizes: width - 20 mm, height - 30 mm and thickness - 3 mm may be chosen as cell windows. The degree of finishing of a garnet polishing must be very high (more than $\lambda/10$). In order to form a nanometric gap between the cell windows, in the bottom side of the windows, by vacuum deposition, a thin strip (width is 1 mm, length is several mm and thickness - about 1 – 2 μm) of sapphire (Al_2O_3) is created.

In case of particular problems, it was obligatory to use windows with a small thickness about 0.7 mm. In those cases after the cell filling and sealing-off under the pressure of the external atmosphere, the windows were pressed to each other, particularly in the region where the stripe are absent (top of plates), decreasing the gap between the cell windows up to 20 – 30 nm. In case when the plates of ~ 0.7 mm were used, to increase plates thicknesses in the bottom part, little sapphire or garnet blocks were glued, which is well seen on fig.1.16(b). Inside is put and glued the thin sapphire pipe with the external diameter ~ 2 mm and ~ 50 mm length. For this purpose, a hole was drilled in the bottom side of the cell (where the supplementary sapphire blocks were glued) with a diameter of ~ 2 mm. Further the all construction was gathered and glued in the vacuum chamber [45].

It is important to note, that since the distances between cell windows are small, a more careful and longer pumping (~ 8 hours) at high temperatures (~ 400 °C) is necessary. On fig. 1.16(b) is given a photograph of the nanocell with a wedge-shape gap between the windows and L in the range 50 nm - 2 μm . We would like to pay attention that on this photograph, an interferometric pattern is observed, which appears as a result of the reflection of the sunlight from the internal surfaces of the nanocell windows. This is because the gap between the windows is of the wavelength λ of the sunlight. Note that the interferometric pattern is

observed up to thicknesses about $2 - 2.5 \mu\text{m}$. On fig. 1.16(b) a thermocouple can also be seen. A thermocouple is fixed so that its tip has a good thermal contact with the upper limit of the metallic Rb column inside the sapphire pipe. In order to increase the thermal contact, the tip of the thermocouple is tied to the sapphire pipe by a glass fiber.

1.5.3 Determination of the thickness of a nanocell using a laser beam

The method is based on the interferometry of reflected laser beams from two internal surfaces of the cell. Since the cell windows form a wedge, by directing the laser radiation perpendicularly to the cell, one gets three reflections, demonstrated on fig. 1.17: R_1 - reflection from the first (external) surface, R_2 - reflection from the inner gap, which is a interferometric pattern of reflections from the two internal surfaces and, as a result, contains information about the thickness of the gap; R_3 - reflection from backside surface. A nanocell can be considered as low-Q Fabry-Perot interferometer [103]. Because of this, by measuring the ratio of the intensities I_{R_2}/I_{R_1} for a certain λ , it is possible to determine the thickness L using the following relation for a Fabry-Perot interferometer [46]:

$$\frac{I_{R_2}}{I_{R_1}} = \frac{1}{R} \cdot \frac{F \sin^2(\varphi/2)}{1 + F \sin^2(\varphi/2)} \quad (1.63)$$

where R is the cell windows reflection coefficient, $F = 4R/(1 - R)^2$ and $\varphi = 2\pi\delta/\lambda = 2\pi \cdot 2L \cos\alpha/\lambda = 4\pi L/\lambda$ (α is practically ~ 0). From (1.63) it follows: the maximum of the reflection is achieved for $\varphi/2 = (2k + 1)\pi/2$ it means that $L = (2k + 1)\lambda/4$ and the minimum of the reflection (i.e. $R_2/R_1 = 0$) is obtained for $\varphi/2 = \pi k/2$ that is for $L = k\lambda/2$, where k is an integer. In case of usage of garnet plates as nanocell windows with refraction coefficient $n = 1.82$ (for $\lambda = 780 \text{ nm}$), $R = [(n - 1)/(n + 1)]^2 = 0.084$ (i.e. 8.4%), $F = 0.4$ and ratio reaches to its maximum: $R_2/R_1 = 2.85$ (maximum for thicknesses $L = (2k + 1)\lambda/4$). Hence, the maximal value of the reflection coefficient from the inner gap (R_2) achieves $R_2(\text{max}) = 2.85 \times 8.4\% \approx 24\%$ and $R_2(\text{min}) = 0$. It is important to mention, that one may obtain the maximal and the minimal coefficients of the reflection, only when the region of the uniform thickness (i.e. $L = \text{const}$) inside nanocell is larger than the diameter of laser beam. Hence, the achievement the maximal and the minimal reflection, indicates a

correctly selected homogeneous region L .

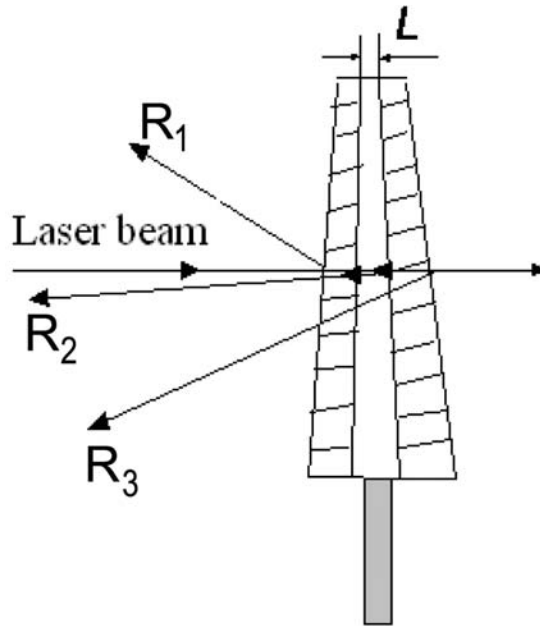


Figure 1.17: Configuration of reflections from nanocell: R_1 - reflection from first surface, R_2 - reflection from inner gap (interferometric pattern), R_3 - reflection from backside surface.

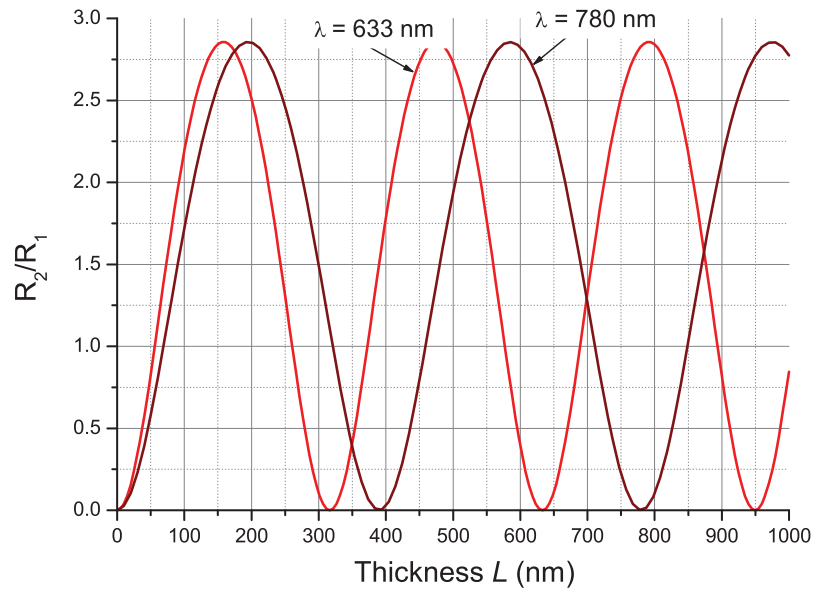


Figure 1.18: Variation R_2/R_1 as function of L for $\lambda = 633 \text{ nm}$ and $\lambda = 780 \text{ nm}$.

Thus, the intensity of the radiation transmitted through the nanocell with $L = k\lambda/2$ will have the maximal magnitude, which has the intensity of two reflections less (from the first surface (R_1) and from the backside surface (R_3)) than the initial radiation, i.e. $R_1 + R_3 \approx$

16.8% less. When the thickness $L = (2k + 1)\lambda/4$, the transmitted intensity is $16.8\% + 24\% = 40.8\%$ less than the initial intensity. Fig. 1.18 shows the variation of the intensity depending of the thickness of the cell calculated with the relation (1.63) (for certain parameters of the nanocell) for $\lambda = 633$ nm and $\lambda = 780$ nm. Since the calculated curves demonstrates a periodical variation of the reflection, the thickness L can be measured up to a multiple of $\lambda/2$, particularly it is impossible to distinguish $L = \lambda/2$, $L = \lambda$ and $L = 3\lambda/2$. In order to eliminate this complication, we did the following in our experiments: the nanocell is constructed so, that it contains the thickness $L < 100$ nm. Such kind of small thicknesses are visually observable: the reflection from this thickness is vanishing and visually this region has white color. In the marginal case of zero thickness, an “optical contact” arises and obviously no reflection appears. Hence, measuring the thickness L from the region of $L < 100$ nm, such kind of ambiguity will be eliminated. Since for the different wavelength the maxima and the minima of the reflection achieve for the different thicknesses (see fig. 1.18), in experimental conditions it is more convenient to make a measurement of the nanocell thickness directly using setup DL (for example $\lambda = 780$ nm). In this case the thicknesses $L = \lambda/2$ (390 nm), $L = \lambda$ (780 nm), $L = 3\lambda/2$ (1170 nm) etc. give minimal reflection ($R_2 = 0$), while the maxima of reflection are reached for $L = \lambda/4$ (195 nm), $L = 3\lambda/4$ (585 nm) etc. It is possible to measure the maxima and the minima with a high precision, that is to determine the thickness of the gap with the precision ± 20 nm.

The thickness of the gap can be measured as well as by the transmission intensity: for example, in the case of $L = (2k + 1)\lambda/2$ the minimum of the reflection is observed, that is in the transmitted light, the maximum of intensity will be detected, and inversely: in the case of $L = (2k + 1)\lambda/4$, when the reflection is maximal, it will be minimal intensity in transmission.

It is important to note, that in some cases, the region of homogeneous thickness has a small size. It is clearly visible, that the reflection from the region with a homogeneous thickness, has a homogeneous color, due to the interference conditions for a certain wavelength of the light. In this case, in order to increase the precision of the measurement it is necessary to decrease the laser beam diameter in a spot with a diameter $D_L = 0.3 - 0.5$ mm. The advantage of this method is the possibility to make a measurement during the experiment, this measurement being precisely localized and with high accuracy.

1.6 EIT: The coupling laser frequency is on resonance with atomic transition.

For many applications (some of them will be given in this thesis), it is important to reduce the dimensions of a cell containing atomic metal vapor where the EIT-resonance is formed, at the same time keeping good resonance parameters. The linewidth of EIT resonance in a Λ -system for the case of low laser intensity is given by $\gamma_{EIT} = 2\Gamma_{21} + \Omega^2/\gamma_N$ [78], where Γ_{21} is the coherence dephasing rate, with Ω being the Rabi frequency and γ_N the natural linewidth. For the case where nanometric-thin cells are employed [87, 88, 102, 104], Γ_{21} is highly affected by atom-wall (cell window) collisions; it takes place, though less pronounced, also for sub-millimeter thin cells [81, 106]. It is known that a unique collision with a dielectric surface of an uncoated vapor cell is sufficient to thermalize the ground hyperfine levels, with depolarization probability 0.5 – 1 (see [79] and references therein). As the thickness of an uncoated and not buffered vapor cell is reduced, the lifetime of the ground-state coherence becomes shorter because of collisions of atoms with cell windows: $\Gamma_{21} = (2\pi t)^{-1}$, where $t = L/v$ (L is the distance between windows and v is the most probable thermal velocity). Also the contrast of EIT-resonance depends strongly on Γ_{21} . Hence, one could expect that the EIT effect would completely wash out in the case of $L < 1 \mu\text{m}$ ($2\Gamma_{21} > 100 \text{ MHz}$). Nevertheless, it was demonstrated that the EIT-resonance can be observed in thin cells with thickness as small as $\sim 1 \mu\text{m}$ [87, 88]. The explanation for this non-intuitive behavior is as follows: when the coupling laser is resonant with an atomic transition, only the atoms flying nearly parallel to cell windows and hence not experiencing wall collisions do contribute to the formation of the EIT resonance.

In the paper of M. Stahler *et al.* [105] it was shown that for an ordinary cm-size cell, the excitation of D_1 -line results in greater CPT (EIT) contrast as compared to that for D_2 -line. Let us present some results from this paper. In Fig.1.19, the energy levels which are involved in EIT process are shown. In this work two lasers were used. The first was tuned to the D_1 transition of ^{85}Rb at 795 nm, and the second to the D_2 transition at 780 nm. Both laser beams had the same diameter, and they were superimposed with a beam splitter such that they traveled along the same path in the cell. Each laser beam was then circularly

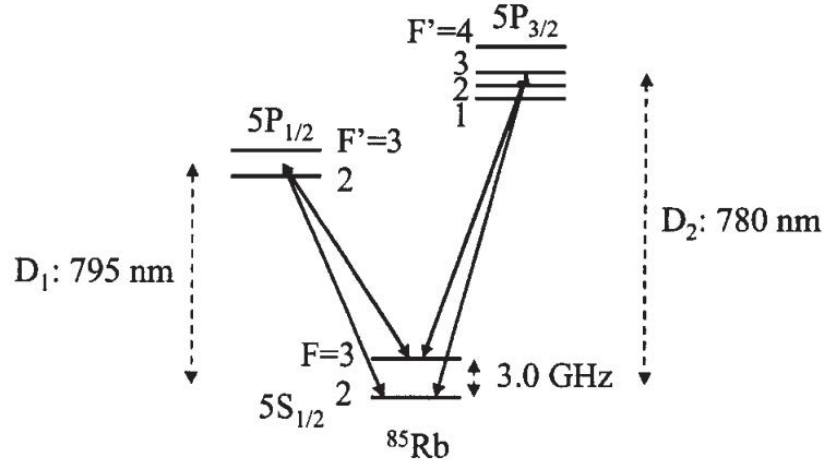


Figure 1.19: Energy levels, which are involved in EIT process

polarized, was passed through an aperture with a diameter of 5 mm and then through the vapor cell, and finally was detected with a photodiode. The cell (length, 4 cm; diameter, 2 cm) contained a natural mixture of Rb isotopes at room temperature and 0.4 kPa of Ne buffer gas. The Rb cell was surrounded by a magnetic shield, and a small longitudinal magnetic field ($\sim 10\ \mu\text{T}$) was applied to shift the magnetically sensitive CPT resonances away from the magnetically insensitive resonance ($|F=2, m=0\rangle \rightarrow |F=3, m=0\rangle$). The diode laser frequency was locked near the center of the optical transition by an active servomechanism. For measurement of the CPT (EIT) resonance, the synthesizer that produced the microwave frequency was scanned over a range of a few kilohertz near 1.5 GHz, the first subharmonic of the hyperfine transition frequency.

Figure 1.20 compares the CPT (EIT) resonance excited by the D_1 transition with that excited by the D_2 transition under the same experimental conditions. Each trace was normalized to the Doppler absorption value that was present when the fields were in optical resonance but out of CPT (EIT) resonance. It is clear that the CPT (EIT) width is smaller for D_1 excitation, and the contrast is larger. The contrast for D_1 excitation is close to 10%, whereas for D_2 excitation the contrast is near 2%.

So far, it was not verified whether this statement holds also for the case of NTC by comparing the measured EIT contrast with that observed earlier for the D_2 line [87, 88]. Switching from D_2 line to D_1 line is also expected to be favorable for forming the EIT-resonance in the fluorescence spectrum when the cell thickness is $\lambda/2$ (this was not attainable

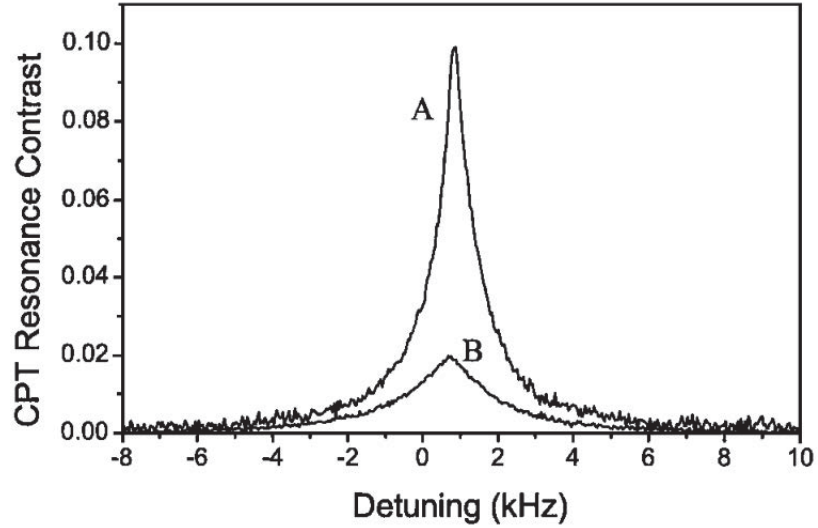


Figure 1.20: CPT resonance for excitation on A, the D_1 transition and B, the D_2 transition with a resonant laser intensity of $160 \mu\text{W}/\text{cm}^2$.

for D_2 -line excitation). It should be noted that in the case of the NTC the key parameter for EIT (equally for absorption and fluorescence) is not the value of L itself, but L/λ ratio, that is why the high contrast obtained for $L = \lambda$ can strongly reduce, when L is further decreased [87, 88].

The main aims of the present study are: (i) to check whether the EIT resonance in a Λ -system on D_1 -line for NTC with $L = \lambda$ is advantageous as compared with the case of D_2 excitation and to study the EIT contrast and linewidth dependence on coupling laser detuning; (ii) to investigate the EIT behavior under the further reduction of cell thickness to $L = \lambda/2$, also in fluorescence spectrum. One of the cell miniaturization usage is to miniaturize the optical devices such as magnetometers with sub-micrometric spatial resolution and precise frequency references.

The experimental arrangement is presented on section 1.2.

1.6.1 EIT: thickness of the cell $L = \lambda$

The $L = \lambda$ case is of a special interest, since this is the minimum thickness when it is possible to form a high-contrast EIT signal. For $L < \lambda$, the Dicke effect causes strong spectral narrowing and absorption increase for the probe laser, which results in reduction of EIT contrast (see below). Relevant energy levels of ^{85}Rb D_1 line involved in EIT are shown in Fig.1.21. The detuning Δ of a coupling laser from $F = 3 \rightarrow F' = 3$ transition varies in

0 – 100 MHz range, while the probe laser is scanned across $F = 2 \rightarrow F' = 2, 3$ transitions.

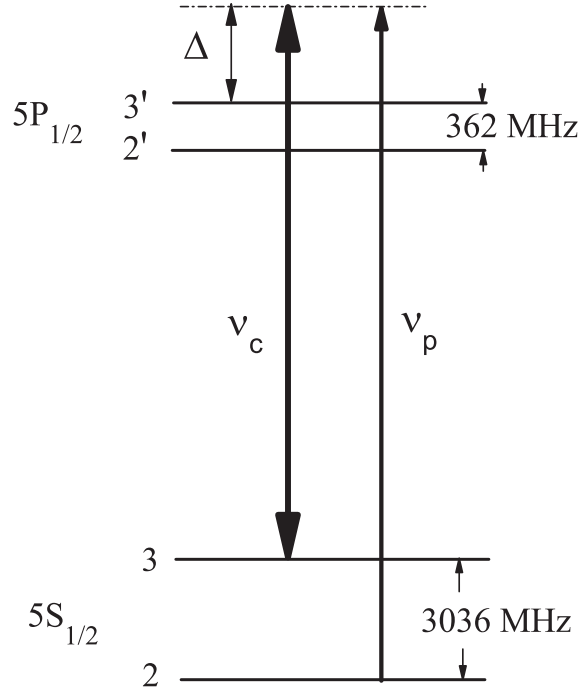


Figure 1.21: Relevant energy levels of ^{85}Rb D_1 line involved in EIT process.

The EIT linewidth and amplitude (contrast) as a function of blue detuning Δ of the coupling laser for $L = \lambda$ can be evaluated from the experimental and theoretical transmission spectra shown in Fig. 1.22. The side-arm temperature of NTC is 140 °C, $P_c \approx 20$ mW. In order to get more prominent EIT-resonance for the large values of detuning, the probe laser radiation power was increased to 1 mW. As it is seen on Fig 1.22, the increase of detuning Δ from 0 to 40 and 85 MHz results in rapid broadening of EIT-resonance linewidth from 25 MHz to 50 and 80 MHz (full width at half maximum, FWHM) correspondingly, meanwhile the EIT amplitude rapidly decreases. This behavior has the following physical explanation. For the case of an exact atomic resonance ($\Delta = 0$), mainly atoms flying parallel to windows, which do not experience frequent collisions with the windows, contribute to formation of the EIT-resonance. The interaction time for these atoms is $\tau_D = D/v$, where D is the laser beam diameter ($D \gg L$). When the coupling laser is detuned from an atomic transition by a value of Δ , only the atoms having $v_z = 2\pi\Delta/k$ velocity projection contribute to the formation of EIT, and for these atoms the flight time between the cell windows shortens with the detuning:

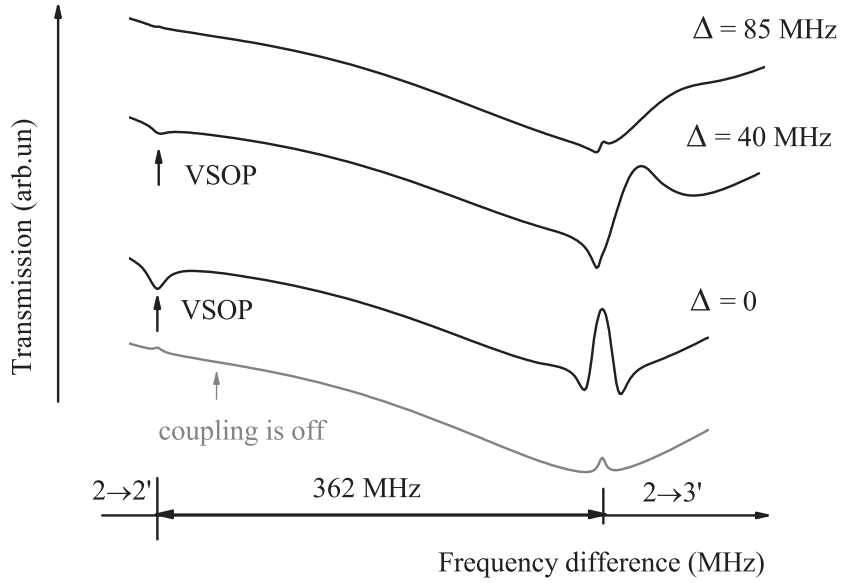
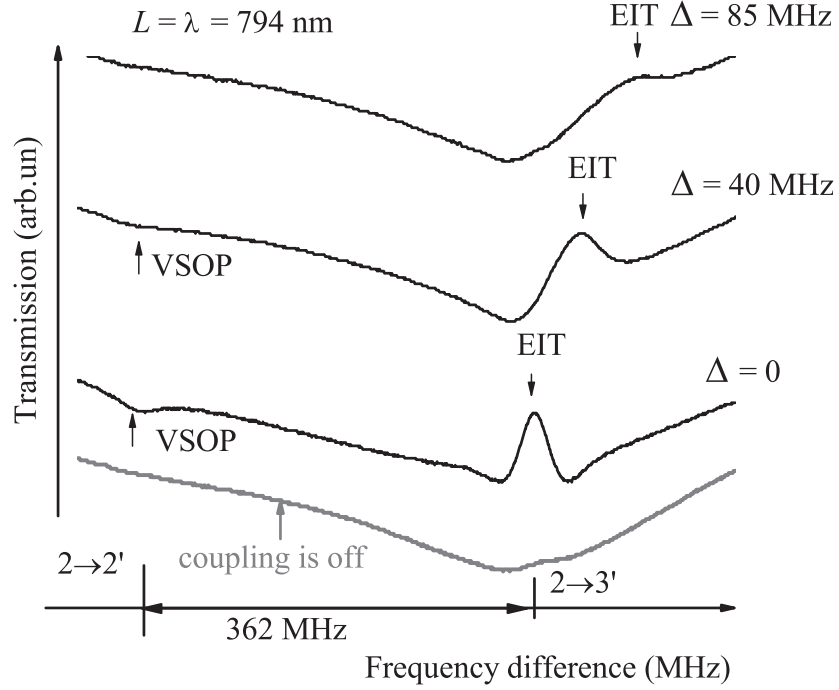


Figure 1.22: EIT spectra for $L = \lambda = 794$ nm and different detunings Δ of coupling laser from $F = 3 \rightarrow F' = 3$ transition. The spectra are shifted vertically for convenience. The lower grey curve is the transmission spectrum when the coupling laser is off. Graph *a*: experiment; graph *b*: numerical calculations for the experimental conditions, $\Omega_c = 1.3\gamma_N$, $\Omega_p = 0.3\gamma_N$, $\gamma'_{21} = 6$ MHz. Additional dephasing rate $\gamma'_{21}(\Delta)$ is responsible for the EIT broadening seen for $\Delta \neq 0$ (see the text).

$\tau_L = L/v_z = kL/(2\pi\Delta)$. This causes frequent quenching collisions of atoms with the cell windows leading to the increase of $\gamma'_{21}(\Delta)$ (which is equal to $1/(2\pi\tau_L)$) and consequently, to strong linewidth broadening and contrast reduction of the EIT-resonance. For this case γ_{EIT} can be described by a simple expression.

$$\gamma_{EIT}(\Delta) = \gamma_{EIT}|_{\Delta=0} + 2\gamma'_{21}(\Delta), \quad (1.64)$$

Replacing the gap thickness by a justified parameter $L_{eff} = L/2$, we get $\gamma'_{21}(\Delta) = \Delta/\pi$ for $L = \lambda$. From (1.64) for $\Delta = 40$ and 85 MHz we have $\gamma_{EIT} = 50$ and 79 MHz, correspondingly, which is in good agreement with the experimental values. We should note that measurement of EIT-resonance linewidth γ_{EIT} at large coupling laser detuning could serve as a convenient tool to study atom-window collisions and properties of window material.

When the coupling laser is off, velocity selective optical pumping (VSOP) peaks located exactly at the atomic transitions and exhibiting reduction of absorption appear in the transmission spectrum of the probe (grey lines) [87].

When the coupling is switched on with $\Delta = 0$, a high contrast EIT-resonance is superimposed on the VSOP at $F_g = 2 \rightarrow F_e = 3$ transition, while VSOP resonance on $F_g = 2 \rightarrow F_e = 2$ transition is inversed, demonstrating an absorption increase. The latter is caused by a transfer of atoms from $F_g = 3$ to $F_g = 2$ by the coupling laser, thus increasing the probe absorption on $F_g = 2 \rightarrow F_e = 2, 3$ transitions.

One can conclude that the best EIT-resonance parameters for the case of NTC are attained for $\Delta = 0$. This behavior completely differs from that observable for ordinary 1 - 10 cm long cell where EIT formed on the wings of the Doppler-broadened absorption line can get narrower [123].

Fig. 1.23 shows the transmission spectrum of the probe laser for $L = \lambda$ ($\lambda = 794$ nm) when the 20 mW coupling laser radiation is resonant with $F = 3 \rightarrow F' = 3$ transition, while the 0.04 mW probe laser radiation frequency is scanned across the $F = 2 \rightarrow F' = 2, 3$ transitions. The NTC's side-arm temperature is 140 °C. The linewidth of EIT-resonance is 25 MHz FWHM, while the contrast defined as the ratio of EIT amplitude to the height of the shoulders is 34 % (the peak value of the absolute absorption is 4 %). For a higher coupling

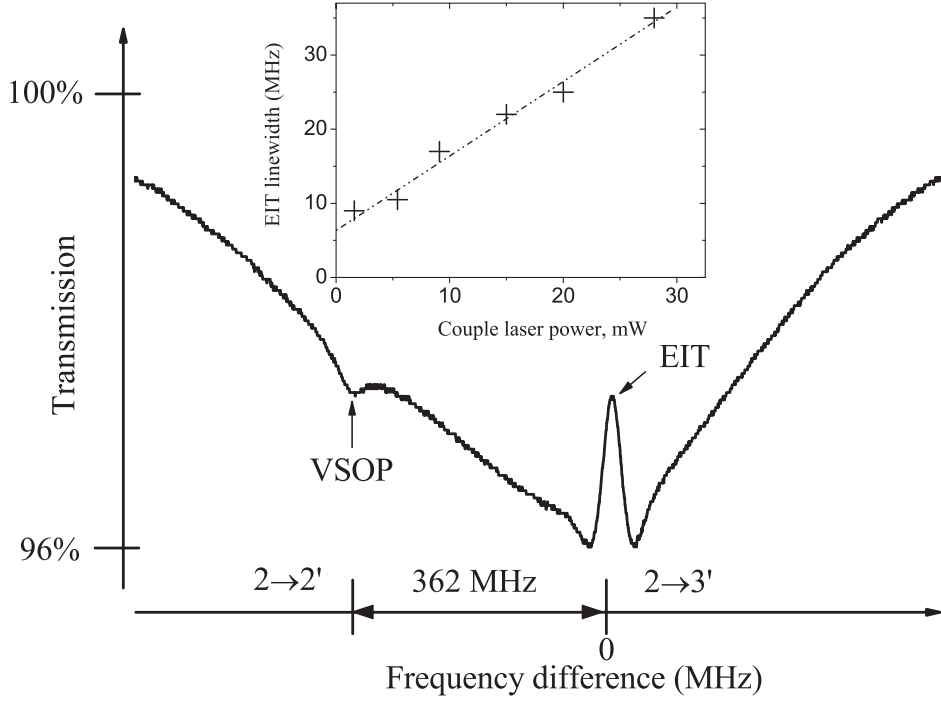
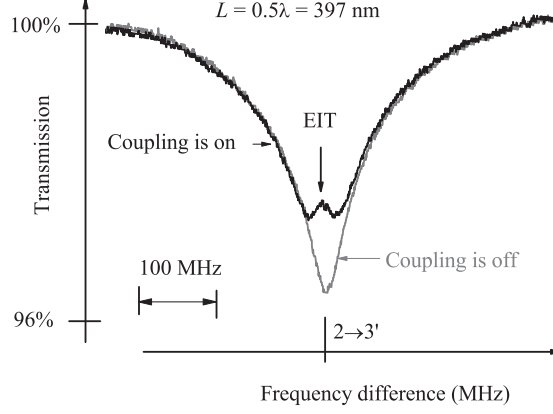


Figure 1.23: EIT spectrum for ^{85}Rb D_1 line. $L = \lambda = 794$ nm. Coupling laser is resonant with $F = 3 \rightarrow F' = 3$ transition, probe laser is scanned across $F = 2 \rightarrow F' = 2, 3$ transitions. Inset: dependence of the EIT linewidth on the coupling laser power.

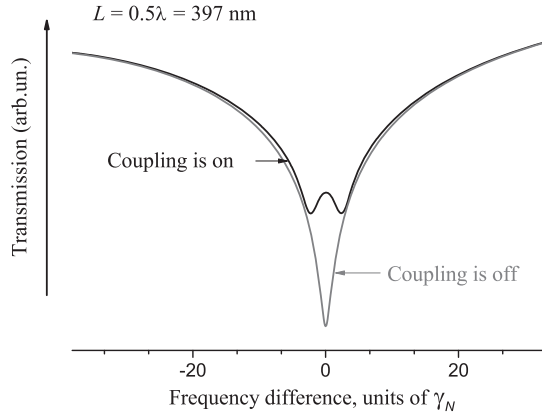
laser radiation power, 28 mW, the linewidth broadens to ~ 35 MHz, and the contrast reaches nearly 40 %. Note that the best contrast for D_2 line obtained under similar experimental conditions was 5 - 6 % [87, 88]. The inset in Fig. 1.23 presents the EIT-resonance linewidth as a function of the coupling laser power. The intersection of the curve with the vertical axis gives the residual coherence dephasing rate of $\gamma'_{21} = 6$ MHz, which is caused by atom-atom, atom-wall collisions in NTC, time-of-flight broadening, as well as due to the fact that the lasers are not coherently coupled [78].

1.6.2 EIT: thickness of the cell $L = \lambda/2$

Earlier it was demonstrated that absorption and fluorescence spectra undergo dramatic changes when the thickness of NTC is reduced from $L = \lambda$ to $L = \lambda/2$ where the most pronounced difference is observed (Dicke-type coherent narrowing effect). Particularly, the sub-Doppler absorption spectrum for $L = \lambda/2$ is nearly 3-fold narrower than that for $L = \lambda$,



(a)



(b)

Figure 1.24: Probe laser transmission spectrum for ^{85}Rb D_1 line. $L = \lambda/2 = 397$ nm. Coupling laser ($P_c = 27$ mW) is resonant with $F = 3 \rightarrow F' = 3$ transition, probe laser ($P_p = 0.04$ mW) is scanned across $F = 2 \rightarrow F' = 2, 3$. Grey line: spectrum when coupling laser is off. Graph *a*: experiment; graph *b*: numerical calculations for the experimental parameters, $\Omega_c = 1.5\gamma_N$, $\Omega_p = 0.06\gamma_N$, $\gamma'_{21} = 6$ MHz.

while showing the same peak absorption value [103, 108, 109]. Moreover, as it was shown recently, it is impossible to form any type of sub-Doppler dip (i.e. VSOP resonance) for $L = \lambda/2$, neither in transmission nor in fluorescence spectra, even for the laser intensity as high as several tens of W/cm^2 , as opposed to $L = \lambda$ where only a few mW/cm^2 probe laser intensity is sufficient for a dip formation. For this reason, the $L = \lambda/2$ case is of a particular interest for EIT-resonance formation.

The striking point of this study is that it is possible to form an EIT resonance (a narrow peak of reduced absorption) for the thickness $L = \lambda/2$ already at a coupling laser intensity as

low as $\sim 0.1 \text{ W/cm}^2$ (see Fig. 1.24(a)). The grey curve shows the 120 MHz-wide sub-Doppler transmission spectrum for $L = \lambda/2$ when the coupling laser is off. The theoretical spectra for the parameters matching exactly the corresponding experimental conditions of Fig. 1.24(a) are shown in Fig. 1.24(b) (for theoretical model, see Section 1.5).

The linewidth of the resonant fluorescence spectrum for $L = \lambda/2$ is 70 - 80 MHz, which is ~ 1.7 times narrower than that of the transmission linewidth. Yet it is possible to form a narrow dip of reduced fluorescence when $P_c = 0.1 \text{ W/cm}^2$, which is a manifestation of EIT for $L = \lambda/2$. Also for this case there is a good agreement of experiment and theory.

Chapter 2

The EIT-resonance splitting in a magnetic field using a nanocell and a microcell.

Introduction

There is only few works about EIT-resonance in a magnetic field. Results of the study of EIT-resonance splitting in a relatively low magnetic field (< 40 G) are presented in [1, 11, 78, 87, 110–113]. The behavior of EIT-resonances in magnetic fields up to several hundred gauss for Na atoms was reported in [114, 115]. In [114] the CPT phenomenon in a sodium atomic vapor was investigated. The black lines in the fluorescence path have been classified according to the nonabsorbing coherent superposition of ground states to which they correspond. The CPT dips corresponding to different nonabsorbing coherent superpositions have different contrasts. This has been explained in terms of pumpings toward levels not resonant with the laser light, and it has been shown that the relaxation of the coherences is not relevant for the experimental conditions analyzed here. The role of the Doppler broadening has been discussed. From a comparison of the experimental data with the predictions obtained with the Rabi-Breit formula R. Höller *et al.* conclude that they have observed the whole spectrum of dark resonances that correspond to the dark superpositions of two Zeeman sublevels of two different ground-state hyperfine components. Thus all possible dark resonances within the sodium D_1 -line have been demonstrated together with the work in which dark coherent

superpositions of sublevels of the same ground-state hyperfine component were considered [114]. The observation of the whole spectrum of the dark resonances in the Λ -systems within the D_1 -line is a necessary step for the future study of the coherence transfer among different Λ -systems. A possible new method for detecting collision-induced coherence transfer between two or more Λ -systems is proposed. The method relies on the possibility of establishing within a very small region two or more black lines by use of only a two-frequency laser light and strong magnetic fields.

In [115] high-resolution spectroscopy of hyperfine Zeeman components in a sodium atomic vapor has been performed by a coherent population trapping technique. In the experiment the simple configuration of a single laser source with a frequency-swept double-pass acousto-optic modulator was used. Well-resolved CPT dip signals in the presence of longitudinal or transverse static magnetic fields were nicely explained by a theory based on two-photon resonance.

In up mentioned papers, EIT (CPT, dark resonance) was considered as a powerful tool for the hyperfine Zeeman spectroscopy. The study of behavior of EIT-resonances in strong magnetic fields is of interest not only from purely scientific but also practical points of view. From the scientific point of view, it is important to know the properties of individual atomic transitions between the splitted Zeeman sublevels, because it is known that the probabilities of atomic transitions change significantly and the frequency shifts of atomic transitions deviate from the linear law even in moderate magnetic fields [116,117]. For practical applications, using the EIT-resonances will allow the formation of narrow optical resonances (of a subnatural width) strongly shifted relative to the atomic transitions (the frequency shift can reach several gigahertz). A further possible application of EIT in high magnetic fields is related to the possibility of selecting a given Λ interaction scheme, including transitions that are forbidden in zero magnetic field, in a multilevel atomic system. This can have an important application in force-assisted velocity-selective EIT laser cooling in which the simultaneous action of two schemes (for example Λ and V) is necessary. This is often problematic in the transition $F = 1 \rightarrow F = 1$ in σ^+, σ^- fields: the V interaction scheme is quickly depleted because the transition $|F_g = 1, m_F=0\rangle \rightarrow |F_e = 1, m_F = 0\rangle$ is forbidden in zero magnetic field, but the related transition probability is strongly increasing with increasing magnetic

field.

The absence of works on EIT in higher fields (> 500 G) is probably due to the relative complexity of producing strong homogeneous magnetic fields, since the EIT-resonances are formed in cells with a length of a few centimeters filled with atomic alkali vapors and the low limit of laser scanning region.

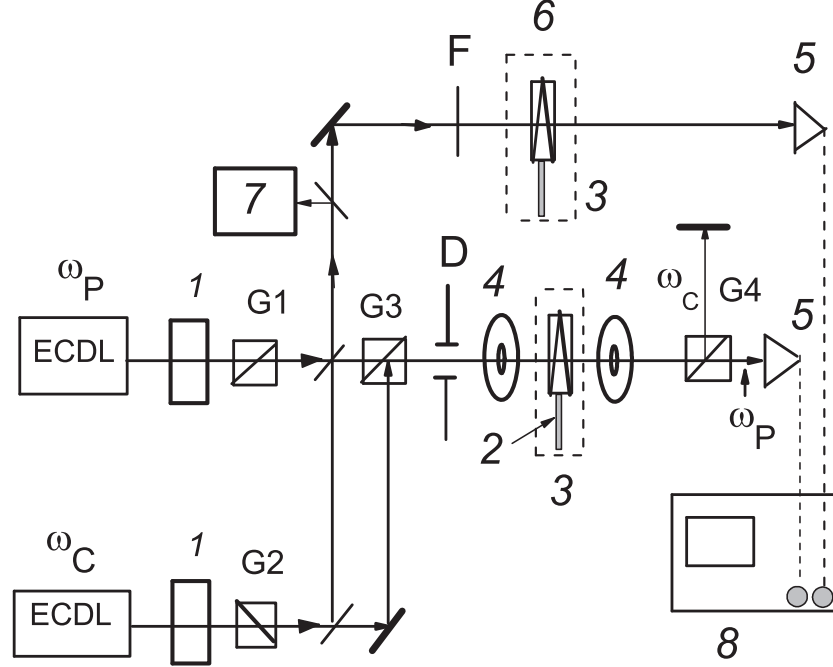
The use of a thick column of vapors is an important advantage, since it becomes possible to use strong permanent magnets that can create fields of several thousand gauss at short range. The fields of such permanent magnets are strongly nonuniform, and the gradient can reach ~ 200 G/mm, which excludes the possibility of using cells of several centimeters long; however, with a small thickness of the vapor column, the change in B is four or five orders of magnitude smaller than the measured value of B itself. This remarkable property of thin cells has been used in the studies of absorption spectra of atomic vapors in strong magnetic fields [87, 118–120]. One more advantage is the absence of sidebands of the EIT-resonance that are formed in cells of several centimeters long [121]. In Chapter 1 it was reported the possibility of forming a high-contrast EIT-resonance (a 40% contrast was reached) using an ETC with vapor column thickness $L = \lambda$ in the Λ -system of the D_1 -line of ^{87}Rb atoms, where the high contrast of the EIT-resonance allowed us to easily record the splitting in a magnetic field of ~ 10 G.

In this chapter the experimental and theoretical results of EIT-resonance splitting in strong magnetic field for the D_1 -line of ^{85}Rb and ^{87}Rb are given.

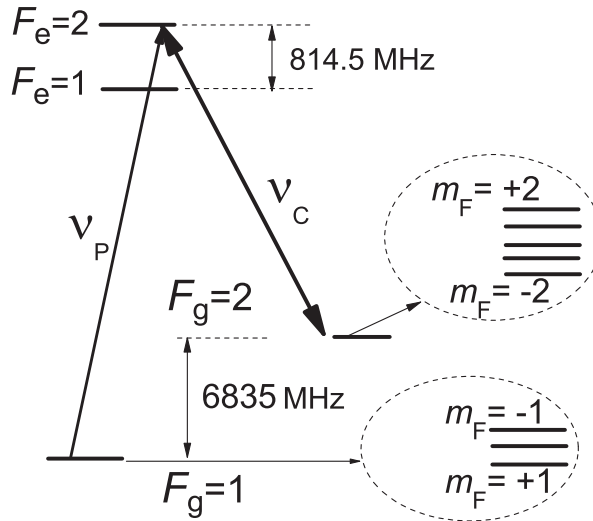
2.1 Experimental technique

In this study, we used an ETC with the thickness of the column of atomic vapors being variable (in the vertical direction) in the range of $0.35\ \mu\text{m}$ [122]. Rectangular windows with a size of 25×30 mm and thickness of 2 mm were made from crystalline sapphire. The c axis was perpendicular to the surface of a window, which significantly decreases the birefringence. The surfaces of sapphire windows were carefully polished (local roughness < 5 nm). To form a wedge-shaped gap (between the internal surfaces of windows), a platinum strip $5\ \mu\text{m}$ thick was placed in the lower part between the windows. The side extension of the ETC was filled

with natural rubidium (containing isotopes ^{85}Rb (72 %) and ^{87}Rb (28%)). The presence of a relatively large region ($\sim 1 \times 1 \text{ mm}$) of a submicron gap with constant thickness $L \sim \lambda$ is an important condition for the successful application of the ETC in this study.



(a)



(b)

Figure 2.1: (a) Schematic of the experimental setup: (ECDL) narrow-band diode laser, (1) Faraday insulator, (G1, 2, 3, 4) Glan polarizers, (2) main ETC, (3) oven, (4) PMs, (5) photodiodes, (6) auxiliary ETC, (F) optical filter, (7) device for stabilizing the coupling laser frequency, (8) digital oscillograph, and (D) an aperture. (b) The levels of the D_1 -line of ^{87}Rb atoms involved in formation of the EIT-resonance. In the presence of a magnetic field, different sublevels m_F take part in the formation of the EIT-resonance.

To form such a gap, one of the windows (the surface that forms the submicron gap) was chosen to be weakly convex with a radius of curvature $R > 100$ m. It is important to note that a deviation of the gap thickness from $L = \lambda = 794$ nm by $\pm 10\%$ does not reduce the contrast and spectral width of the EIT-resonance significantly. The oven for the ETC is made from nonmagnetic materials (in order to reduce the magnetic field, we use a noninductive winding of the heating coil) and has two holes to transmit laser radiation. The oven consists of two heaters: the first one for heating the windows and the second one for heating the sapphire extension containing Rb. The temperature of the upper boundary of the column of metallic Rb was $\sim 120^\circ\text{C}$, which provides a concentration $N \sim 2 \times 10^{13}$ cm³. In order to exclude condensation of Rb vapors on the windows of the ETC, the temperature of the windows was maintained at $\sim 140^\circ\text{C}$. To ensure necessary thickness of the gap $L = \lambda$, the oven (and the ETC inside it) was mounted on a nonmagnetic table with the possibility of smoothly moving it in the vertical direction. The other details are described in Chapter 1.

A schematic of the experimental setup for studying the EIT-resonance is presented in Fig. 2.1a. Radiation beams of two continuous wave narrow-band (with the width of about 1 MHz) extended cavity diode lasers (ECDL) were used, one of which (the coupling laser) had fixed frequency ν_C and the other of which (with a tunable frequency) was probe laser ν_P . With the help of Glan prisms G1 and G2, polarizations of the coupling and probe lasers were made linear and mutually perpendicular. Both radiation beams ~ 1 mm in diameter were superimposed by Glan prism G3 on each other and directed to ETC (2) placed inside an oven (3). Portions of probe ν_P and coupling ν_C beams were directed to additional (auxiliary) ETC (6) with thickness $L = \lambda$ to form a frequency reference. Note that, if coupling beam ν_C is absent, a velocity-selective optical resonance (VSOR) located exactly at the atomic transition [99] is formed in the spectrum of the additional ETC. If the coupling beam ν_C is also present, then, in the case of an exact resonance of ν_C with the corresponding atomic transition, a EIT-resonance is also formed, which superimposes the VSOR in the spectrum. Such an experiment allows one, using the frequency difference between the EIT-resonance and the VSOR, to determine the detuning Δ of the frequency ν_C from the exact resonance (see below). The radiation beams were recorded by FD-24K photodiodes (5). The signals from photodiodes were amplified by an operational amplifier and then directed to a Tektronix

TDS2014B four-beam digital oscillograph (8). Part of radiation of the laser ν_C was directed to system (7) in order to form an error signal and stabilize its frequency [99]. Magnetic fields weaker than 200 G were formed by a system of Helmholtz coils, inside which the ETC and the oven were placed (the coils are not shown in Fig. 2.1a). To form magnetic fields stronger than 200 G, we used disk-shaped PMs 60 mm in diameter and about 30 mm thick with a hole 2 mm in diameter to transmit the laser beam. The permanent magnets were mounted on two nonmagnetic tables the distance between which could be smoothly varied. Prism G4 removed radiation of the coupling laser, so that only radiation of the probe laser was recorded. Neutral filters F were used to ensure the required powers of laser beams. We studied the Λ -system of the D_1 -line of ^{87}Rb atoms shown in the diagram in Fig. 2.1b: frequency ν_C is in resonance with the $2 \rightarrow 2'$ transition (the prime labels the upper levels), and frequency ν_P is scanned over the $1 \rightarrow 1', 2'$ transitions. In the presence of an external magnetic field, Λ -systems involving different sublevels m_F are formed. Powers of the coupling P_C (130 mW) and the probe P_P (< 1 mW) lasers were chosen so that the EIT-resonance had a minimal spectral width and a good contrast.

2.2 The splitting of the EIT-resonance on three components: ^{87}Rb , D_1 -line, the vapor thickness $L = \lambda$

Figure 2.2 presents the transmission spectrum of the vapors for $L = \lambda$ (with zero magnetic field) containing an EIT-resonance.

The contrast of the EIT-resonance (defined as the ratio of the EIT-resonance amplitude to the value of the peak absorption) is about 40% with spectral width $\gamma_{EIT} \approx 30$ MHz. Note that close values of the EIT-resonance parameters were obtained in [110] for the same Λ -system of the D_1 -line of ^{87}Rb using an ordinary cell with $L = 3$ cm: EIT-resonance contrast of about 60% and $\gamma_{EIT} \approx 20$ MHz. Thus, along with the advantages of an ETC indicated above, reduction of the thickness of a vapor column by more than four orders of magnitude ($3 \text{ cm}/794 \text{ nm} = 3.8 \times 10^4$) does not significantly reduce the EIT-resonance parameters, which is important for minimizing the cell size in practical applications [80]. The weak dependence of the EIT-resonance parameters on thickness L is explained by the fact that, if the coupling

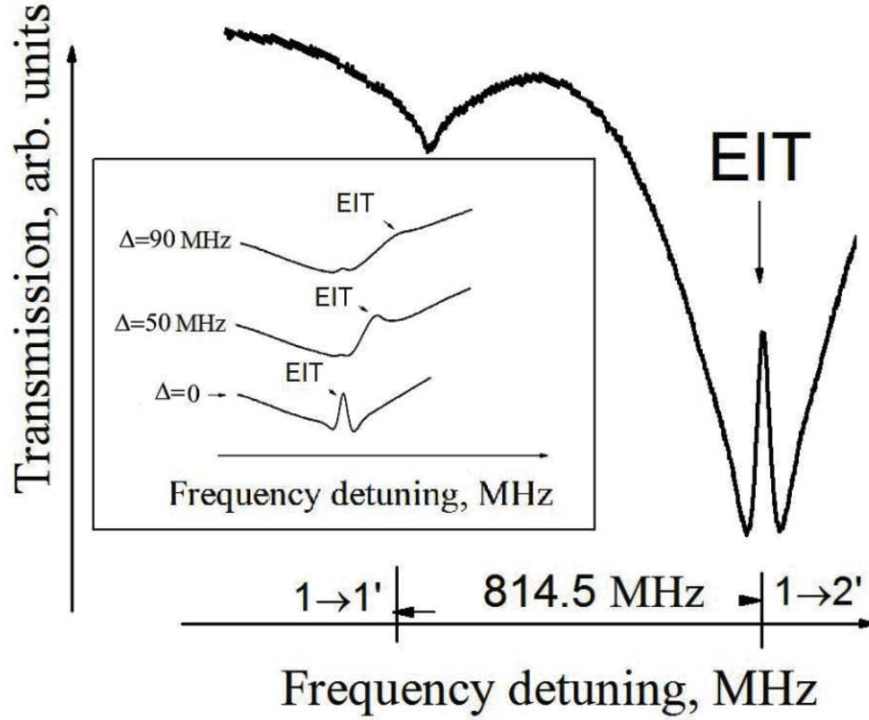


Figure 2.2: An extremely thin cell with $L = \lambda = 794$ nm: the transmission spectrum of ν_P , the EIT-resonance is indicated by an arrow, the EIT-resonance contrast is $\sim 40\%$, and $\gamma_{EIT} \approx 30$ MHz. The behavior of the EIT-resonance amplitude and γ_{EIT} in the presence of detuning Δ for the ν_C frequency are shown in the inset.

laser frequency is in exact resonance with the corresponding atomic transition (Fig. 2.1b), only atoms flying parallel to the windows of an ETC and practically not colliding with them take part in the formation of a EIT-resonance. Therefore, for these atoms, the decrease of L weakly affects the EIT-resonance. The dependence of the amplitude and width of the EIT-resonance on the magnitude of detuning Δ of coupling laser frequency ν_C from the frequency of the 2-2' atomic transition is shown in the inset of Fig. 2.2. One can see in the figure that, as Δ increases, the EIT-resonance amplitude rapidly decreases, with its spectral width increasing at the same rate (the EIT-resonance can have a dispersion form at large Δ). This is the case because, at large Δ , the EIT-resonance is formed by the atoms flying in the direction of laser beam z with velocity $V_z = 2\pi\Delta/k$, thus the time of flight of the atoms from one wall of the ETC to the other $\tau = L/V_z$ is short (for $L \sim 1 \mu\text{m}$ and $V_z = 300$ m/s, $\tau \sim 3$ ns). This fact gives rise to a rapid increase in the coherence dephasing rate (CDR), which is the determining factor that governs the characteristics of a EIT-resonance [1, 78]. The rapid increase in the CDR significantly broadens the EIT-resonance and reduces its amplitude.

Interestingly, with the use of an ordinary cell several centimeters long, the situation is quite the reverse – namely, narrower EIT-resonances are formed at $\Delta \neq 0$ [123].

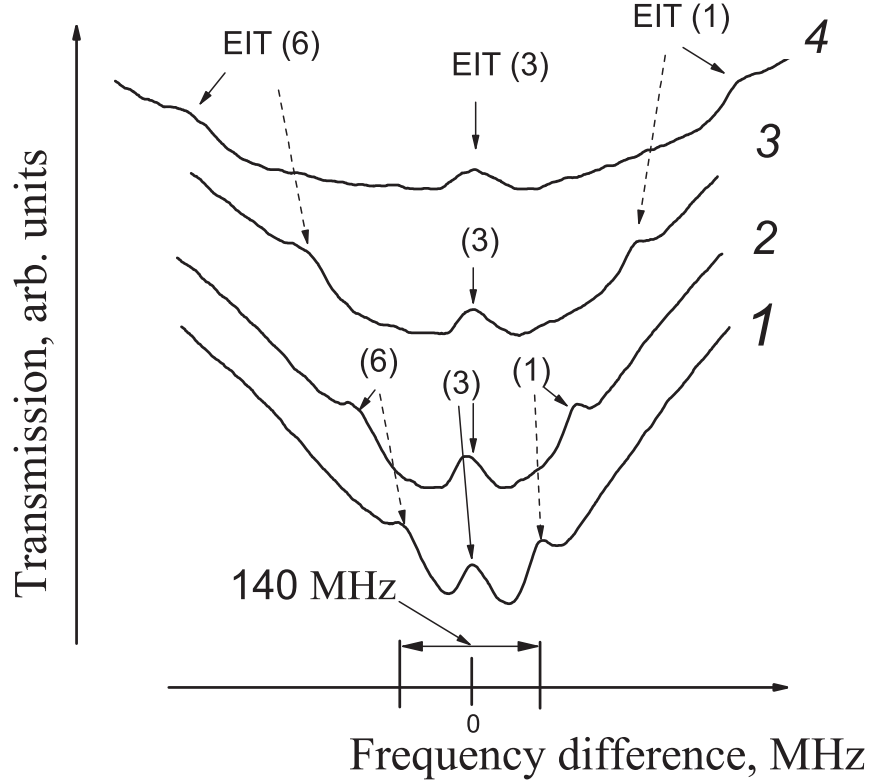


Figure 2.3: An extremely thin cell with $L = 794$ nm: curves 1–4 are the transmission spectra in the magnetic fields of 50, 80, 120, and 200 G, respectively, in which EIT(1), EIT(3), and EIT(6) indicated by arrows are present.

Figure 2.3 shows the transmission spectra of probe radiation, where the EIT-resonances are indicated by arrows (here and below, a longitudinal magnetic field $\mathbf{B} \parallel \mathbf{k}$ is applied, where \mathbf{k} is the wave vector of the laser radiation). As the magnetic field increases (50, 80, 120, and 200 G for curves 1-4, respectively), the frequency distance between components (1), (3), and (6) increases (the number in parentheses corresponds to the number described in the Fig. 2.8 and to the Λ -systems presented in Fig. 2.4).

Zeeman splitting of the ground levels $F_g=1,2$ described by quantum number m_F and the Λ -systems involved in EIT-resonance components formation are presented in Fig. 2.4.

In the formation of components (1), (3), and (6), three Λ -systems with the following lower sublevels (see the Fig. 2.4) of the hyperfine structure ($F_g = 1, m_F; F_g = 2, m_F$) take part: (1, +1; 2, +1), (1, 0; 2, 0), and (1, -1; 2, -1). Apart from the frequency shift, a certain spectral broadening of the EIT-resonance takes place because $\Delta \neq 0$. Since the magnitude

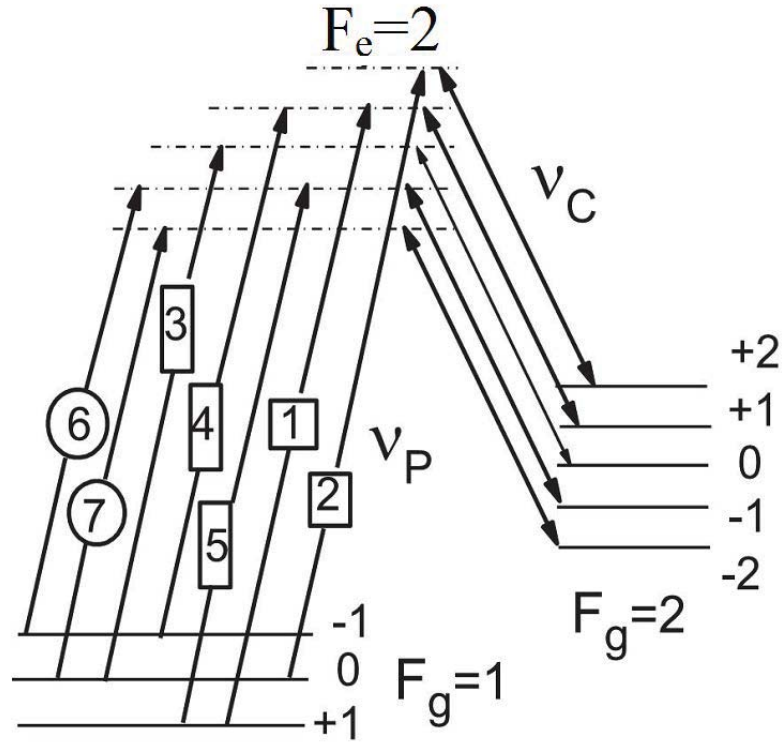


Figure 2.4: EIT for ^{87}Rb D_1 line. Seven Λ -systems are formed in magnetic field. For $B < 300$ G, EIT components marked by the same symbol (circle, square or rectangle) have the same frequency, i.e. $\nu_6 \cong \nu_7; \nu_1 \cong \nu_2; \nu_3 \cong \nu_4 \cong \nu_5$.

of detuning Δ strongly affects the EIT-resonance parameters (see the inset in Fig. 2.2), it is necessary to know the dependence of Δ with the magnetic field strength.

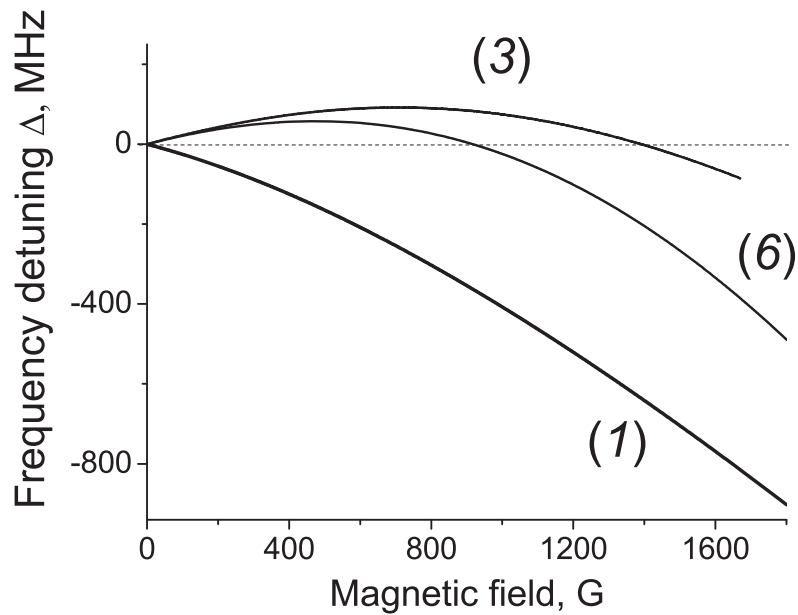


Figure 2.5: Dependence of the detuning Δ of the ν_C frequency on the distance of corresponding transitions for EIT-resonances (1), (3), and (6) on the magnetic field (see text).

Figure 2.5 shows the dependence of the detuning Δ of the coupling laser frequency ν_C on the magnetic induction for several upper levels. For EIT-resonances (1), (3), and (6), the behavior of detunings Δ of the coupling laser frequency ν_C from the frequencies of atomic transitions ($2, m_F = +1 \rightarrow 2', m_F = +2$), ($2, m_F = 0 \rightarrow 2', m_F = +1$), and ($2, m_F = 1 \rightarrow 2', m_F = -2$), respectively, is shown. The horizontal dashed line shows zero detuning. One can see in Fig. 2.5 that, for the EIT(1), $|\Delta|$ rapidly increases already in fields stronger than 350 G and, consequently, the EIT(1) is absent (see also further Fig. 2.8). For the EIT(6), $|\Delta|$ also rapidly increases in fields stronger than 1200 G and, consequently, this resonance is absent. For the EIT(3), $|\Delta|$ rapidly increases in the fields stronger than 1600 G; consequently, this EIT-resonance should be present in the transmission spectrum in weaker fields.

Figure 2.6 presents portions of spectra containing EIT-resonances (indicated by arrows).

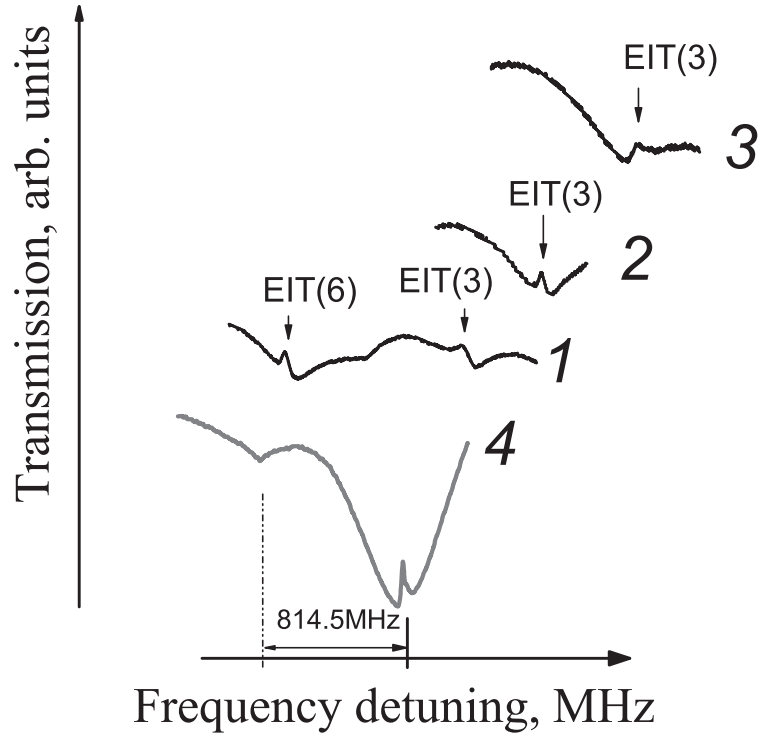


Figure 2.6: The extremely thin cell with $L = 794$ nm: 1-3 fragments of the transmission spectra containing EIT (6) and EIT (3) (indicated by arrows) with a magnetic field of 725, 1220, and 1650 G, respectively; 4 is the transmission spectrum of the ETC with $L = 794$ nm at $B = 0$ (the VSOR and the EIT-resonance coincide in frequency).

It is interesting to note that, as follows from the curve for EIT(3) (Fig. 2.5), $\Delta \approx 0$ in

fields about 1300 G; therefore, a spectrally narrow EIT(3) is observed on curve 2, while the EIT(3) is broadened at $B = 725$ and 1650 G (curves 1 and 3). The inset in the upper left part of the Fig. 2.6 shows the Λ -system with magnetic sublevels m_F and also detuning Δ of the coupling laser frequency from the corresponding upper level of the Λ -system. Note that one can control the magnitude of Δ by changing the frequency ν_C of the coupling laser. We will show below that this is feasible.

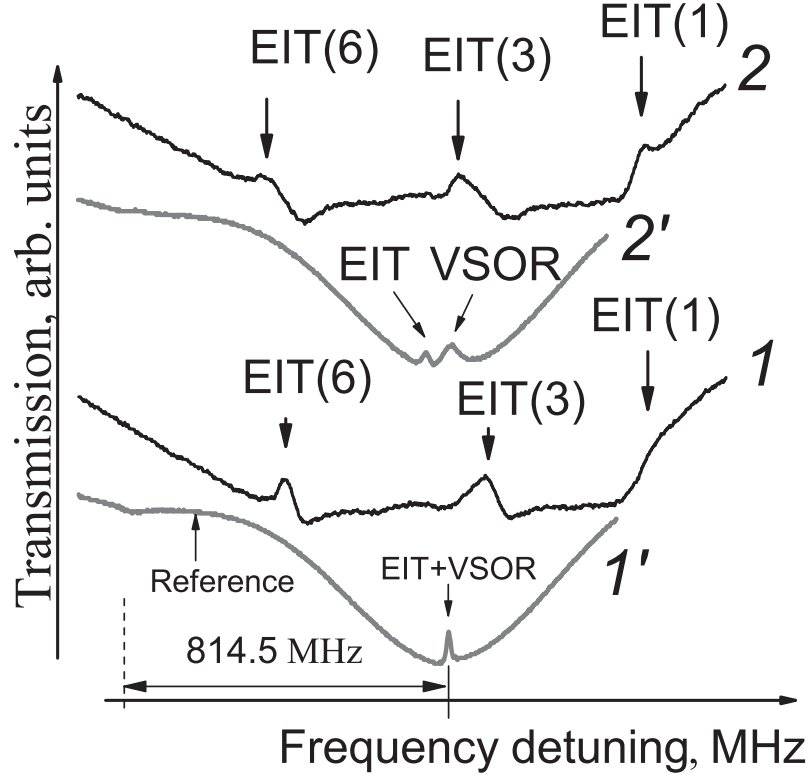


Figure 2.7: An extremely thin cell with $L = 794$ nm, $B = 350$ G: (1) transmission spectrum containing EIT(3) and EIT(6), while EIT(1) is very small; (1') frequency reference in which the EIT and the VSOR are superimposed on one another; (2) spectrum with the ν_C frequency chosen so that the condition $\Delta \approx 0$ is satisfied; and (2') frequency reference with the EIT and the VSOR shifted relative to each other.

Curve 1 in Fig. 2.7 shows the transmission spectrum at $B = 350$ G. One can see that EIT(3) and EIT(6) are present, while EIT(1) has a small amplitude and is strongly broadened (because of relatively large detuning Δ). Curve 1' is the frequency reference, on which one can see the EIT-resonance and the VSOR. These spectral features coincide in frequency and, consequently, are superimposed on each other. This fact suggests that the frequency ν_C of the coupling radiation is in resonance with the $2 - 2'$ transition. Curve 2 in Fig. 2.7 shows the transmission spectrum with the corresponding decrease in frequency ν_C of the coupling

laser so that (using curve 1 in Fig. 2.5) condition $\Delta \approx 0$ can be satisfied. One can see that the EIT(1) appears in the spectrum. Curve 2' is the frequency reference on which the EIT-resonance and the VSOR are present. These spectral features are shifted relative to one another due to nonzero detuning $|\Delta|$ of radiation frequency ν_C from the initial value of the $2 - 2'$ transition frequency. It follows from the curves presented in Fig. 2.5 that the decrease in detuning $|\Delta|$ for the EIT(1) automatically leads to an increase in the frequency detuning for the EIT(3) and EIT(6). Therefore, the parameters for the EIT(3) and EIT(6) in curve 2 are worse than in curve 1 .

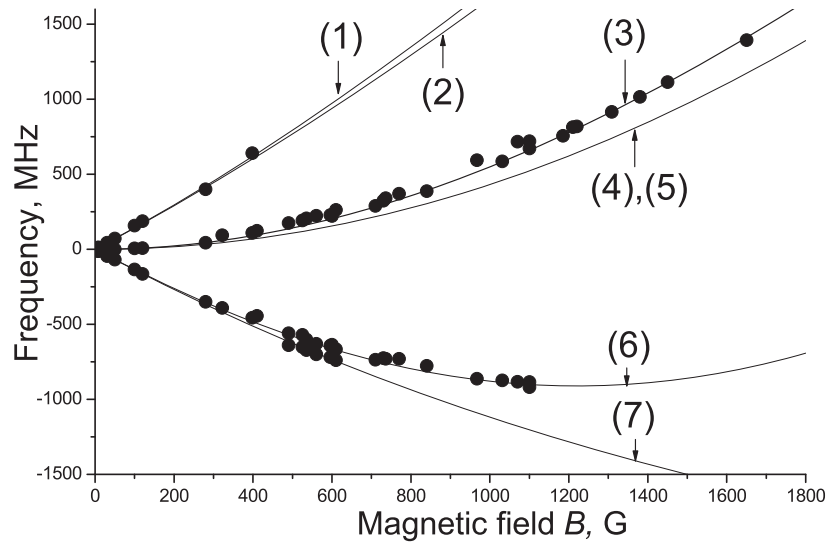


Figure 2.8: Dependence of the frequency shifts of EIT(1)-(7) on the magnetic field. The frequencies of EIT (4) and EIT (5) coincide; therefore, six EIT-resonances with different frequencies can exist. Black circles represent the experimental data.

Figure 2.9 shows three EIT components, when $B = 596$ G longitudinal magnetic field is applied (upper curve). The lower curve shows frequency reference spectrum. It is interesting to note, that in the case of a good adjustment of the coupling and probe beams at the conventional ETC (Fig. 2.1a), an EIT-resonance appears in the reference spectrum, which is narrower than VSOR presented in the frequency reference spectrum when the coupling is not well adjusted.

Since it is necessary to satisfy the condition

$$|\nu_P - \nu_C| = [E(F_g = 2, m_F) - E(F_g = 1, m_F)]/h, \quad (2.1)$$

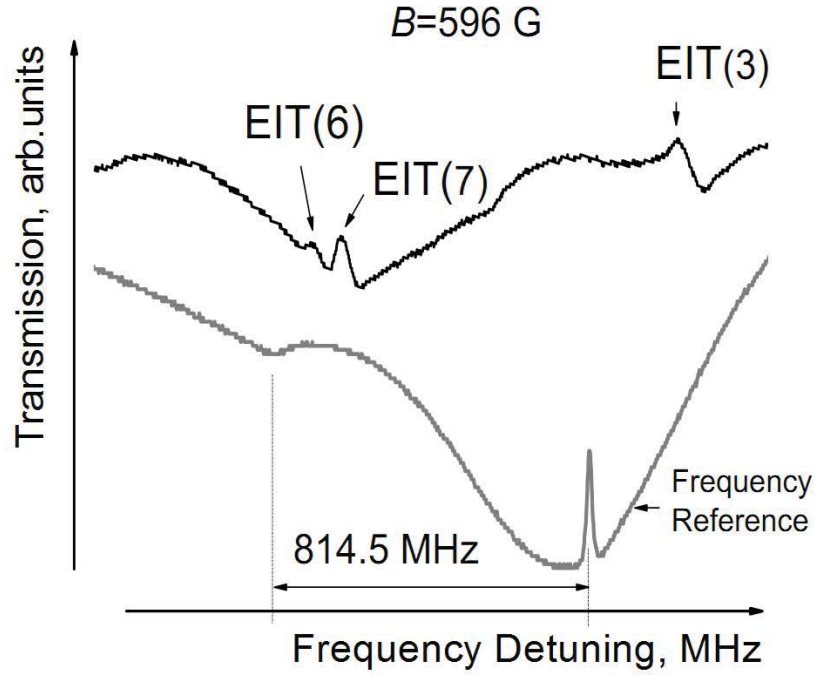


Figure 2.9: Splitting of EIT-resonance into three components. The labels denote corresponding transitions shown in Figures 2.4, 2.8. The lower grey curve shows frequency reference spectrum.

in order for an EIT-resonance to be formed, the number of EIT-resonance components formed in a constant magnetic field and their frequency behaviors depend on the number and shift of magnetic sublevels m_F of the low-lying levels $F_g = 1$ and 2. In the case of the D_1 transitions of ^{87}Rb , the nonlinear energy shift of magnetic sublevels m_F (levels $F_g = 1$ and 2 are denoted below as $F = 1$ and 2) can be calculated by the Breit-Rabi formula presented, for example, in [115]:

$$E(F = 2, m_F) = h\nu_{hfs}[-1/8 + (1/2)(1 + m_F x + x^2)^{1/2}] \text{ for } m_F \neq -2 \quad (2.2)$$

$$E(F = 2, -2) = h\nu_{hfs}(3/8 - x/2) \text{ for } m_F = -2 \quad (2.3)$$

$$E(F = 1, m_F) = h\nu_{hfs}[-1/8 - (1/2)(1 + m_F x + x^2)^{1/2}] \quad (2.4)$$

where $x = 2\mu_B B / h\nu_{hfs}$, μ_B is the Bohr magneton, and $\nu_{hfs} = 6835$ MHz. Figure 2.8 presents seven curves constructed using equations (2.1)-(2.4) that describe the frequency shift of EIT-

resonances in the magnetic field. Black circles represent the experimental results. The numbers of curves 1 – 7 correspond to the numbers of the EIT-resonance components. One can see in Fig. 2.8 that three EIT-resonances (1), (3), and (6) are formed in fields weaker than 300 G. The EIT-resonance (7) appears with fields in the range of 500-630 G. In fields stronger than 1200 G, only the EIT-resonance (3) is observed in the high-frequency wing of the spectrum of probe radiation. As noted above, this is explained by the behavior of the detuning Δ of fixed frequency ν_C from the corresponding upper level of the Λ -system. In particular, for the EIT(1), Δ already rapidly increases in fields stronger than 350 G, which leads to absence of the EIT(1); at $B > 1200$ G for the EIT(6), Δ rapidly increases and, consequently, this EIT-resonance is absent; for the EIT(3), Δ begins to grow rapidly in fields stronger than 1700 G, with this resonance consequently being detected up to such fields.

Along with detuning Δ , the Rabi frequencies of the coupling Ω_C and probe Ω_P laser beams can affect the EIT-resonance parameters. The Rabi frequency linearly contains the matrix element of the dipole moment of an atomic transition [1, 78]. It is known that the atomic transition probability significantly changes in strong magnetic fields [116, 118]. Therefore, it is important to know the behavior of the atomic transition probabilities for the probe and coupling radiation beams. For the probe radiation, the transitions $(1, m_F = +1 \rightarrow 2', m_F = +2)$, $(1, m_F = 0 \rightarrow 2', m_F = +1)$, and $(1, m_F = -1 \rightarrow 2', m_F = -2)$ of the D_1 -line of ^{87}Rb are involved in the formation of EIT-resonances (1), (3), and (6), respectively. It was shown in [120] that the probabilities of the first two transitions increase monotonically up to 5000 G, while, for component (6), the probability decreases by a factor of 2 at $B = 1500$ G (as compared to that at $B = 0$). As for the atomic transition probabilities for coupling radiation indicated in Fig. 2.5 for EIT(1), EIT(3), and EIT(6), calculations by the model presented in [118, 124] show the following: for EIT(1), the probability rapidly drops; for EIT(3), the probability decreases slowly and drops by a factor of 3 at 3000 G; and, for EIT(6), the probability increases and at 3000 G becomes a factor of 3 larger than the probability at $B = 0$. However, from the practical point of view, the application of EIT(3) is more expedient because its frequency shift increases monotonically (Fig. 2.8) and amounts to ~ 4 GHz at 3000 G. Consequently, with an appropriate choice of the coupling laser frequency, the EIT(3) can be used to form a narrow resonance at a frequency strongly shifted with respect to the

resonance transition of ^{87}Rb . In addition, using the frequency shift of EIT(3), it is possible to measure both uniform and strongly nonuniform magnetic fields up to several thousand gauss. In order to measure relatively weak fields ~ 5 G (in this case, the frequency interval between two neighboring EIT-resonances is ~ 7 MHz), the powers of the coupling and probe lasers were decreased to 0.1 and ~ 0.04 mW, respectively, which allowed us to narrow the EIT-resonance width down to 6.5 MHz (the EIT-resonance contrast becomes significantly lower, but it is still sufficient for recording) and to resolve spectrally EIT(1), EIT(3), and EIT(6). It is important to note that the splitting of a EIT-resonance on the Λ -system of the D_2 -line of ^{87}Rb (both lower levels are the same as in the case shown in Fig. 2.1b) was studied in [111] using a similar setup (i.e., two independent diode lasers) and an ordinary Rb cell with $L = 5$ cm in the magnetic field $B = 3.2$ G. Therefore, three EIT-resonances were also detected with a spectral width of about 1.5 MHz. Consequently, the decrease in thickness L by a factor of $\sim 6 \times 10^4$ when using an ETC (the local spatial resolution is improved by the same factor in the case of a magnetic field with a large gradient) deteriorates the spectral resolution only by a factor of ~ 4 . Note that the behavior of the EIT-resonance for the D_1 -line of ^{87}Rb (Fig. 2.8) in weak fields is similar to that observed for the D_1 -line of Na [115] because the systems of levels are analogous.

2.3 The EIT-resonance splitting in a magnetic field in case of microcell: magnetic field $B < 2000$ G

For these researches a micrometer size cell was used. An important advantage of using a thin atomic vapor column with $L = 30 \mu\text{m}$ is the possibility of implementing strong permanent magnets that can produce B fields up to thousands of Gauss over a distance of a few centimeters. The field of such permanent magnets is strongly inhomogeneous. Its gradient can be as high as 100-200 G/mm. This excludes the use of centimeter-long cells. At the same time, owing to a small diameter of the vapor column, the variation of B is several orders of magnitude lower than the absolute value of the field. In addition, a buffer gas (neon) with a pressure of ~ 100 Torr is added into the cell for the following reason. As was previously shown [11, 125], an important condition for the formation of the EIT-resonance in

the Λ -system with the use of cells with a micron thickness is the smallness of the frequency detuning Δ between the coupling laser and the respective atomic transition. High magnetic fields automatically result in high Δ . In this case, EIT occurs for the atoms moving in the direction of the laser radiation z at the velocity $V_z = 2\pi\Delta/k$, where $k = 2\pi/\lambda$. This leads to a decrease in the time of flight $\tau = L/V_z$ (where L is the distance between the cell windows) and, consequently, to a fast increase in the phase decoherence rate ($\Gamma_{12} = 1/2\pi\tau$) between the two lower levels of the Λ -system (a wall collision with a large probability results in the transition of the atom between the lower levels [11]). An increase in Γ_{12} leads to a fast decrease in the amplitude and an increase in the width of the EIT-resonance. The presence of a buffer gas (~ 100 Torr) greatly reduces the mean free path of the alkali atoms (down to $\sim 1 \mu\text{m}$). As a result, they do not reach the walls of the $30\text{-}\mu\text{m}$ cell [125].

In this section, we report on the experimental investigation of the behavior of the EIT-resonance in strong magnetic fields up to 1.7 kG with the use of the $30\text{-}\mu\text{m}$ cell filled with an atomic rubidium vapor and a buffer gas (neon). We show that the EIT-resonance in the Λ -system of the D_1 -line of ^{85}Rb atoms splits in a longitudinal magnetic field into five components, whose frequency behavior depends on the frequency configuration of the probe and coupling fields and the magnitude of the magnetic field. We also show that the study of the characteristics of the EIT-resonance components in high magnetic fields can readily reveal the onset of the Paschen-Back regime for the hyperfine structure of the atoms, i.e., the regime of decoupling the total angular electronic momentum J and the nuclear magnetic momentum I .

The scheme of the experimental setup is similar to the setup presented in Fig. 2.1a. The only difference is the cell. For this experiment we use the cell, which design is similar to that described in [126, 127]. The 20×30 mm rectangular windows with a thickness of 2 mm were fabricated of crystalline garnet that does not feature birefringence. To form a wedge-shaped gap, 50- and $20\text{-}\mu\text{m}$ platinum bars were placed in the lower and upper parts, respectively (between the windows). This provided gradual variation of the gap thickness in the vertical direction (between the well-polished surfaces of the microcell windows) in the range of 20-50 μm (in the experiment, we used a thickness of $30 \mu\text{m}$).

The permanent magnets were mounted onto two nonmagnetic stages with the possibility of

gradually adjusting the distance between them. The magnetic field in the microcell increased when the permanent magnets approached each other (the technique of the measurement of the inhomogeneous magnetic field is described elsewhere [118]).

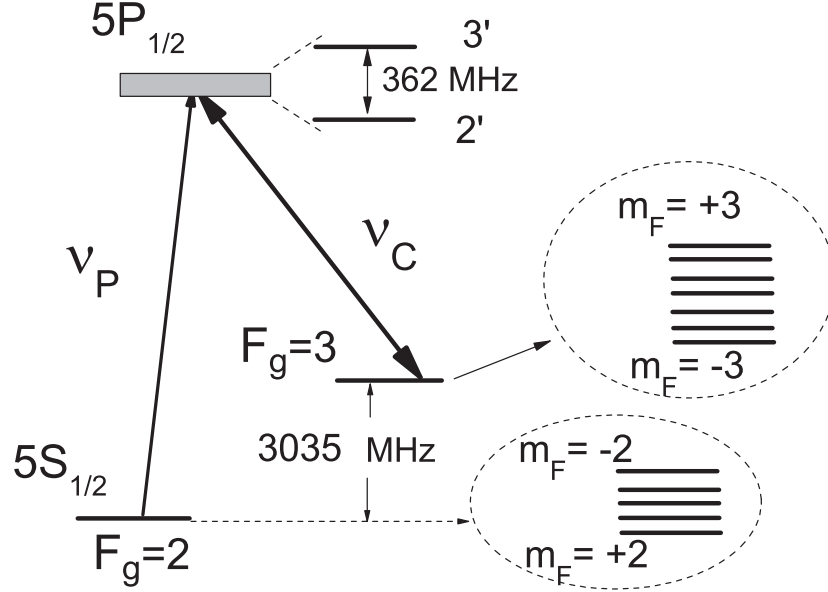


Figure 2.10: Levels of the D_1 -line of ^{85}Rb atoms participating in the formation of EIT-resonance. In the presence of the magnetic field, the EIT-resonance components are formed by different m_F sublevels.

We studied the Λ -system of the D_1 -line of ^{85}Rb atoms shown in Fig. 2.10. Here, the frequency ν_C is in resonance with the transition $F_g = 3 \rightarrow F_e = 2'$ (primed numbers stand for upper levels), whereas the frequency ν_P is swept through the resonance $F_g = 2 \rightarrow 5P_{1/2}$. In the presence of the external longitudinal magnetic field $\mathbf{B} \parallel \mathbf{k}$ (where \mathbf{k} is the wave vector of the laser field), the Λ -systems of different m_F sublevels are formed (see Figs. 2.10, 2.13). The power of the coupling ($P_C = 130$ mW) and probe ($P_P < 1$ mW) lasers were chosen so that the spectral width of the EIT components would be small at a good contrast. The transmission spectra of the probe beam in the magnetic field increasing from zero to 1480 G are shown in Fig. 2.11.

The EIT-resonance components in Fig. 2.11 are marked by numbers 1–5 (this numbering corresponds to that of the curves shown in Fig. 2.14). The amplitudes of the EIT-resonance components decrease gradually with an increase in the magnetic field; however, the amplitudes in Fig. 2.11 were modified so that all peaks would be visible. Despite the fact that the amplitudes of the EIT-resonance components decrease with an increase in the magnetic

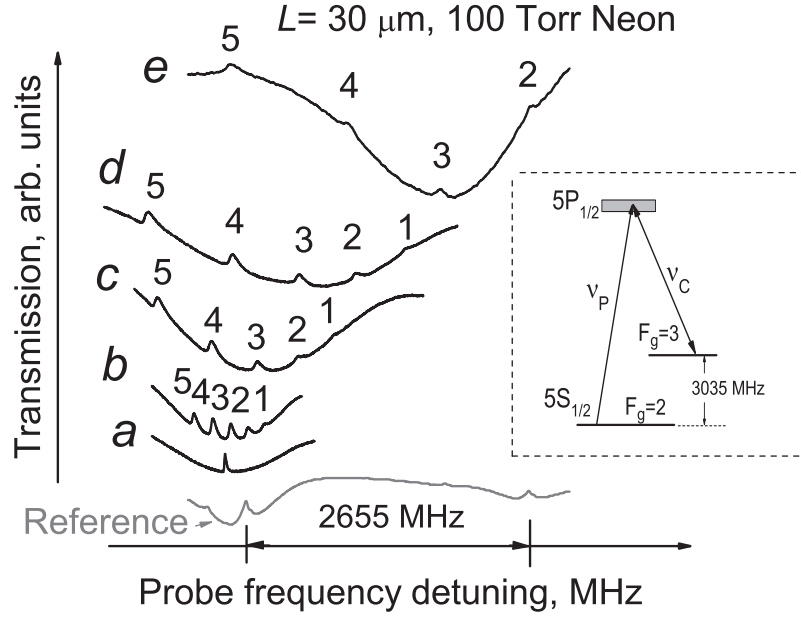


Figure 2.11: Transmission spectra of the probe beam at $B = 0, 180, 480, 760,$ and 1480 G (the spectra are vertically shifted for convenience). The numbering of the EIT-resonance components corresponds to that given in Fig. 2.14. The microcell with $L = 30 \mu\text{m}$ filled with rubidium and neon is used. The temperature is $\sim 100^\circ\text{C}$. The configuration of ν_C and ν_P is shown in the inset (the frequency ν_P is swept through the resonance $F_g = 2 \rightarrow 5P_{1/2}$). The lower gray curve is the reference spectrum obtained with the use of the Rb nanocell.

field, the components are reliably resolved up to 1.7 kG without any special technical tricks. A decrease in the amplitudes of the EIT-resonance components is due to two reasons: an increase in the magnetic field leads to an increase in the detuning Δ of the frequency ν_C from the respective atomic transition and (more importantly) to a decrease in the probability of the atomic transitions at the frequencies ν_C and ν_P [99, 118, 141].

Figure 2.12 presents similar spectra for another configuration of frequencies ν_C and ν_P shown in the inset. Here, the magnetic field ranges from zero to 1630 G. The EIT-resonance components are marked with the numbers $1'-5'$ corresponding to the numbering in Fig. 2.15.

The theoretical dependence of the hyperfine levels $F_g = 2, 3$ of ^{85}Rb atoms on the magnetic field is shown in Fig. 2.13 (the curves were calculated according to the known model described, e.g., in [117, 141]). It should be mentioned that ^{85}Rb atoms exhibit decoupling of J and I in the fields $B \gg A_{HFS}/\mu_B \approx 700$ G, where A_{HFS} is the hyperfine constant for $5S_{1/2}$ and μ_B is the Bohr magneton, the level splitting is described by the projections m_J and m_I , and the hyperfine Paschen-Back regime [117, 128, 140] takes place. The EIT-resonance occurs under

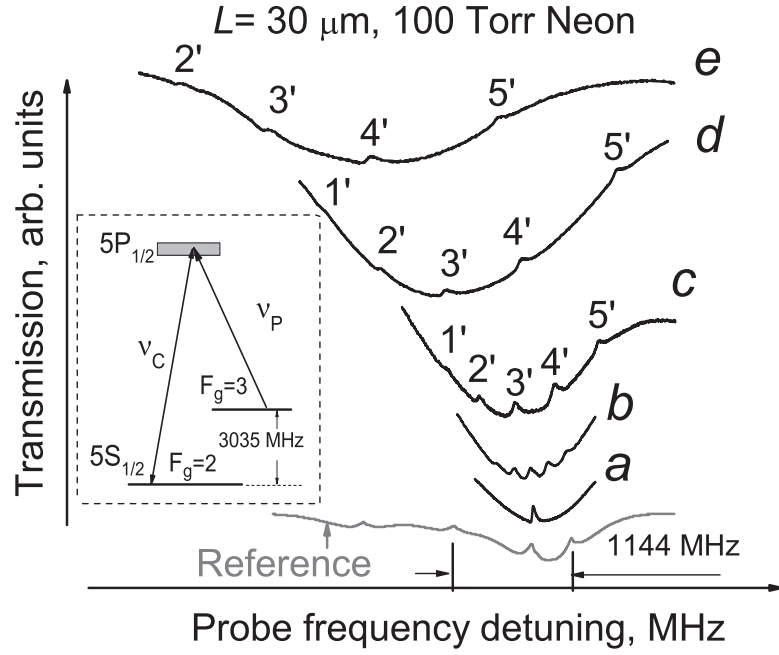


Figure 2.12: Transmission spectra of the probe beam at $B = 0, 175, 380, 850,$ and 1630 G. Numbering of the EIT-resonance components corresponds to that of the curves in Fig. 2.15. The configuration of ν_C and ν_P is shown in the inset (the frequency ν_P is swept through the resonance $F_g = 3 \rightarrow 5P_{1/2}$). The lower grey curve is the reference spectrum.

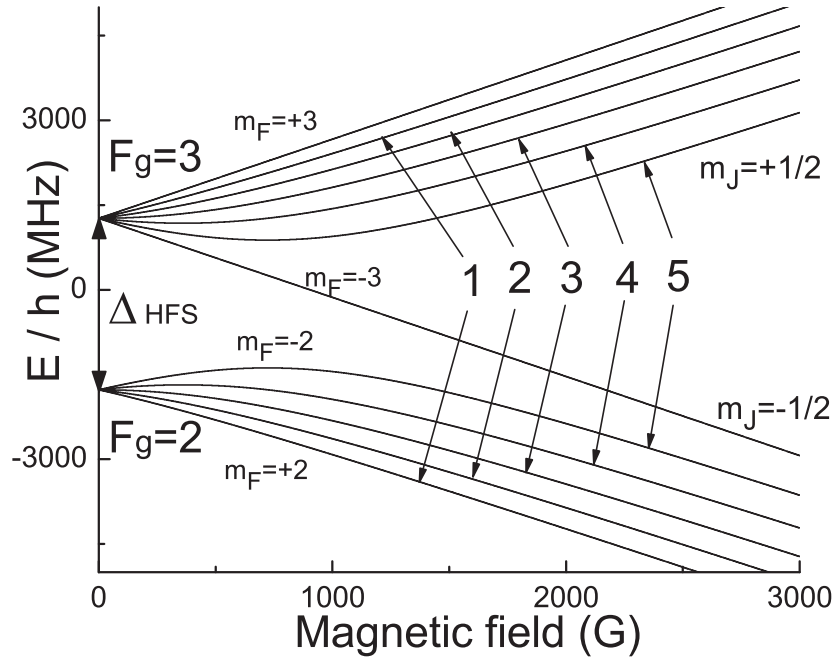


Figure 2.13: Theoretical magnetic field dependence of the hyperfine structure of ^{85}Rb atoms with $F_g = 2, 3$. Digits indicate the m_F sublevels participating in the formation of the EIT-resonance components 1 – 5.

the condition $\nu_P - \nu_C = [E(F = 3, m_F) - E(F = 2, m_F)]/h$.

Figures 2.14 and 2.15 show the theoretical curves for the EIT-resonance components 1 – 5

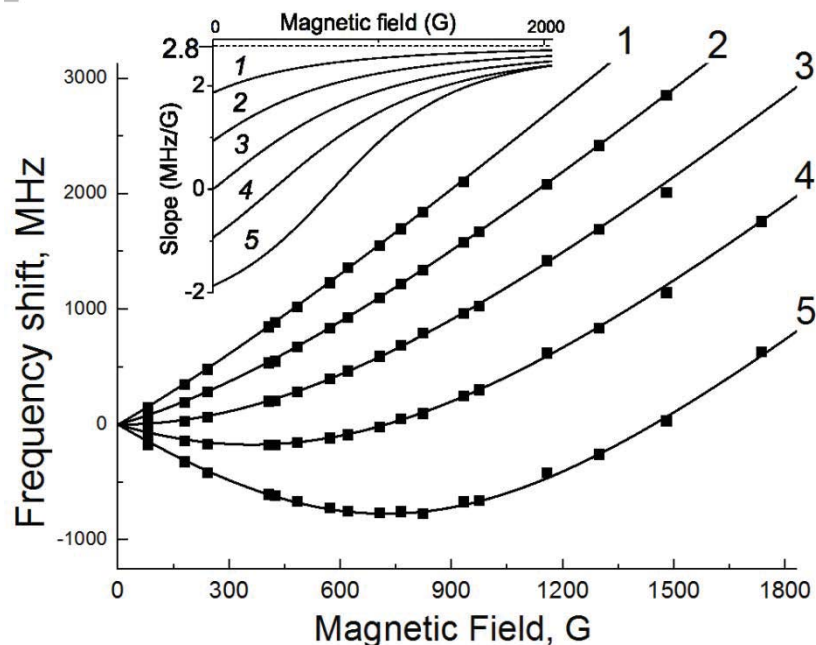


Figure 2.14: Magnetic field dependence of the frequency shifts of the EIT-resonance components 1 – 5 (the configuration of the frequencies ν_C and ν_P is shown in the inset in Fig. 2.11). Solid lines are the theoretical curves. Closed squares are the experimental points (the size of the symbols represents an experimental error of $\sim 2\%$). The slopes of all curves at $B > 1$ kG are positive and asymptotically approach $s = 2.8$ MHz/G (see inset), which is the manifestation of the hyperfine PaschenBack regime.

and $1' - 5'$ with the frequency configurations shown respectively in the insets in Figs. 2.11 and 2.12, respectively. The experimental results are shown by closed squares. As is seen in Figs. 2.14 and 2.15, the experimental results are in good agreement with the theory. According to the experiment, five Λ -systems with the following hyperfine sublevels participate in the formation of the EIT-resonance components 1 – 5 ($1' - 5'$) ($F_g = 3, m_F; F_g = 2, m_F$) (see Fig. 2.13): $(3, +2; 2, +2)$, $(3, +1; 2, +1)$, $(3, 0; 2, 0)$, $(3, -1; 2, -1)$, and $(3, -2; 2, -2)$. No additional EIT-resonance components with different combinations of the lower sublevels were detected.

As is seen in Fig. 2.14 (the frequency ν_P is swept through the resonance $F_g = 2 \rightarrow 5P_{1/2}$), the frequency slope of all curves becomes positive at $B > 1$ kG and asymptotically approaches $s = 2.8$ MHz/G (see inset in Fig. 2.14). In the case shown in Fig. 2.15, the frequency slope of all curves becomes negative at $B > 1$ kG and asymptotically approaches $s' = -2.8$ MHz/G (see inset in Fig. 2.15). Such behavior in both cases is due to the onset of the hyperfine Paschen-Back regime, since the quantities s and s' at $B \gg 700$ G are determined by m_J, m_I , and g_J (g_J is the Landé factor of the fine structure of the level $5S_{1/2}$). According to Fig. 2.13,

we have $s = (2\mu_B g_J |m_J|)/B \approx 2.8 \text{ MHz/G}$ and $s' = -(2\mu_B g_J |m_J|)/B \approx -2.8 \text{ MHz/G}$ ($g_J \approx 2.002$; the term $g_I m_I$ is omitted because g_I is four orders of magnitude smaller). Since the frequency slopes of the EIT-resonance components 1–5 ($1'–5'$) asymptotically approach s (s'), the frequency intervals between the EIT-resonance components 1–5 ($1'–5'$) in the hyperfine Paschen-Back regime also asymptotically approach fixed values. The slope of the EIT-resonance component 1 is $> 2 \text{ MHz/G}$. This can be used for measuring high-gradient fields. For example, a $30\text{-}\mu\text{m}$ displacement of the cell at a gradient of 200 G/mm would result in an additional frequency shift of more than 10 MHz , which is easily detectable.

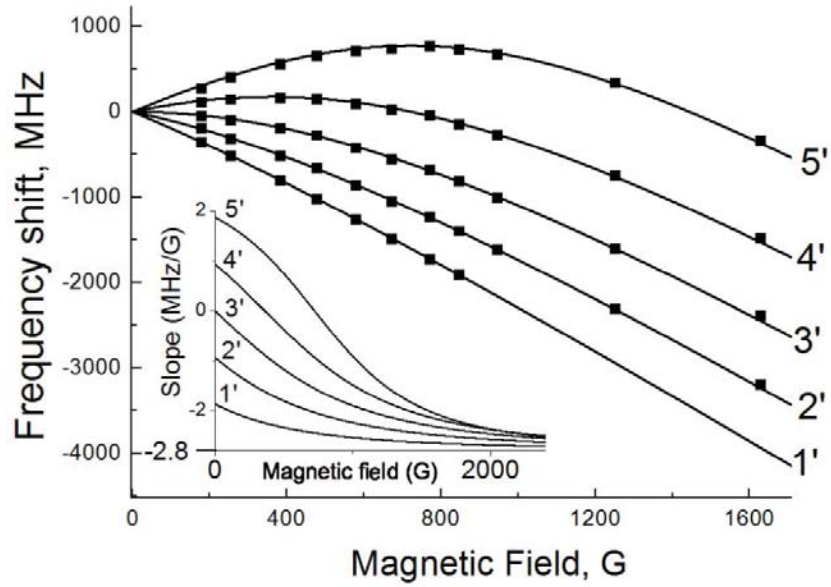


Figure 2.15: Magnetic field dependence of the frequency shifts of the EIT-resonance components 1'- 5' (the configuration of the frequencies ν_C and ν_P is shown in the inset in Fig. 2.12). Solid lines are the theoretical curves. Closed squares are the experimental points (the size of the symbols represents an experimental error of $\sim 2\%$). The slopes of all curves at $B > 1 \text{ kG}$ are negative and asymptotically approach $s' = -2.8 \text{ MHz/G}$ (see inset), which is the manifestation of the hyperfine Paschen-Back regime.

The higher B field is (compared to 700 G) the purer hyperfine Paschen-Back we have. However, the regime can be regarded as quite perfect already at $B \sim 5 \text{ kG}$, as was established in our previous work with the use of a Rb nanocell [140]. At the same time, nanocells still remain hardly available for many researchers. Implementation of microcells (which can even be made of glass) is also capable of extending the margins of the phenomena under investigation. In particular, the technique of studying the hyperfine Paschen-Back regime with the use of electromagnetically induced transparency is well applicable to other alkali atoms and

their isotopes. In this respect, ^{39}K atoms are unique since their hyperfine constant A_{HFS} is much lower than that of ^{85}Rb and therefore the hyperfine Paschen-Back regime starts to manifest itself already at $B = 200$ G.

In this chapter the EIT-resonance splitting in magnetic field for the case of D_1 -line of 87 and 85 isotopes of rubidium in nanocell and microcell is studied in details. We calculated the dependence of the frequency shifts of EIT components on the magnetic field. The comparison of experimental and theoretical results are made and the good agreement is shown.

In next chapter the N -type resonance observation in microcell filled with rubidium and buffer gas is presented. The dependence of N -resonance parameters (the FWHM and the contrast) on the angle between two lasers (which are used to form the resonance) is shown.

Chapter 3

N-resonance formation in micron thickness cells, filled with the Rb atom vapors and neon buffer gas

Introduction

Mediated by the effects of CPT and EIT [29,30], nonlinear optical interactions can be significantly enhanced in comparison with two-level resonant systems. This was first recognized for Λ -type three-level configuration and subsequently developed for a variety of multi-level systems. In particular, a four-level N -type configuration displaying large nonlinearity attracts a lot of attention because of its broad range of applications in quantum and nonlinear optics [68]. This system demonstrates either an efficient self-action at a single-photon energy level [129] or strong interaction of two electromagnetic fields via refractive [130–132] and/or absorptive [132] nonlinearities. Several experimental studies of spectral properties of real N -type configurations have been performed quite recently [45].

Doppler-free absorption resonances that can be observed in an N -type level configuration represent another important feature of the system. Such resonances remove the strict restrictions on the Doppler-free geometry imposed by conventional nonlinear spectroscopy [134].

The coherence results an extension of the possible applications of hot atomic vapors by eliminating Doppler broadening without cooling. For example, this effect might be employed to enhance gain of gas lasers (with or without population inversion), or to obtain a high

index of refraction without absorption. The narrow subnatural width of the resonances could be very useful in quantum computing. The three-photon transparency resonance inherits the properties of the regular EIT-resonance but has one significant advantage in comparison with usual EIT: it has almost no Doppler background. This unique feature is important for different applications such as atomic clocks and magnetometry.

3.1 Literature overview of N -type resonance

The N -type resonance have been firstly demonstrated in hot ^{87}Rb atomic vapor driven by two coherent electromagnetic fields [2]. The experimental observation of a new kind of strong and narrow Doppler-free absorption (up to $\sim 95\%$) and transmission resonances in hot rubidium vapor has been reported. They studied propagation of two electromagnetic fields through isotopically pure ^{85}Rb atomic vapor. One (drive) field is red-shifted from either D_1 or D_2 -lines of ^{85}Rb , while the other (probe) field is nearly resonant with one of the atomic transitions.

In Ref. [135] the first-order light shifts can be canceled for an all-optical, N -type resonance on the D_1 transition of ^{87}Rb . This light-shift cancelation facilitates improved frequency stability for an N -resonance clock. For example, by using a tabletop apparatus designed for N -resonance spectroscopy, it is possible to measure a short-term fractional frequency stability (Allan deviation) of $\simeq 1.5 \times 10^{-11} \tau^{-1/2}$ for observation times of $1 \text{ sec} \leq \tau \leq 50 \text{ sec}$. The narrow transparency window is observed on the background of high-contrast Doppler-free subnatural absorption resonance.

Experimental comparison of three-photon-absorption resonances (N -resonances) for the D_1 and D_2 optical transitions of thermal ^{87}Rb vapor has been observed in [136]. They have shown that the D_2 N -resonance has a better contrast but a broader linewidth than the D_1 N -resonance, such that the N -resonance quality factor is comparable for the D_1 and D_2 transitions. This result implies a similar shot-noise limit to N -resonance frequency standard performance on the D_1 and D_2 transitions, in strong contrast with CPT resonances, for which the quality factor is about an order of magnitude worse for the D_2 transition than for D_1 . In addition, the symmetry features of N -type resonances have been discussed in [136, 137] and it is shown that D_2 N -resonance line shape is significantly more symmetric than the D_1 -line

shape, indicating that a D_2 N -resonance frequency standard will have reduced sensitivity to certain modulation-induced systematic frequency shifts. Taken all together, these factors imply superior performance for frequency standards operating on alkali D_2 N -resonances, in contrast with coherent population trapping resonances, for which the D_2 transition provides poorer frequency standard performance than the D_1 transition.

The parameters of N -resonances can be improved by using laser radiation from three sources [138]. For applications in spectroscopy, metrology etc., it is important to reduce the dimensions of the atomic vapor cell in which optical resonances are formed while maintaining good resonance parameters [125, 127, 139, 140].

3.2 Experimental technique

For the observation of N -type resonance we have used the experimental technique (the setup is depicted in Fig. 3.1) described below. We use MTC for N -type resonance formation that has the same design as the MTC described in the Section 1.2.1. The N -resonance was formed in a Λ -system by two lasers beams with $\lambda \approx 795$ nm and 1 MHz linewidth: the probe beam, whose frequency was tunable, and the coupling beam, whose frequency was fixed. The diagram presented in Fig. 3.2 shows the Λ -system for the ^{85}Rb atom, where $F_g = 2, 3$ are the ground levels, and the combined upper level $5P_{1/2}$ consists of hyperfine levels $F_e = 2, 3$. The probe laser frequency ν_P was resonant with the $F_g = 2 \rightarrow 5P_{1/2}$ transition, and the coupling laser frequency was shifted by the value of the ground state hyperfine splitting (Δ_{HFS}): $\nu_{C1} = \nu_P + \Delta_{HFS}$.

The beams of two single-frequency extended cavity diode lasers (ECDL) were carefully superimposed and directed by PBS3 onto the MTC. The coupling and probe beams were linearly polarized in orthogonal planes. The small thickness of MTC makes it possible to use a permanent ring magnet (PRM) in order to apply a strong magnetic field and still obtain a homogeneous field over the thickness of the cell: in the MTC, the variation of the B -field inside the atomic vapor column is negligible compared to the value of the applied magnetic field. The magnetic field was measured by a calibrated Hall gauge. To control the magnetic field value, one of the magnets was mounted on a micrometric translation stage that allowed

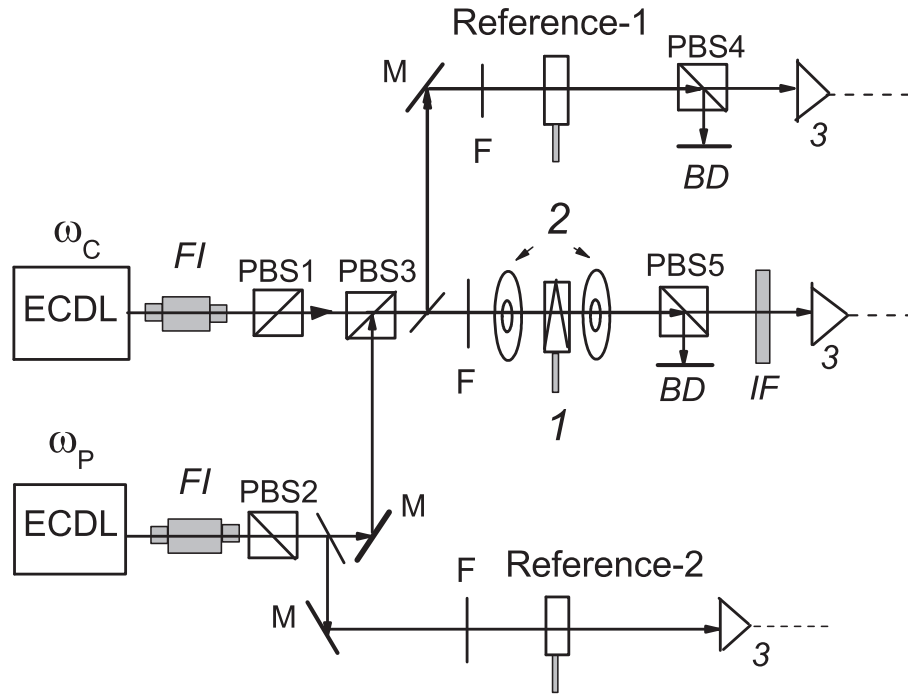


Figure 3.1: Sketch of the experimental setup. ECDL - diode lasers; FI - Faraday isolator; 1- MTC in the oven; PBS- polarizing beam splitters; 2- permanent ring magnets; 3- photodetectors; IF - interference filter with 10 nm transmission bandwidth at 795 nm; F - neutral density filters; BD- beam dump to block ν_c . PBS5 is used to single out ν_p for detection.

longitudinal displacement. Portions of the coupling and probe beams were diverted to an auxiliary 40 μm -long Rb cell filled with Ne gas to obtain an N -resonance spectrum at $B = 0$.

This spectrum served as frequency Reference-1. Furthermore, another portion of the probe beam was diverted to a Rb nanocell with $L = \lambda$ to obtain a $B = 0$ transmission spectrum, which served as frequency Reference-2 [141]. The optical radiation signals recorded by photodiodes (3) were amplified and recorded by a four-channel digital storage oscilloscope.

Although the best N -resonance contrast and linewidth can be achieved for cells with thicknesses around 1 cm [2,135–138], using an MTC with a thickness as small as 30 to 40 μm still allowed us to obtain good resonance parameters. The MTC side arm, whose temperature determines the density of Rb atoms, was maintained at $\sim 110^\circ\text{C}$ (Rb atomic vapor density 10^{13} cm^{-3}).

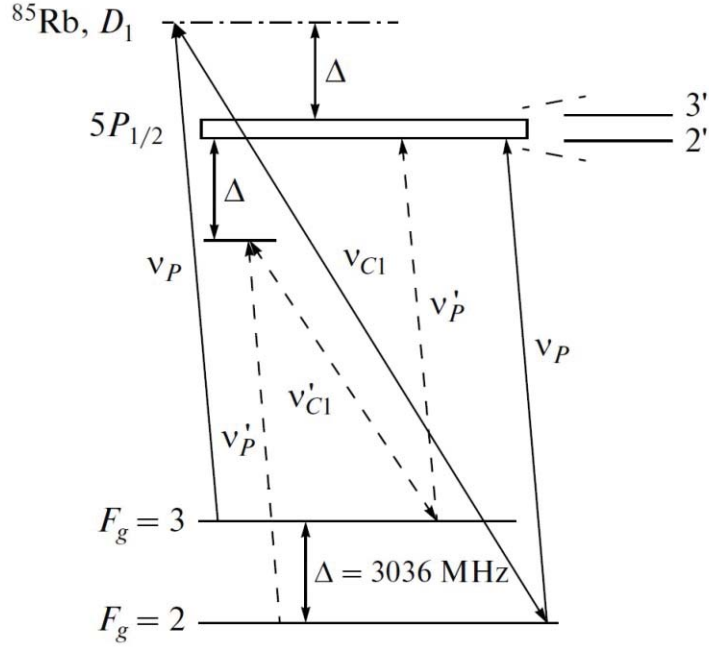


Figure 3.2: Λ system of D_1 -line ^{85}Rb atoms. Probe laser frequency ν_P scans the transitions $F_g = 2 \rightarrow F_e = 2, 3$ and a N -type resonance forms in the probe radiation spectrum. If scans the transitions $F_g = 3 \rightarrow F_e = 2, 3$ (dashed lines), N -type resonance formation requires a lower coupling laser frequency $\nu'_{C1} = \nu_{C1} - 3\Delta$.

3.3 Formation of N -type resonance in the vapor of atoms Rb, D_1 -line, in the presence of neon buffer gas

The atomic configuration of N -type resonance in a Λ system of ^{85}Rb atoms (D_1 -line) formation is presented in Fig. 3.2. The lower levels of the Λ system are $F_g = 2, 3$ and the upper level is $5P_{1/2}$ (which consists of two Doppler broadened hyperfine levels $F_e = 2, 3$). Probe laser frequency ν_P scans the transitions $F_g = 2 \rightarrow F_e = 2, 3$ and coupling laser frequency ν_{C1} is fixed. In the probe radiation spectrum, a cascade N -type resonance forms if the frequency difference is $\nu_{C1} - \nu_P = \Delta$, where Δ is the hyperfine splitting of the lower level (it is important that frequency ν_{C1} is tuned out by Δ from the transition $F_g = 2 \rightarrow 5P_{1/2}$). It is seen that, if a lower probe laser frequency (Fig. 3.2, dashed lines), which scans the $F_g = 3 \rightarrow 5P_{1/2}$ transitions, is used and "laid off" from level $F_g = 2$, the formation of the N -type resonance requires a lower coupling laser frequency, $\nu'_{C1} = \nu_{C1} - 3\Delta$. It is important that the contrast and spectral width of the N -type resonance are almost the same in both cases. For comparison, Fig. 3.3 shows a schematic diagram for the formation of the EIT-resonance in the same Λ system of ^{85}Rb atoms (D_1 -line). Here, the same probe laser frequency ν_P is used and

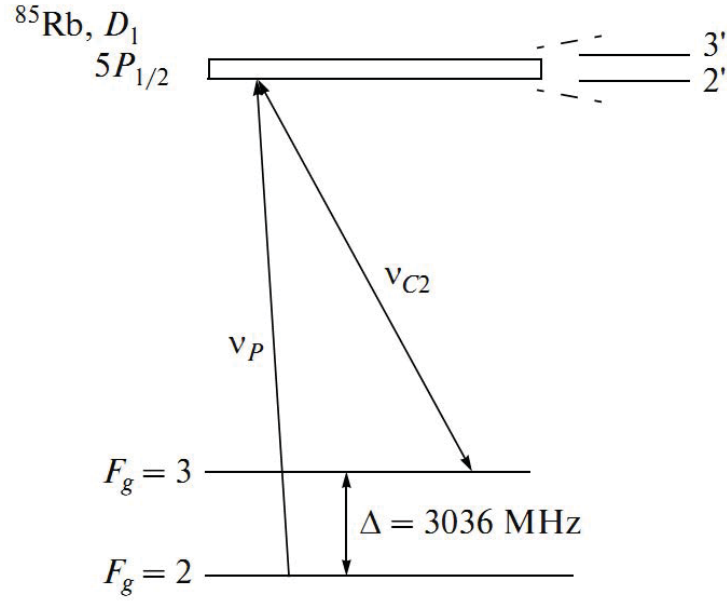


Figure 3.3: Λ system of D_1 -line ^{85}Rb atoms at the same probe laser frequency ν_P but another coupling laser frequency, $\nu_{C2} = \nu_{C1} - 2\Delta$. The formed dark resonance demonstrates a decrease in the absorption.

the coupling laser frequency ν_{C2} should be lower by 2Δ in this case. Thus, as the coupling laser frequency increases ($\nu_{C1} = \nu_{C2} + 2\Delta$), the "dark" resonance (exhibiting a decrease in absorption) that forms in the probe radiation spectrum of the Λ system becomes a bright N -type resonance (exhibiting an increase in absorption).

We have studied the dependence of the process on rubidium vapor column thickness L and showed that the N -resonance has a good contrast and a narrow spectral width even at a small thickness ($L = 50\mu\text{m}$). We have also investigated the splitting of the N -resonance in magnetic fields for ^{85}Rb atoms (D_1 -line). An analysis of the recorded spectra demonstrates that the initial and final levels are represented by the lower levels of the atom, $F_g = 2, 3$. The characteristics of the N and EIT-resonances that form in the same Λ system are compared as functions of vapor column thickness L . The noncollinear geometry of N -type resonance formation was studied, and possible practical applications were noted.

The diagram presented in Fig. 3.4a shows the Λ -system for the Rb atom, where $F_g = 2, 3$ are the ground levels, and the combined upper level $5P_{1/2}$ consists of hyperfine levels $F_e = 2, 3$. The probe laser frequency $\nu - P$ was resonant with the $F_g = 3 \rightarrow 5P_{1/2}$ transition, and the coupling laser frequency was shifted by the value of the ground state hyperfine splitting (Δ_{HFS}): $\nu_C = \nu_{P1} - \Delta_{HFS}$. Transmission spectra of the probe radiation through the MR-cell

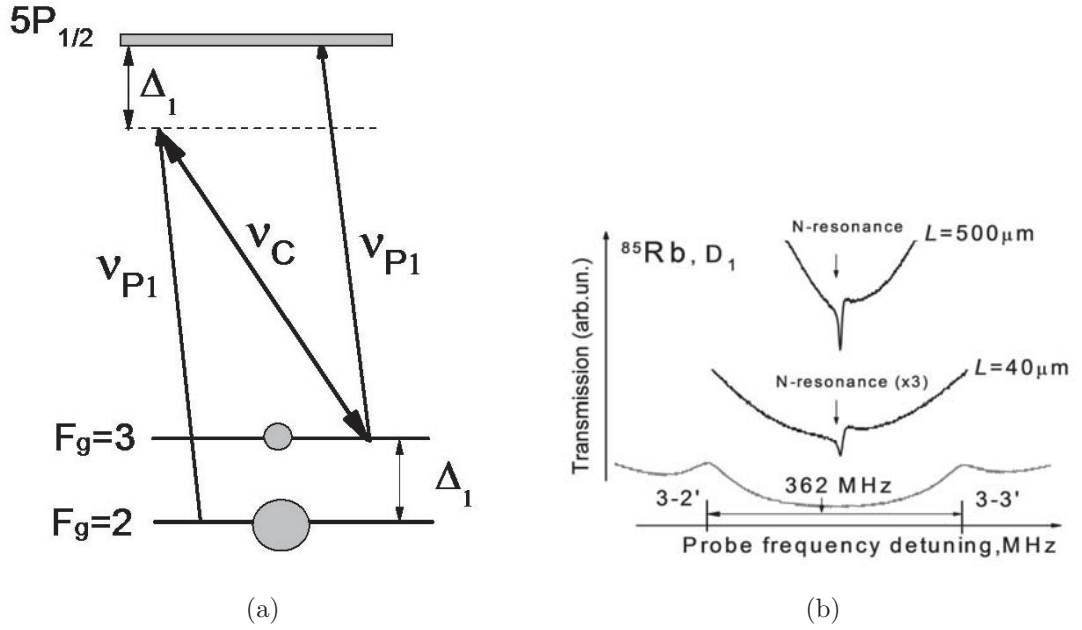


Figure 3.4: a: Relevant energy levels of the ^{85}Rb D_1 -line involved in the N -type resonance formation, $\Delta_1 = \Delta_{HFS} = 3036$ MHz, b: The upper and the middle (is multiplied by 3) curves shows N -type resonance for the thickness $L=500$ and $50 \mu\text{m}$, correspondingly; $P_C = 25$ mW, $P_P=1$ mW, N -type resonance on D_1 has dispersive profile), the lower grey curve is the Reference-2 spectrum.

containing N -type resonance are presented (Fig. 3.4b) for two cases : i) with $L = 0.5$ mm (the upper curve) and the linewidth (full width half maximum) about 4.5 MHz (i.e. the linewidth is the sub-natural, since the natural linewidth is 6 MHz), the contrast is 35 %; ii) $L = 40 \mu\text{m}$ (the middle curve), the linewidth is about 6 MHz and the contrast is ~ 10 %. Spectra were obtained under nearly identical conditions. For convenience, the spectra are shifted in the vertical direction. The lower grey curve presents the spectrum of Reference-2. The physical origin of N -type resonance formation is as follows. The probe radiation causes a strong optical pumping effect, which transfers a large number of Rb atoms from $F_g=3$ to $F_g=2$ (the presence of buffer gas enhances optical pumping process, meanwhile weakly influences on the ground levels broadening), thus assuring the condition $N_2 > N_3$, conventionally shown by a large and small disks (where N_2 and N_3 are the populations of the $F_g=2$ and $F_g=3$ levels, respectively). For the condition $\nu_{P1}-\nu_C = \Delta_{HFS}$, a strong 2-photon-type absorption of the probe radiation via $F_g=2 \rightarrow F_g=3$ occurs at the frequency $\nu_{P1} = \nu_C + \Delta_{HFS}$, forming the N -type resonance. 2-photon absorption is $\sim \exp[-(N_2 - N_3) \times \sigma_{2PA} \times L]$, where the cross-section σ_{2PA} for 2-photon absorption of the probe beam ν_P is given by formula (3.1)

from [142]:

$$\sigma_{2PA} = \frac{\lambda^2}{16\pi^2} \times \frac{\gamma_N}{\gamma_{21}} \times \frac{d \times E_C}{\hbar \times \Delta} \quad (3.1)$$

where E_C is the electric field of the coupling laser radiation (note that the probe laser cross-section depends on intensity of only the coupling laser), d is the matrix element of the atomic transition dipole moment, Δ is the laser frequency detuning from the state $5P_{3/2}$ ($\Delta \sim 3$ GHz), $\gamma_N = 6$ MHz, $\gamma_{21} \sim 0.1$ MHz, $\lambda = 780$ nm, $(d \times E_C) / \hbar = \Omega \approx 60$ MHz.

Figure 3.5 shows the schematic diagram of the experimental setup for the case of ordinary cm-size cell, for observation of N -type resonance contrast dependance of the angle between two laser radiations. We used the radiation of two continuous narrow-band (with a width of about 1 MHz) extended cavity diode lasers (ECDLs), one of which had fixed frequency ν_C (coupling laser) and the other had tuned frequency ν_P (probe laser); both lasers had a wavelength of ~ 795 nm. Both laser beams 2 mm in diameter were carefully superimposed by Glan prism G_1 (the polarizations of the coupling and probe lasers were linear and mutually perpendicular) and then directed to the cell with atomic vapor. Part of the probe radiation was directed to additional NTC 5 of thickness $L = \lambda$, which was used to form a frequency reference according to the technique described above. The laser radiations were detected with FD-24K photodiodes 3. Interference filter 6 with a transmission of 50% at a wavelength of ~ 795 nm with a bandwidth at half-maximum of 10 nm was placed in front of the photodiode detecting the probe radiation. The signals from the photodiodes were amplified with an operational amplifier and were then supplied to a four-channel TDS2014B digital oscilloscope 7. We used a set of Helmholtz coils 2 inside which cell 4 with atomic vapor was placed in order to cancel the laboratory magnetic field and to form a magnetic field in the given direction. With prism G_2 , the coupling laser radiation was cut off and only the probe radiation was detected.

In the experiment, we used cell of thickness $L = 8$ mm filled with rubidium vapor and gaseous neon at a pressure of 6, 20 and 400 Torr (when studying the dependence of the N -type resonance on thickness L , we also used a wedge cell with a column thickness of $50 - 90 \mu\text{m}$ and a neon pressure of 200 Torr). Two beams with frequencies ν_P and ν_C were brought into coincidence and directed to the cell with atomic vapor and neon at a pressure of

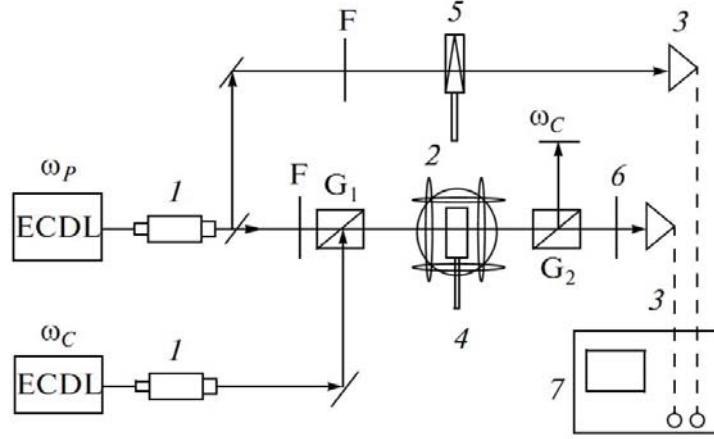


Figure 3.5: Schematic diagram of the experiment: (ECDLs) extended cavity diode lasers, (1) Faraday insulators, ($G_{1,2}$) Glan polarizers, (2) Helmholtz coils, (3) photo-diodes, (4) cell with atomic vapor, (5) auxiliary NTC, (F) neutral optical filters, (6) interference filter of a wavelength of 795 nm, and (7) digital oscilloscope.

6 Torr. The probe laser power was 4 mW and the coupling laser power was 20 mW (the laser beam diameters were about 2 mm). The branch piece (reservoir) temperature was 70°C (the rubidium atom vapor density was approximately 5×10^{11} atoms/cm³). Probe laser frequency ν_P scanned the transitions $F_g = 2 \rightarrow F_e = 2, 3$ and coupling laser frequency ν_C was fixed (Fig. 3.2).

Figure 3.6 (upper curve) shows the N -type resonance formed in the transmission spectrum of the probe radiation. The contrast of the N -type resonance reaches 75% (if it is determined as the ratio of the resonance amplitude to the peak absorption in the absence of the coupling radiation). The estimation of the Rabi frequency with the expression $\Omega/2\pi = \gamma_N(I/8)^{1/2}$ [11], where I is the laser intensity (mW/cm²) and γ_N is the natural width of the upper level (5.8 MHz), yields 40 and 18 MHz for the coupling and probe lasers, respectively. The spectral width (full width at half-maximum) of the N -type resonance is approximately 10 MHz. When the coupling or probe laser power decreases, the N -type resonance contrast decreases to several percent and the spectral width narrows significantly (to 2 MHz). The lower curve in Fig. 3.6 shows the transmission spectrum of the frequency reference at NTC thickness $L = \lambda$. This spectrum contains sub-Doppler optical resonances, which are selective in atomic velocities and are located exactly at atomic transitions [87]. Note that the parameters of the N -type resonance at a pressure of 20 Torr (contrast, spectral width) are approximately the same as those at a pressure of 6 Torr. However, the contrast decreases to 10% at a gaseous

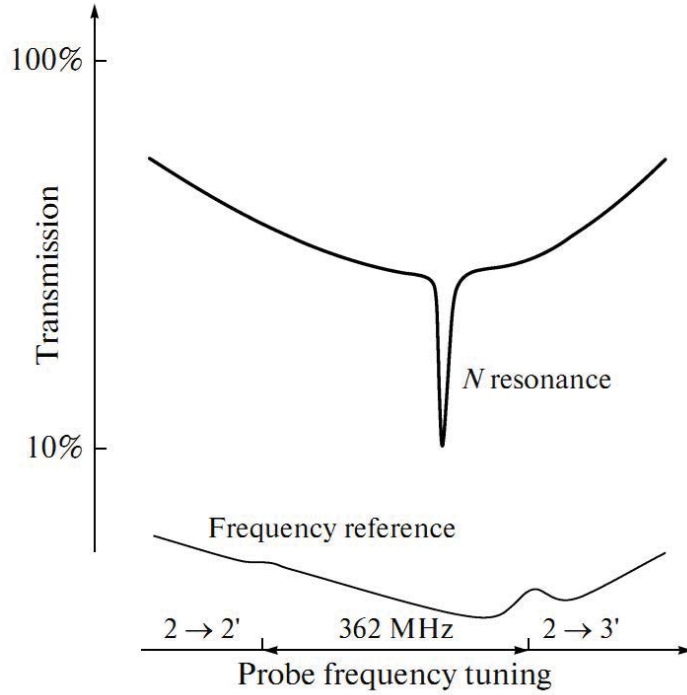


Figure 3.6: (upper curve) Transmission spectrum of the probe radiation with an N -resonance. The cell thickness is $L = 8$ mm, the neon pressure is 6 Torr, and the reservoir temperature is 70 °C. (lower curve) Transmission spectrum of the frequency reference at NTC thickness $L = \lambda$; it contains sub-Doppler resonances at atomic transitions.

neon pressure of 400 Torr (investigation of the dependence of the N -type resonance shape on buffer gas pressure is of interest). When studying the N -type resonance contrast as a function of thickness L , we found that the N -type resonance contrast (amplitude) decreases with decreasing L from 8 mm to $50 \mu\text{m}$. We analyzed a cell with a wedge vapor column thickness of $50 - 90 \mu\text{m}$ at a neon pressure of 200 Torr (cell reservoir temperature of about 100°C). The minimum vapor column thickness at which the N -type resonance with good parameters was detected (contrast of 10%, spectral width of 15-20 MHz) was $50 \mu\text{m}$, and the coupling radiation was focused to reach the intensity 1 W/cm^2 . When L decreased further (NTC with $L = 3 \mu\text{m}$ shown in Fig. 3.7 was used for this purpose), the N -type resonance contrast decreased to 0.5% and the spectrum broadened to 30 – 40 MHz.

To study the behavior of the N -type resonance as a function of the angle Θ between the coupling and probe lasers is important from both fundamental and applied standpoints. Practical importance consists in the fact that, when the coupling and probe lasers have the same polarization, the only possibility of detecting the probe radiation is its spatial separation from the coupling radiation.

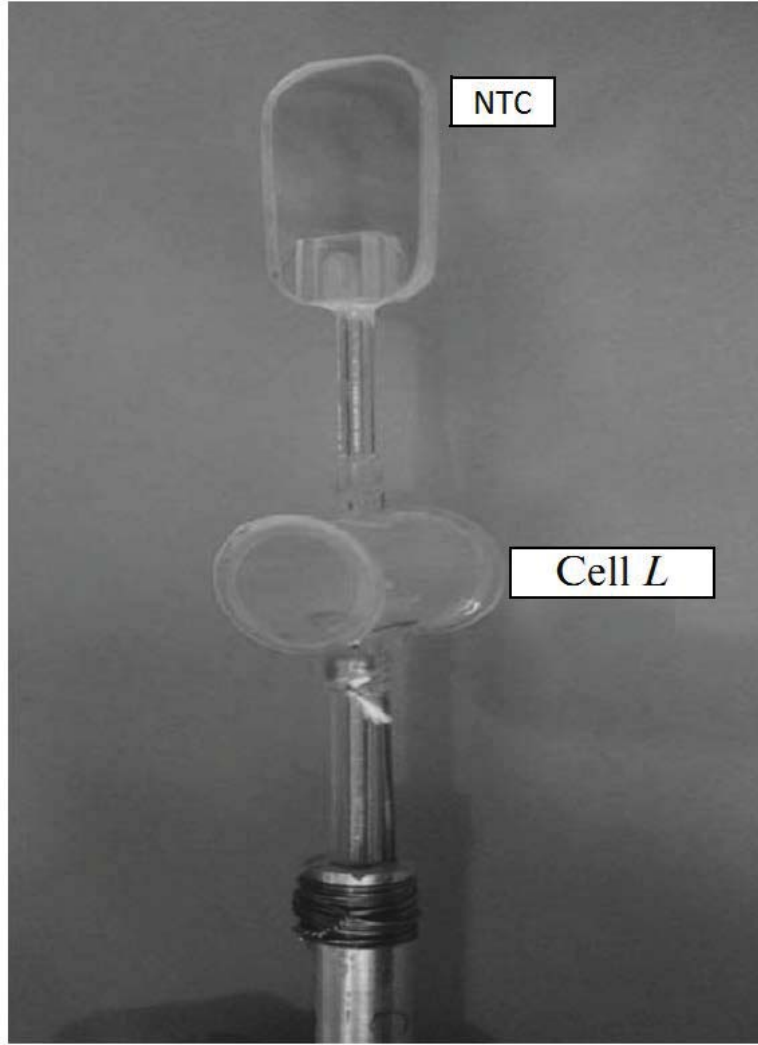


Figure 3.7: Photograph of a two-section (TS) cell containing rubidium vapor and gaseous neon. NTC is shown at the top: the wedge gap between the inner surfaces of the windows changes in the range 50-3000 nm. NTC is connected with the cell of length L , to which another sapphire tube filled with metallic rubidium (reservoir) is connected. At the bottom, the metallic holder on which the TS cell is fixed and the thermocouple used to determine the reservoir temperature are visible.

Figure 3.8 shows the spectra that demonstrate the behavior of the N -type resonance at various θ angles (geometric scheme is shown in Fig. 3.9). The angular dependence of the spectral width is shown in Fig. 3.9. The solid line is the approximation of the spectral width by the empirical formula $\Gamma(MHz) = 9 + 0.02 \theta^{1.9}$ (mrad).

A similar angular dependence was detected for EIT-resonance in [143], which is explained by similar formation of these resonances, since Λ systems are used in both cases and the lower levels are involved in the formation of the EIT and N -type resonances. As is seen from Figs. 3.8 and 3.9, the parameters degrade relatively slowly at low angles (~ 10 mrad), which can be used for the spatial separation noted above. The residual Doppler width resulting

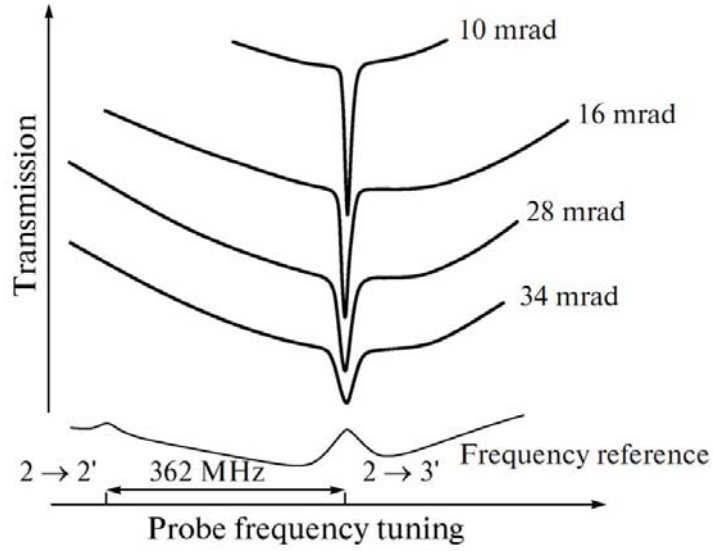


Figure 3.8: N -resonance spectra at various angles θ between the coupling and probe lasers (geometry is shown in the Fig. 3.9). For clarity, the spectra are shifted vertically. An increase in angle θ leads to a decrease in the contrast and an increase in the spectral width of the N -resonance. (lower curve) Transmission spectrum of the frequency reference at NTC thickness $L = \lambda$.

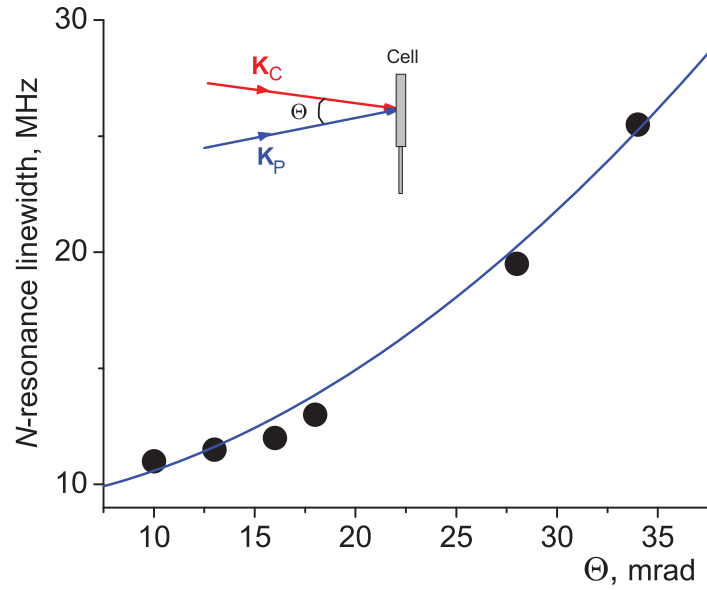


Figure 3.9: Spectral width of the N -resonance vs. angle θ (solid line) approximation by an empirical curve and (inset) schematic diagram for the incidence of the coupling (\mathbf{k}_C) and probe (\mathbf{k}_P) laser reductions onto a cell.

a broadening of the N -type resonance in the case of collinear propagation ($\theta = 0$) along z is $(k_C - k_P)V_z$, where V_z is the projection of the atomic velocity. When angle θ increases, the residual Doppler width increases; however, the width is approximately equal to θ at low angles [143]. A further increase in θ leads to a rapid decrease in the contrast and to an

increase in the spectral width, as was detected for the EIT-resonance.

3.4 The low-frequency beating signal when the condition $\nu_C \approx \nu_P$ is fulfilled

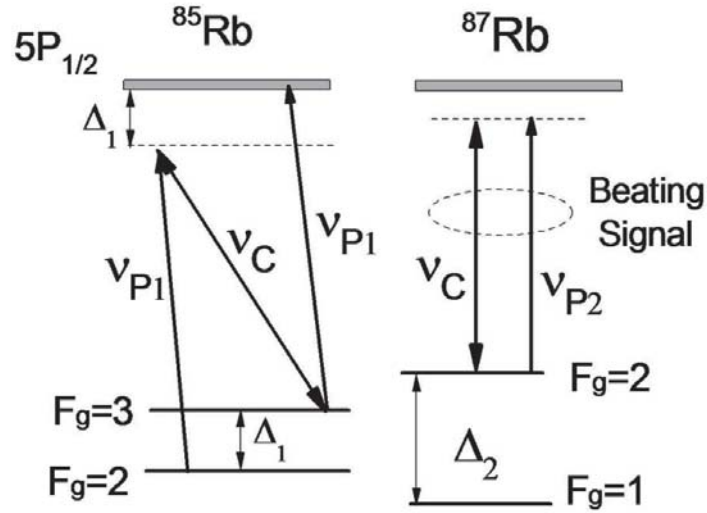


Figure 3.10: The diagram (left part) shows the configuration of ν_C and ν_{P1} required for the N -type resonance formation; the right part shows the configuration of ν_C and ν_{P2} for low-frequency beating signal formation $\nu_C \approx \nu_{P2}$.

While forming N -type resonance using the configuration of ν_C and ν_{P1} shown in Fig.3.10, it is possible to detect simultaneously the N -type resonance and low-frequency beating signal of the two optical radiations ν_C and ν_{P2} of small frequency difference. To form N -type resonance the frequency ν_{P1} satisfies the condition $\nu_{P1} = \nu_C + \Delta_1$ ($\Delta_1 = 3036$ MHz) (see Fig. 3.11). For the low-frequency beating signal the condition $\nu_C \approx \nu_{P2}$ is fulfilled. Thus, the frequency separation between N -resonance and the frequency ν_{P2} (where the beating signal occurs) is equal to $\nu_{P1} - \nu_{P2} = 3036$ MHz. So, with the help of the beating signal it is easy to determine directly the coupling frequency ν_C (i.e. without using a wavelength-meter).

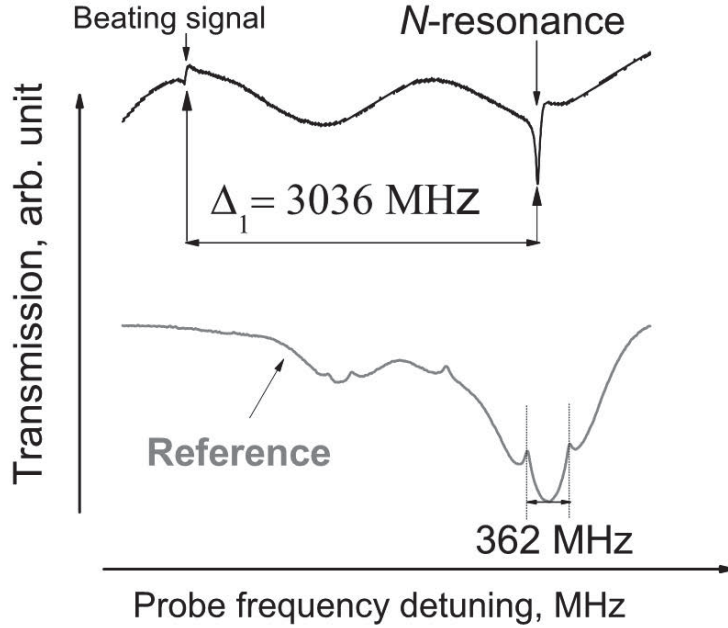


Figure 3.11: The upper curve shows the N -type resonance for the thickness $50 \mu\text{m}$ and the low-frequency beating signal with the frequency interval between them $\Delta_1 = 3036 \text{ MHz}$. The lower grey curve is the Reference spectrum.

3.5 Simultaneous Observation of N - and EIT-Resonances in Micrometric Thin Cell

Under some experimental conditions it is possible to detect simultaneous observation of N - and EIT- resonances formation using Rb MR-cell with the thickness $L = 40 \mu\text{m}$ and filled with 150 Torr neon gas (see Fig. 3.12).

For N - and EIT-resonances formation in Λ -system two lasers are used: the probe (with tunable frequency), and the coupling (with the fixed frequency) with $\lambda \approx 795 \text{ nm}$ wavelength and 1 MHz- line-width. The probe frequency scans the Rb, D_1 line, $5S_{1/2} \rightarrow 5P_{1/2}$ transition, while the coupling frequency is fixed. The N -type resonance demonstrates sub-natural increase of the probe absorption and is formed when probe frequency ν_{P1} is resonant with the ^{85}Rb , $F_g=2 \rightarrow 5P_{1/2}$ transition, while for the coupling frequency the condition $\nu_C = \nu_{P1} + \Delta_1$ ($\Delta_1 = 3036 \text{ MHz}$) is fulfilled (see Fig. 3.13). The EIT- resonance demonstrates sub-natural reduction of the probe absorption and is formed when ν_{P2} scans the ^{87}Rb transition $F_g=2 \rightarrow 5P_{1/2}$ and for the same coupling frequency the condition $\nu_C = \nu_{P2} + \Delta_2$ ($\Delta_2 = 6835 \text{ MHz}$) is fulfilled. Thus, the frequency interval presented in Fig. 3.12 between the N - and the

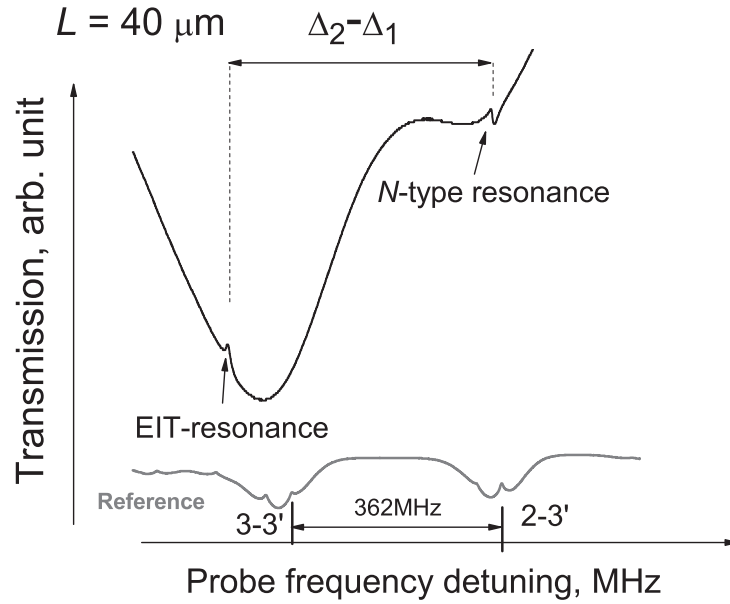


Figure 3.12: The upper curve shows simultaneous detection of the N - and EIT-resonances for the thickness $L = 40 \mu\text{m}$, 150 Torr neon. The frequency interval between N - and EIT-resonances is equal to $\Delta_2 - \Delta_1 = 3.8 \text{ GHz}$. $P_C = 20 \text{ mW}$, $P_P = 2 \text{ mW}$. The lower grey curve is the reference spectrum.

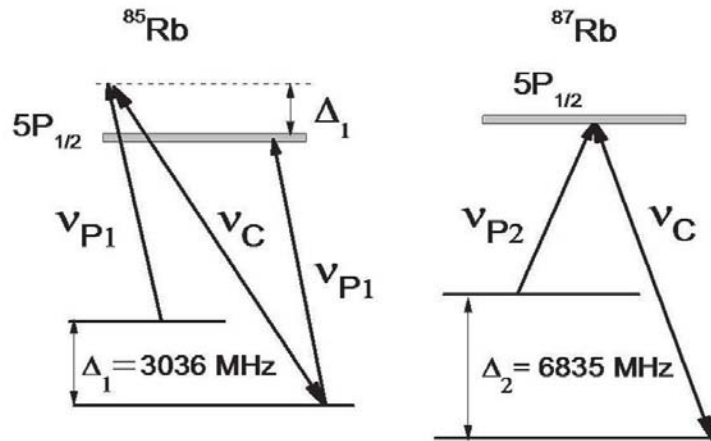


Figure 3.13: The diagram (left part) shows the configuration of ν_C and ν_{P1} required for the N -type resonance formation $\nu_{P1} = \nu_C - \Delta_1$; the right part shows the configuration of ν_C and ν_{P2} for the EIT-resonance formation $\nu_{P2} = \nu_C - \Delta_2$, thus, $\nu_{P1} - \nu_{P2} = \Delta_2 - \Delta_1$.

EIT-resonances is equal to $\Delta_2 - \Delta_1 = 3799 \text{ MHz}$.

In this chapter the study of N -type resonance formation in microcell filled with rubidium and buffer gas is made. The explanation of N -resonance formation is given. The comparison between N - and EIT-resonance formation is made.

In next chapter the N -resonance behavior under the influence of moderate and strong magnetic field is presented. The explanation of N -resonance splitting into three, five and six components for different isotopes of rubidium and different configuration of magnetic field is given.

Chapter 4

The N -type resonance splitting in magnetic field using microcell with the addition of neon buffer gas

4.1 The N -type resonance splitting on three components: ^{87}Rb , D_1 -line

In this section we give the N -type resonance observation, when Λ -system in D_1 -line of rubidium atoms is employed and the radiations of two lasers are used [135–137]. Figure 4.1 shows the scheme of formation of N -resonance in the Λ -system of D_1 -line of ^{87}Rb atoms. The lower levels of the Λ -system are those with $F_g = 1, 2$, while the upper level involves two Doppler-broadened hyperfine levels $5P_{1/2}$, $F_e = 1, 2$. The frequency of the probe radiation is scanned over the transitions $F_g = 1 \rightarrow F_e = 1, 2$; and the frequency ν_C of the coupling laser is fixed. In the spectrum of probe radiation N -resonance is formed when the frequency difference is $\nu_C - \nu_P = \Delta$ with Δ the hyperfine splitting of the lower level (6068 MHz).

In the cited works [135–137] the necessary condition of formation of N -resonance was the presence of a buffer gas in the rubidium-vapor cell. The purpose of the present work is to study the behavior (not studied before) of the N -resonance in an external magnetic field with use of rubidium (isotope 87) atomic vapor. Also the possibility has been stated of practical applications of these studies.

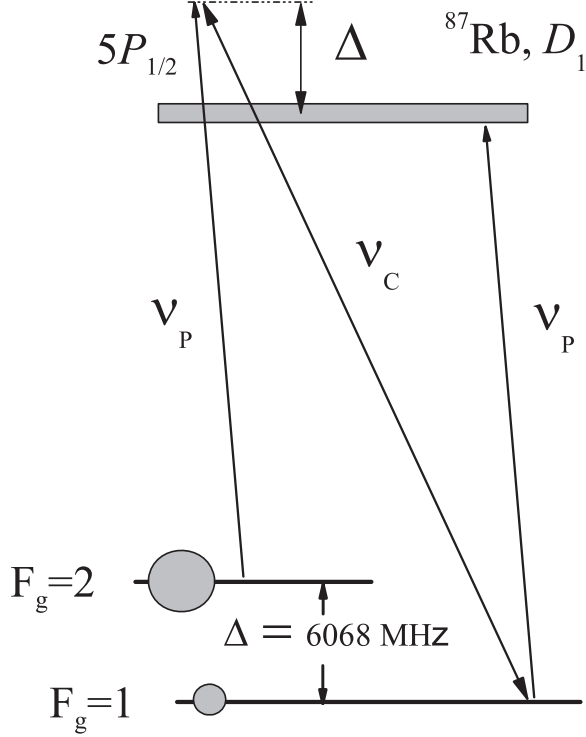


Figure 4.1: Λ -system of D_1 -line of ^{87}Rb atoms; lower levels $F_g = 1, 2$; $F_e = 1, 2$; at frequency $\nu_C - \nu_P = \Delta$. The N -resonance is formed in the spectrum of probe radiation; the resonance exhibits enhancement of absorption. Large circle shows the population N_2 of the level $F_g = 2$ and the small circle the population N_1 of the level $F_g = 1$.

The experiment used a microcell, of $\sim 50 \mu\text{m}$ thickness, filled with rubidium vapor mixed with 100 torr pressure neon as a buffer gas. Rectangular windows with sizes $20 \times 30 \text{ mm}$ and thickness of 2 mm were fabricated of crystalline sapphire. The c -axis was perpendicular to the window surface which reduced essentially birefringence of transmitted radiation. Surfaces of sapphire windows were carefully polished (local roughness $5 < \text{nm}$). In order to produce a wedge-shaped gap (between the inner surfaces of windows), platinum strips, 20 and 80 μm thick, were placed between the windows in the upper and lower parts, respectively. The wedge-shaped gap between the windows was needed for revealing the least thickness of atomic vapor column, for which the studied process is still occurring effectively. This was important for further miniaturization of the cell with the purpose of practical applications [118]. Filling of the microcell was realized with natural rubidium consisting of isotopes ^{85}Rb (72%) and ^{87}Rb (28%). More details of construction of microcells are given in [126,127].

Diagram of the experimental setup is similar to that shown in Fig. 3.5. The $50 \mu\text{m}$ thick cell was used.

For creation of magnetic field in the needed direction a system of Helmholtz coils (2) was employed with the microcell located inside. Radiation of the coupling laser was cut by means of prism G2 and only the probe radiation was recorded. For better selection of the frequency of probe radiation an additional interference filter (6) was used; it had following parameters: 50% transmission at the wavelength 795 nm with the 10 nm width of the transmission peak. Temperature of the side-arm of the microcell (which determines the number density of rubidium atoms in the cell) was about 70 °C (vapor density $\approx 5 \times 10^{11}$ atoms/cm³). The frequency of probe laser ν_P was scanned through the transitions $F_g = 1 \rightarrow F_e = 1, 2$ and the frequency ν_C of the coupling laser was fixed (Fig. 4.1). Shown in Fig. 4.2 (upper curve) is the transmission spectrum of probe radiation when the coupling radiation is present. The contrast of N -resonance (defined as the ratio of the resonance amplitude to its peak absorption) is seen to be reaching 15 %. Note that the contrast of N -resonance is considerably lower in case of employing pure rubidium vapor (interpretation is given below).

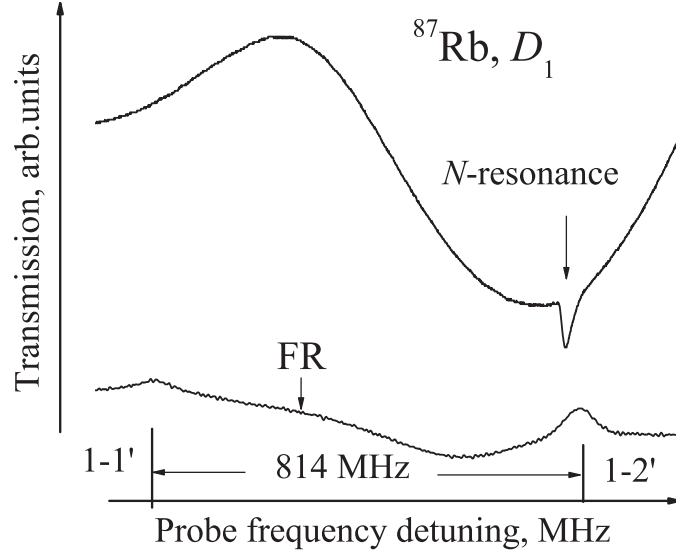


Figure 4.2: Upper curve transmission spectrum involving N -resonance. Contrast is 15%, FWHM 16 MHz. Powers of coupling and probe lasers are, respectively, 27 mW and 1 mW. The lower curve FR is the frequency reference.

The spectral width of N -resonance amounts to ≈ 16 MHz. At strong decrease in the power of coupling and probe lasers the contrast of N -resonance decreases down to several percent with the decrease in the spectral width down to ≈ 5 MHz. The lower curve in Fig. 4.2 is the frequency reference FR which is formed in the nanocell with the thickness $L =$

Λ [11].

High contrast of N -resonance in case where buffer gas is used allows easy tracking its behavior in the external magnetic field in a wide range of field values, from several G to several hundreds of G. In the case of employing ^{87}Rb atoms the N -resonance splits into three or four components (depending on mutual orientation of the magnetic field \mathbf{B} and the laser radiation direction \mathbf{k}). As will be noted below, the behavior of the N -resonance in a magnetic field helps also to identify the physical mechanism of its formation. In case of splitting of N -resonance in magnetic field the lower levels are $F_g = 1$ and $F_g = 2$, which split in the external field, respectively, into three and five sublevels as shown in Fig. 4.3.

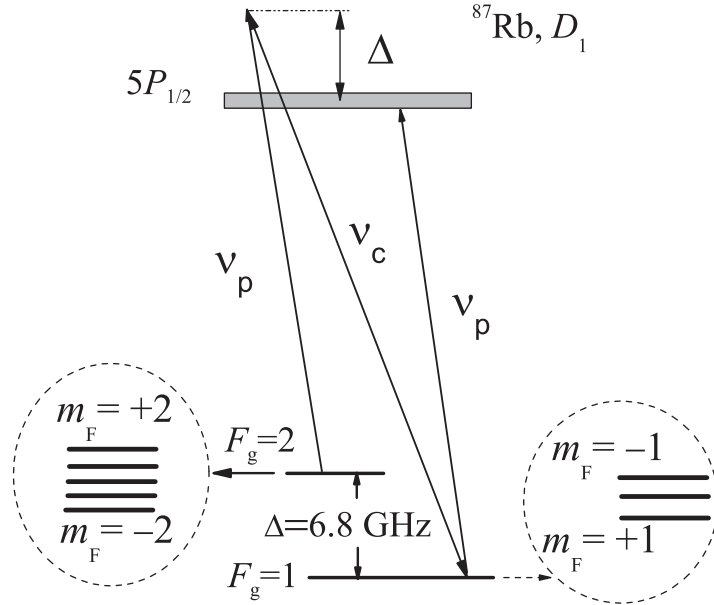


Figure 4.3: In external magnetic field the lower levels $F_g = 1$ and $F_g = 2$, participating in formation of N -resonance, split into, respectively, three and five sublevels (number of sublevels of a level with quantum number F is $2F + 1$).

In the case where the applied magnetic field is longitudinal $\mathbf{B} \parallel \mathbf{k}$, the N -resonance is split into three components shown in Fig. 4.4. Powers of the coupling and probe lasers are, respectively, 27 mW and 1 mW. Depending on the value of the magnetic field, the frequency distance between the components is changed. It is easy to show that at the fields $B < 200$ G the frequency distance between the neighboring components is close to ~ 1.4 MHz/G [87]. Hence, measuring the frequency distance between the components enables determination of the value of the applied magnetic field.

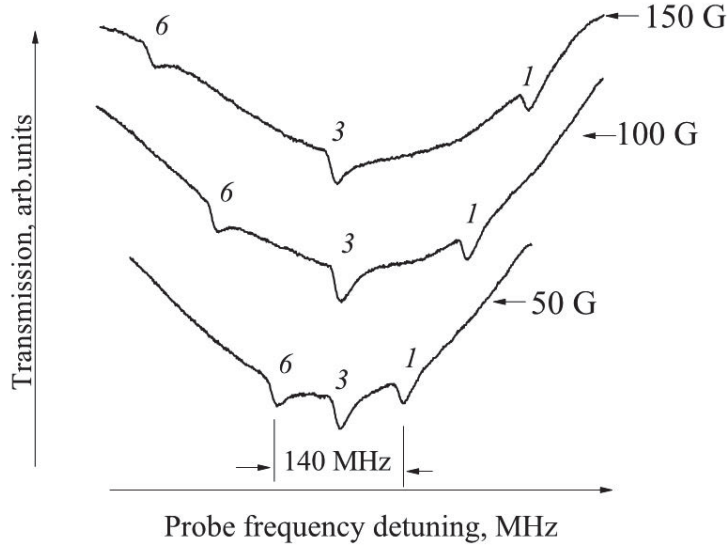


Figure 4.4: Spectra of splitting of N -resonance into three components at different values of the magnetic field: 50, 100, and 150 G. Components are labeled by numbers 1, 3, and 6; component 1 may contain additional component 2 not frequency-allowed; component 3 may involve additional components 4 and 5; component 6 can involve component 7 (see Fig. 4.5).

As seen in Fig. 4.1, for the formation of N -resonance the following condition should be fill:

$$\nu_P - \nu_C = [E(F_g = 2, m_F) - E(F_g = 1, m_F)]/h, \quad (4.1)$$

and the number of components of N -resonance formed in a constant magnetic field and their behavior with frequency are determined by the number and shifts of magnetic sublevels m_F of lower levels $F_g = 1, 2$. In case of D_1 -line of ^{87}Rb the nonlinear energy shift of magnetic sublevels m_F (notation $F = 1, 2$ stands below for $F_g = 1, 2$) may be calculated by the Rabi-Breit formula given, e.g., in works [115, 124]:

$$E(F = 2, m_F) = h\nu_{hfs}[-1/8 + (1/2)(1 + m_F x + x^2)^{1/2}] \text{ for } m_F \neq -2 \quad (4.2)$$

$$E(F = 2, -2) = h\nu_{hfs}(3/8 - x/2) \text{ for } m_F = -2 \quad (4.3)$$

$$E(F = 1, m_F) = h\nu_{hfs}[-1/8 - (1/2)(1 + m_F x + x^2)^{1/2}] \quad (4.4)$$

where $x = 2\mu_B B/h\nu_{hfs}$, μ_B is the Bohr magneton, and $\nu_{hfs} = 6835$ MHz.

Figure 4.5 demonstrates seven curves drawn from formulas (4.1)-(4.4) and describes the frequency positions (shifts) of components of the N -resonance in the magnetic field; black circles are experimental points. Note that the frequencies given by curves 4 and 5 coincide completely at all values of the magnetic field, therefore only six different frequency components of N -resonance are possible. Figure 4.5 shows that in fields below 200 G three components of N -resonance are formed: 1 (may contain additional component 2), 3 (may contain additional components 4 and 5), and 6 (may contain additional component 7). These additional components may possibly be recorded, if formation of narrower (with the width of 12 MHz) components of the N -resonance will be provided. In formation of components 1, 3, and 6 of the N -resonance, as in the case of study of electromagnetically induced transparency [115], three Λ -systems are involved with the following lower sublevels of hyperfine structure of the lower level $5S_{1/2}$ ($F_g = 1, m_F; F_g = 2, m_F$): (1,+1,2,+1), (1,0,2,0), and (1,-1,2,-1), respectively.

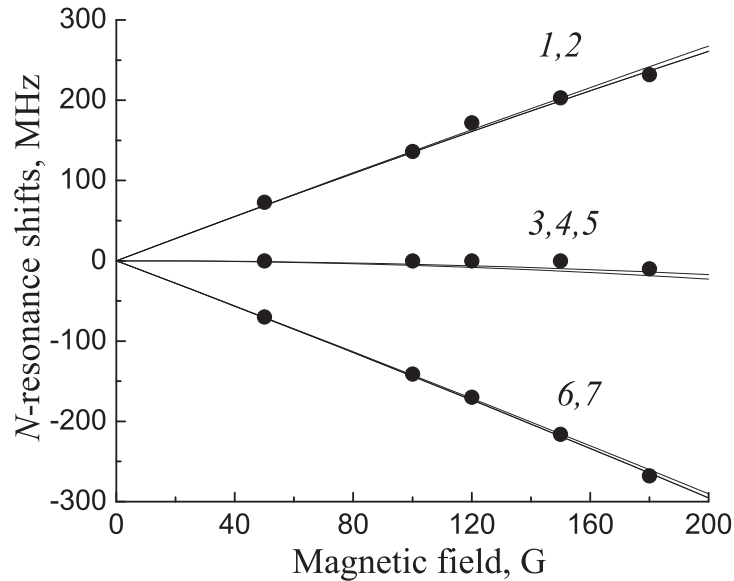


Figure 4.5: Magnetic field dependence of frequency-shifts of N -resonance components. Solid curves: theory, black circles: experiment.

As show the described results on splitting of N -resonance in magnetic field, the initial and the final states are the lower levels $F_g = 1, 2$. Hence, the following mechanism of formation of N -resonance is possible: probe radiation moves atoms from the level $F_g = 1$ to the state $5P_{1/2}$ with subsequent decay to $F_g = 2$ (the so-called process of optical pumping [144]). This

leads to depletion of the level $F_g = 1$ (its population N_1 is shown in Fig. 4.1 by a small circle) and increase in population of the level $F_g = 2$ (its population N_2 is shown by a larger circle). As a result, population inversion arises, $N_2 > N_1$ and at corresponding frequency of the coupling laser two-photon absorption occurs [145]: the atom absorbs from the level $F_g = 2$ a photon of probe radiation ν_P , then goes to $F_g = 1$ emitting a photon at the frequency ν_C . As a consequence, in the spectrum of probe radiation a narrow N -resonance appears (which may be more correctly called cascade resonance) demonstrating enhanced absorption. The amplitude of N -resonance is proportional to $\exp[\sigma_{ta}(N_2 - N_1)L]$, where σ_{ta} is the cross-section of two-photon absorption (it depends on the detuning Δ , intensity of the coupling laser, and probabilities of transitions $F_g = 1 \rightarrow 5P_{1/2}$, $F_g = 2 \rightarrow 5P_{1/2}$) and L the length of the rubidium vapor column. An additional confirmation of this mechanism is also the fact of abrupt improvement of the contrast of N -resonance when a buffer gas is used. This is explained by the fact that in the case of Λ -system lower levels are weakly broadened by the buffer gas [54] and the prevailing effect is the increase in the time of staying of atoms in laser beam (atomic diffusion rate in the presence of buffer gas is several orders of magnitude lower than the thermal velocity of atoms in pure rubidium vapor) and, hence, more efficient optical pumping which is proportional to the time of interaction. This leads to the increase in the population N_2 and consequently to the increase in the amplitude of N -resonance.

4.2 The N -type resonance splitting on five components:

^{85}Rb , D_1 -line

The N -resonance was formed in a Λ -system by two lasers beams with $\lambda \approx 795$ nm and 1 MHz linewidth: the probe beam, whose frequency could be tuned, and the coupling beam, whose frequency was fixed. The diagram presented in the inset of Fig. 4.6 shows the Λ -system for the ^{85}Rb atom, where $F_g = 2, 3$ are the ground levels, and the combined upper level $5P_{1/2}$ consists of hyperfine levels $F_e = 2, 3$. The probe laser frequency ν_P is resonant with the $F_g = 3 \rightarrow 5P_{1/2}$ transition, and the coupling laser frequency is shifted by the value of the ground state hyperfine splitting (Δ_{HFS}): $\nu_C = \nu_P - \Delta_{HFS}$. The experimental arrangement is sketched in Fig. 3.1.

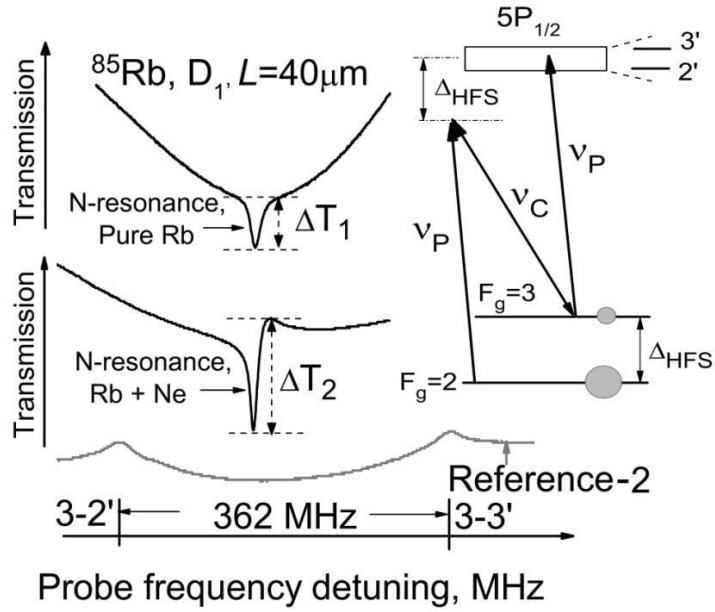


Figure 4.6: Transmission spectra of the probe radiation through the MTC with $L = 40 \mu\text{m}$. Spectra containing an N -resonance are presented for two cases: pure Rb vapor (upper curve), which give a linewidth of around 10 MHz, and Rb with 150 Torr Ne (lower curve), which give a linewidth of around 8 MHz. Spectra were obtained under nearly identical conditions. For convenience, the spectra are shifted in the vertical direction. The lower grey curve is the spectrum of Reference-2. Inset: relevant energy levels of ^{85}Rb involved in N -resonance formation.

Although the best N -resonance contrast and linewidth can be achieved for cells with thicknesses around 1 cm [2, 135–138], using an MTC with a thickness as small as 30 to $40 \mu\text{m}$ still allowed us to obtain good resonance parameters. The experimentally recorded N -resonance spectra are presented in Fig. 4.6. The MTC side arm, whose temperature determines the density of Rb atoms, was maintained at $\sim 110^\circ\text{C}$ (Rb atomic vapor density 10^{13} cm^{-3}).

In the case of the pure Rb vapor (the upper curve) the change of the probe transmission over the N -resonance was $\Delta T_{\text{Rb}} \approx 7\%$, and its lineshape was symmetric. For the buffered cell (the lower curve) the change was larger ($\Delta T_{\text{Rb+Ne}} \approx 12\%$), and the N -resonance shape was asymmetric, consistent with the results reported in [137]. However, the sharp profile of the transmission signal in this case makes it convenient for studying the splitting of N -resonances in a magnetic field.

The N -resonance was split into 5 components in a magnetic field. This splitting is shown in Fig. 4.7 for the B -field varying from 59 G to 460 G. The coupling and probe beam powers

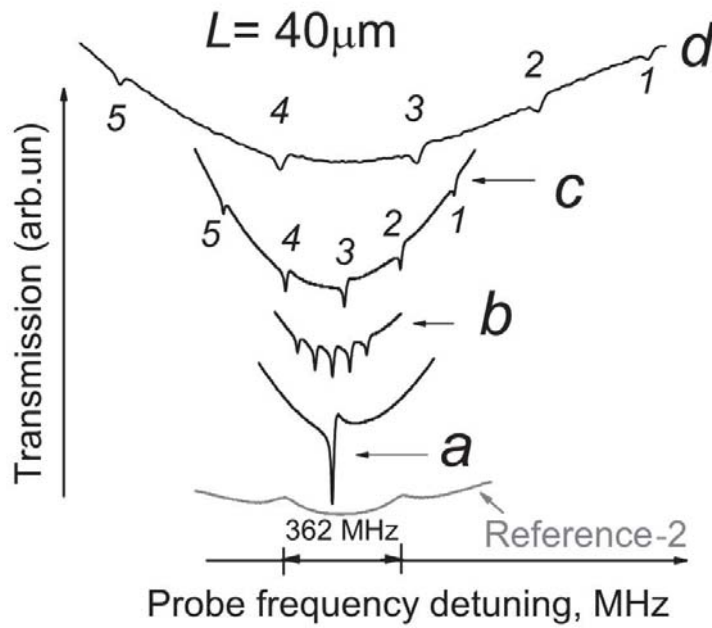


Figure 4.7: Splitting of the N -resonance in a moderate B -field. a: spectrum of Reference-1 for $B = 0$; b - d: N -resonance spectra for $B = 59$ G (b), 190 G (c), and 460 G (d). The labels 1-5 denote corresponding transitions shown in Fig. 4.10. The lower grey curve shows spectrum of Reference-2.

were 4 mW and 1 mW, with a beam diameter of 1.5 mm.

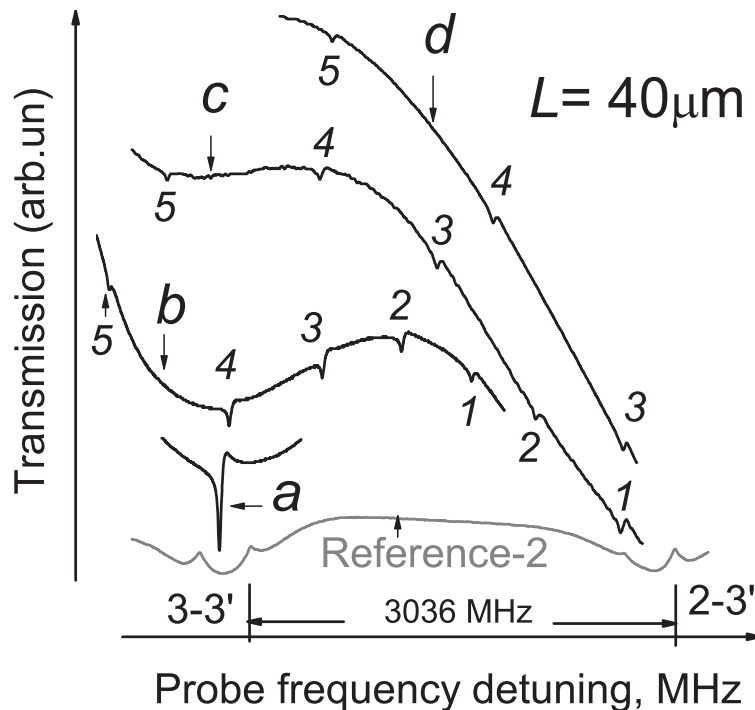


Figure 4.8: Splitting of the N -resonance in a strong B -field. a: spectrum of Reference-1 for $B = 0$; b - d: N -resonance spectra for $B = 808$ G (b), 1238 G (c), and 1836 G (d). The labels 1-5 denote corresponding transitions shown in Fig. 4.10. The lower grey curve shows spectrum of Reference-2.

Spectra showing splitting for stronger B -field values (808 -1836 G) are presented in Fig. 4.8. Although the amplitudes of the N -resonance components tended to decrease with B , they were nevertheless easily observable up to $B = 2200$ G. As can be seen from Fig. 4.7 and Fig. 4.8, the narrow linewidth of the N -resonance makes it possible to achieve a spectral resolution that is higher by a factor of 5 as compared with the results obtained by the λ -Zeeman technique [140]. Although the amplitudes of the N -resonance components tended to decrease with, they were nevertheless easily observable up to $B = 2200$ G. The calculations by the model presented in [141] for pairs of ν_C and ν_P values show that, at high magnetic field, the transition probability on either ν_C or ν_P strongly reduces, resulting in reduction of N -type resonance amplitude.

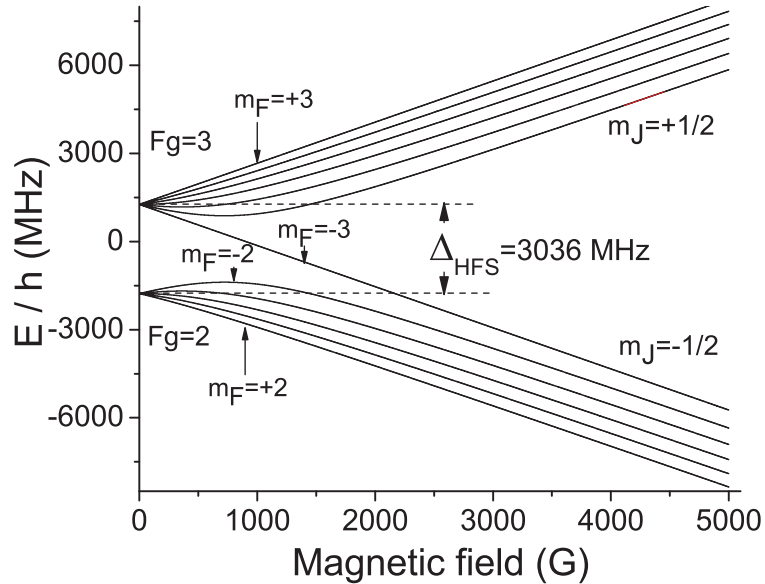


Figure 4.9: Splitting of ^{85}Rb $5S_{1/2}$ ground level hyperfine structure in an external magnetic field.

Figure 4.9 presents the dependence of the frequency of the magnetic sublevels of the ^{85}Rb $F_g = 2, 3$ ground hyperfine states on the magnetic field, as calculated by a well-known model (see, for example, [124]). The system is described in the basis of (F, m_F) in the low-field (Zeeman) regime, and in the basis of (m_J, m_I) in the strong-field (hyperfine Paschen-Back [HPB]) regime, when $B \gg 700$ G [140]. N -resonance components are observed whenever the 2-photon resonance conditions are satisfied: $\nu_P - \nu_C = [E(F=3, m_F) - E(F=2, m_F)]/h$.

Figure 4.10 shows the magnetic field dependence of the frequency shift for the five observed N -resonance components. Other N -resonance components expected from the calcu-

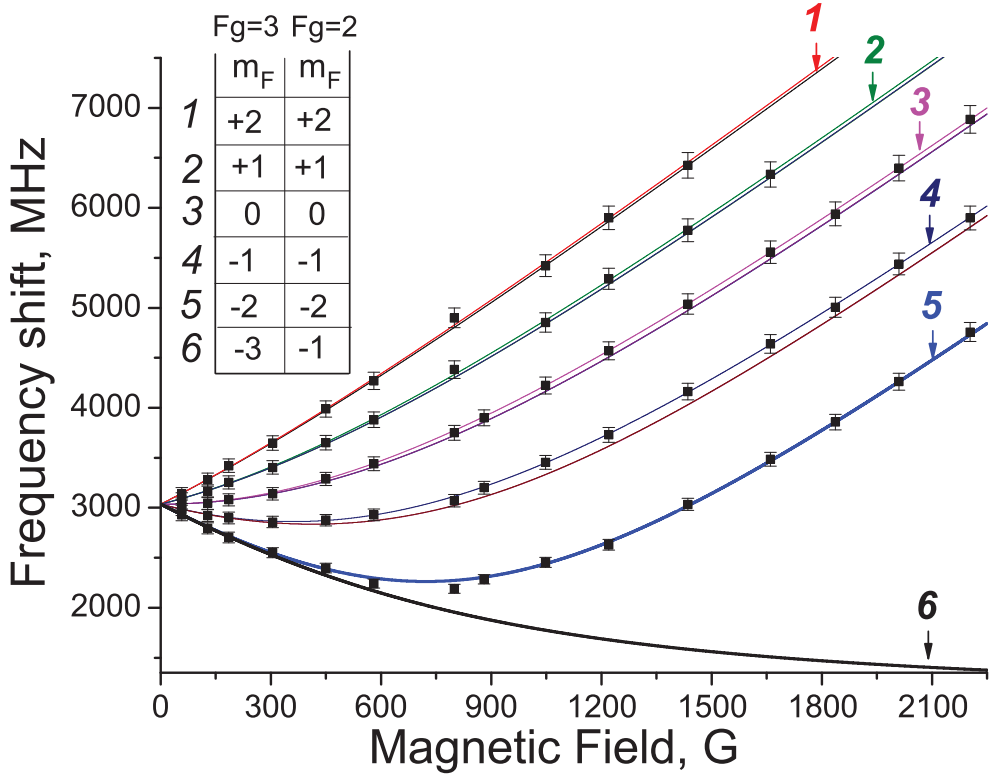


Figure 4.10: Frequency shifts of the N -resonance components in a B -field. *Solid lines*: theory; *symbols*: experiment. The inaccuracy does not exceed 2%. The initial and final Zeeman sublevels of $F_g=2,3$ are indicated in the Table for components 1-5. For the component labeled 6 the linked sublevels are $F_g=2, m_F=-1$ and $F_g=3, m_F=-3$.

lations and presented as thin solid lines in Fig. 4.10 are not observable in the experiment because at low fields ($B < 500$ G) their separation from components 1-5 is unresolvably small (several MHz), while at high fields the atomic transition probabilities (line strengths) are reduced (either for the coupling or for the probe radiation) down to undetectable values (see component 6, undetectable for $B > 500$ G). Note that the slope of components 1-5 contains contributions from the B -field shifts of the corresponding ground-state Zeeman sublevels $F_g=2,3$ (see Fig. 4.9). Thus, N -resonance component 1 has the largest slope of 2.68 MHz/G in the region around 2 kG, that is, $|-1.34|$ MHz/G from $F_g=2, m_F=+2$, and $|+1.34|$ MHz/G from $F_g=3, m_F=+2$. For $B > 1.5$ kG an HPB regime becomes predominant. As a consequence, the slopes of components 1-5 tend to equalize at the same final value of ~ 2.8 MHz/G.

4.3 The N -type resonance splitting into six components: ^{85}Rb , D_1 -line

For ^{85}Rb atoms, the N -type resonance in a magnetic field splits into five or six components depending on the mutual orientation of field \mathbf{B} and laser radiation direction \mathbf{k} .

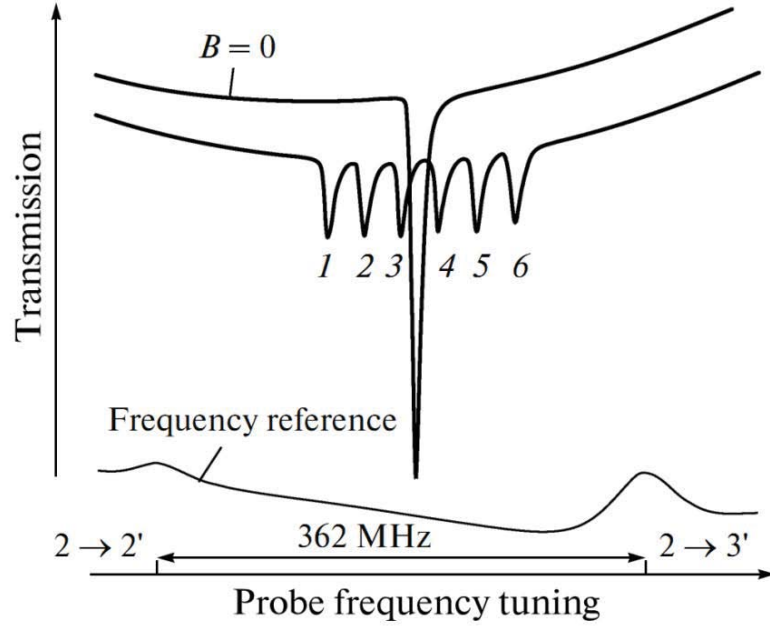


Figure 4.11: (upper curve) N -resonance at $B = 0$, (medium curve) splitting of the N -resonance into six components in a transverse magnetic field $B = 30$ G, and (lower curve) transmission spectrum of the frequency reference at UTC thickness $L = \lambda$.

The upper curve in Fig. 4.11 shows the N -resonance for the case when the magnetic field is absent ($B = 0$). The medium curve demonstrates the splitting of the N -type resonance into six components in a magnetic field $B = 30$ G (transverse magnetic field $\mathbf{B} \perp \mathbf{k}$ is applied). We used a cell with rubidium vapor and neon at a pressure of 20 Torr. The powers of the coupling (P_C) and probe (P_P) lasers were 18 and 3 mW, respectively. As is seen from Fig. 4.11, all six components have a good contrast and a width of approximately 6 MHz, which is smaller than the initial N -resonance at $B = 0$ by a factor of 1.4. A similar narrowing was reported in [111], where the splitting of the EIT-resonance in a magnetic field was studied.

Figure 4.12 shows the diagram of the $F_g = 2$ and $F_g = 3$ levels of the ^{85}Rb atom, which split into $2F + 1$ Zeeman sublevels (5 and 7 sublevels, respectively) in an applied magnetic field. For clarity, the splitting of the upper $5P$ level is not shown in Fig. 4.12 (the effect

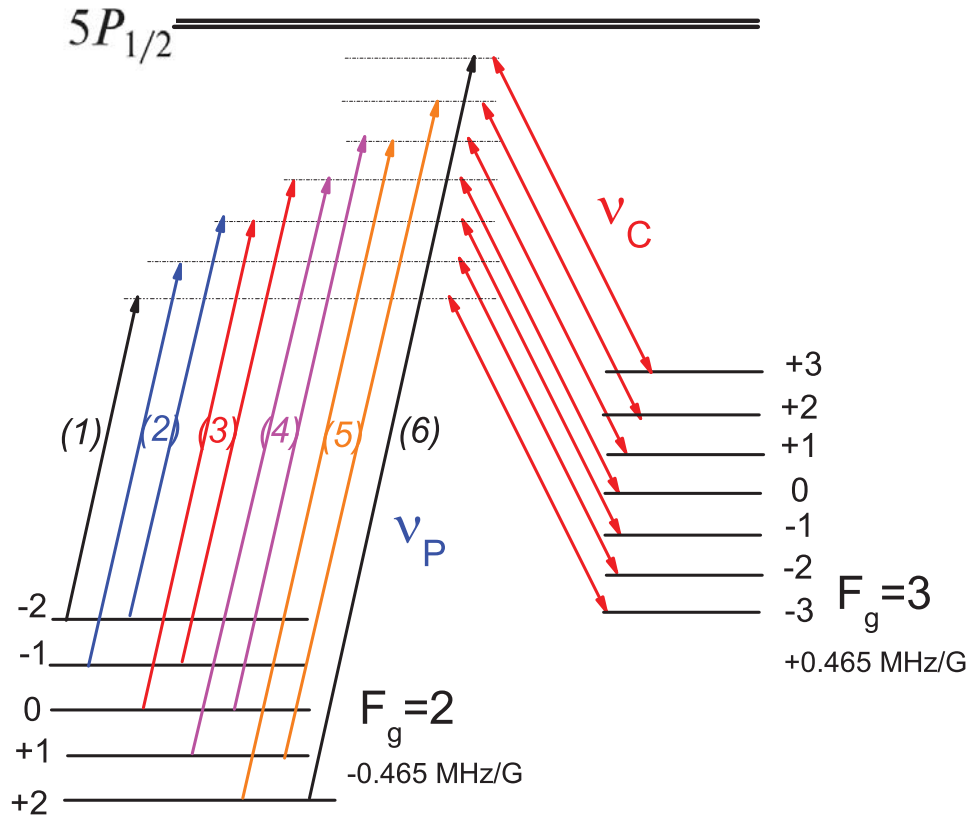


Figure 4.12: Diagram of levels $F_g = 2$ and 3 of the ^{85}Rb atom, which split into 5 and 7 sublevels in an applied magnetic field, respectively. Ten possible pairs of the coupling (ν_C) and probe (ν_P) laser frequencies are shown. The pairs for which probe laser frequencies are the same are indicated by different colors. Components (1) and (6) contain one transition. This diagram is seen to be the same if frequencies ν_C and ν_P are permuted.

of the upper level manifests itself in the change in detuning Δ induced by a change in the magnetic field, which only affects the N -resonance amplitude (see Fig. 3.2)). This diagram shows ten possible pairs of the frequencies of the coupling laser (ν_C) with a fixed frequency and the probe laser (ν_P) with a tunable frequency that can result in two-photon absorption from lower level $F_g = 2$ and the transition of atoms to level $F_g = 3$. It is seen that the probe laser frequencies have the same frequency in some cases (such groups having two transitions with the same frequencies are indicated by different colors), which leads to the appearance of six different frequency components (see Fig. 4.11).

As is seen from the diagram, the frequency shift between two neighboring components is $0.465 + 0.465 = 0.93 \text{ MHz/G}$. If one of the lower levels of the hyperfine structure ($F_g = 2$ or 3) is assumed to be an initial level and one of the upper levels is final ($F_e = 2$ or 3), the frequency shift between two neighboring components should be as follow. In the case where

the lower level is $F_g = 2$ and the final upper level is $F_e = 2$, the frequency shift should be $0.465 - 0.155 = 0.31$ MHz/G; if the final upper level is $F_e = 3$, the frequency shift should be $0.465 + 0.155 = 0.62$ MHz/G. The quantities determining the shifts of the Zeeman sublevels with projection m_F in a magnetic field are given in [146]. The frequency distance between components 6 and 1 (Fig. 4.11) is $(5 \times 0.93 \text{ MHz/G}) \times 30 \text{ G} = 139.5$ MHz; for the case shown in Fig. 4.13, the frequency distance between components 5 and 1 is $(4 \times 0.93 \text{ MHz/G}) \times 15 \text{ G} = 54.8$ MHz. Therefore, the initial and final levels are lower levels $F_g = 2$ and $F_g = 3$. It is important that, irrespective of which of levels $F_g = 2$ and 3 is the initial or final level, the frequency shift between neighboring components is 0.93 MHz/G, which is observed in experiments (this is true for fields lower than 200 G, where the shift of m_F sublevels depends linearly on the magnetic field [118]).

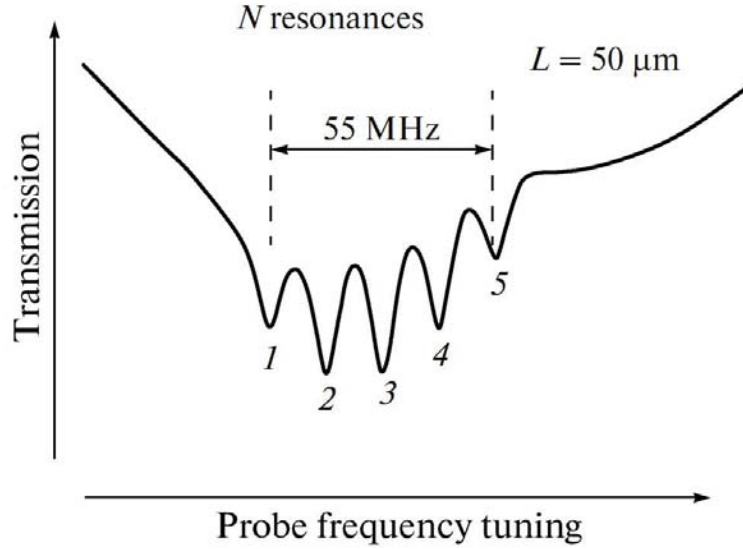


Figure 4.13: Splitting of the N -resonance into five components in a longitudinal magnetic field $B = 15$ G. The atomic vapor column thickness is $50 \mu\text{m}$, and the reservoir temperature is about 100°C .

It is important that, for the case of a cell of thickness $L = 50 \mu\text{m}$ (neon pressure of 200 Torr) and an applied longitudinal magnetic field ($\mathbf{B} \parallel \mathbf{k}$), the N -resonance splits into five narrow (< 6 MHz) components (Fig. 4.13). Powers P_P and P_C were 0.5 and 3 mW, respectively (laser beam diameter of 1 mm). The frequency shift between components 1 and 5 is $4 \times 0.93 = 3.72$ MHz/G. When the magnetic field changes by 1 G, the frequency distance increases by 3.72 MHz and can be detected. This feature can be used to measure strongly inhomogeneous (gradient) magnetic fields with a spatial resolution of $50 \mu\text{m}$. Note

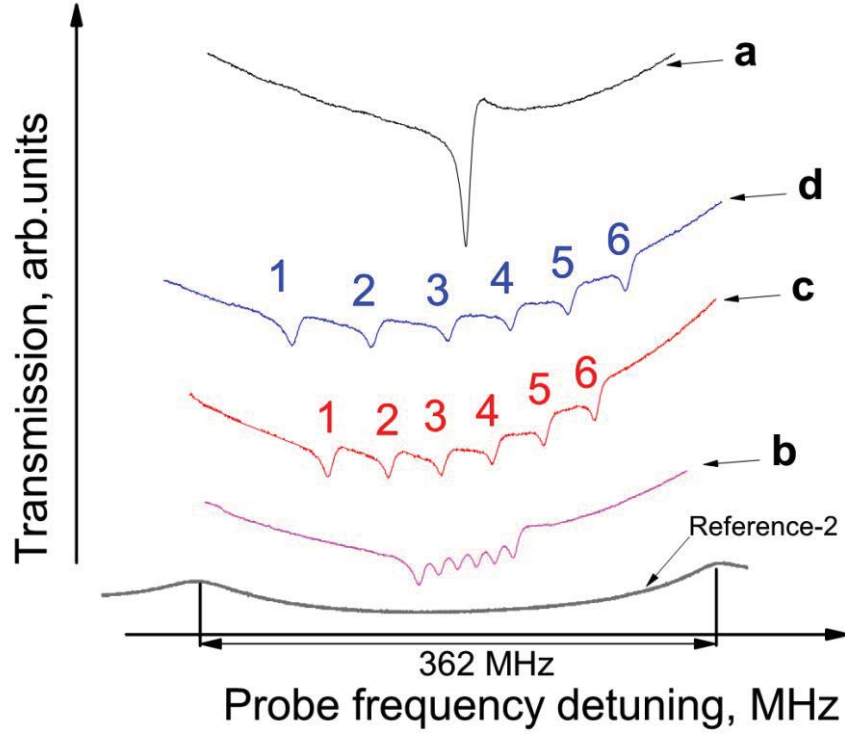


Figure 4.14: Splitting of the N -type resonance in a low B -field. a: spectrum of Reference-1 for $B = 0$; b - d: N -type resonance spectra for $B = 15$ G (b), 40 G (c), and 50 G (d). The labels 1-6 denote corresponding transitions shown in Fig. 4.12. The lower grey curve shows spectrum of Reference-2.

that the spectral resolution achieved using the N -resonance is better by a factor of 5 - 6 than that obtained in [136], in which sub-Doppler resonances were used. The splitting into five components was reliably detected in magnetic fields up to 700 G (to form high magnetic fields, we used the equipment described in [146]).

In Fig 4.14 N -type resonance splitting in 6 components in low magnetic field is shown. The reservoir temperature is about 80°C , cell of thickness $L = 40 \mu\text{m}$ (neon pressure of 150 Torr) and an applied longitudinal magnetic field ($\mathbf{B} \parallel \mathbf{k}$). Powers P_P and P_C were 1 and 4.5 mW, respectively.

Spectra showing splitting for stronger B -field values (250 - 640 G) are presented in Fig. 4.15. Although the amplitudes of the N -resonance components tend to decrease with B , but some of them were observable up to $B = 1400$ G.

Figures 4.16a and 4.17a show the magnetic field dependence of the frequency shift for the six observed N -type resonance components. The diagrams explaining the N -type resonance formation are shown in Fig. 4.16b and 4.17b. Note that changing the frequency ν_P

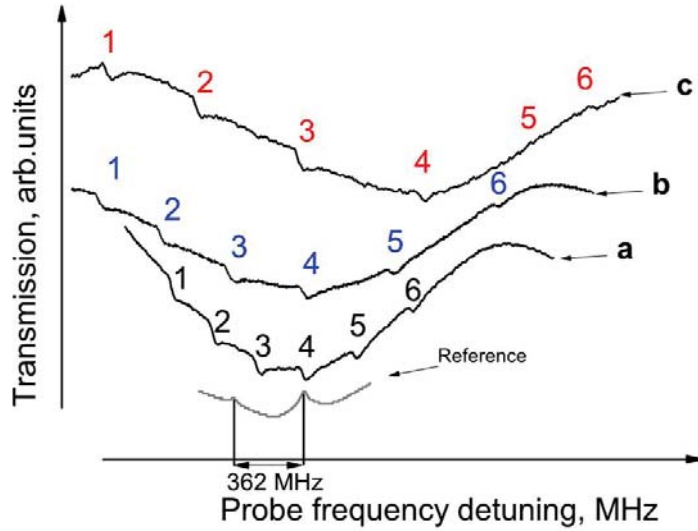


Figure 4.15: Splitting of the N -type resonance in a moderate and high B -field. a - c: N -resonance spectra for $B = 250$ G (a), 425 G (b), and 640 G (c) labels 1-6 denote corresponding transitions shown in Fig. 4.12. The lower grey curve shows spectrum of Reference.

from resonant with $F_g = 3 \rightarrow 5P_{1/2}$ to resonant with $F_g = 2 \rightarrow 5P_{1/2}$, the N -type resonance components frequency shift will be the same multiplied by “-1”.

4.4 Physical mechanisms of N -type resonance formation

We now discuss the N -type resonance formation mechanism. The configuration of frequencies ν_C and ν_P forms letter “ N ” (see Fig. 3.2 and [2, 135–138]). In [2] the authors developed a theoretical model to explain the N -type resonance formation mechanism. In that model, a Λ system of the rubidium atom levels is reduced to the cascade set of levels described above, in which the initial level is one of the lower levels of the hyperfine structure ($F_g = 2$ or 3) and the final level is one of the upper levels of hyperfine structure 5P ($F_e = 2$ or 3). The model satisfactorily describes the detected N -type resonance parameters, but it cannot describe new experimental results. In particular, the splitting of the N -type resonance in a magnetic field indicate that lower levels $F_g = 2$ and 3 are the initial and final levels. It does not follow from the model in [111] that the addition of a buffer gas should improve the contrast; however, the results in [2, 135–138] and our data demonstrate that this is the case. The diagram shown in Fig. 4.18 (configuration of frequencies ν_C and ν_P) well describes these features for the

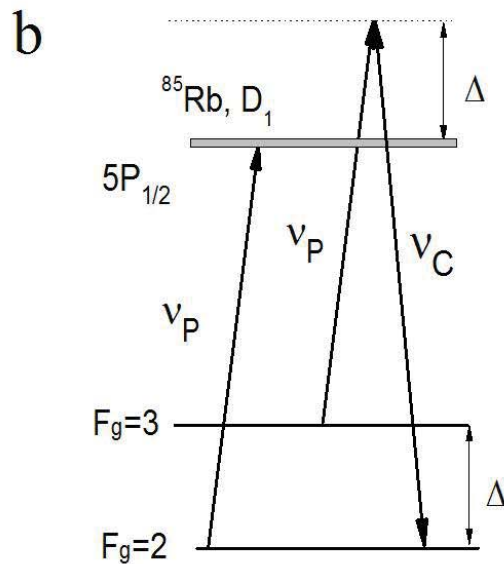
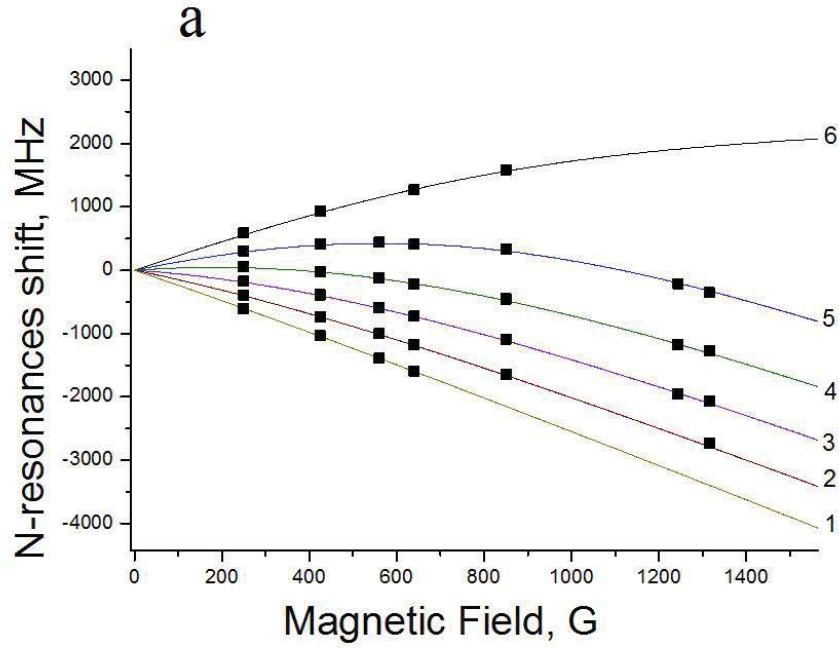


Figure 4.16: a: Frequency shifts of the N -resonance components in a B -field. *Solid lines*: theory; *symbols*: experiment. The inaccuracy does not exceed 2%, b: ^{85}Rb D_1 line diagram shows the configuration of ν_C and ν_P for N -type resonance formation.

following N -type resonance formation mechanism: the probe radiation transfers atoms from level $F_g = 2$ to level $5P_{1/2}$ from which decay to $F_g = 2, 3$ takes place. This is the well-known optical pumping process [144]: level $F_g = 2$ is depleted (population is indicated by the small circle) and the population of $F_g = 3$ increases (population is indicated by the large circle). As a result, population inversion $N_3 > N_2$ appears and two-photon absorption occurs at a

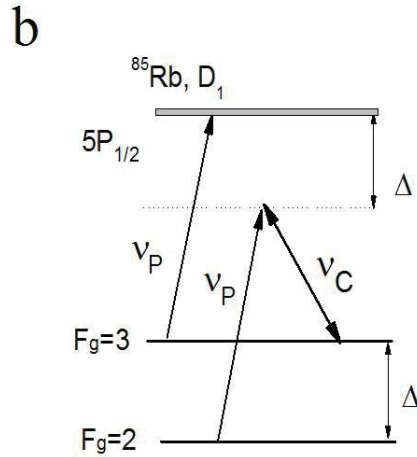
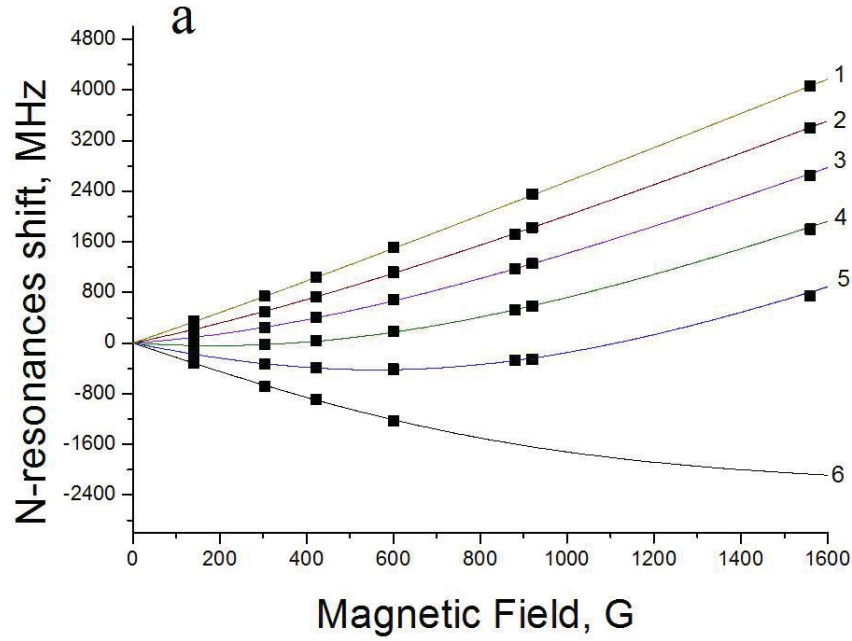


Figure 4.17: a: Frequency shifts of the N -resonance components in a B -field. *Solid lines*: theory; *symbols*: experiment. The inaccuracy does not exceed 2%, b: ^{85}Rb D_1 line diagram shows the configuration of ν_C and ν_P for N -type resonance formation.

certain coupling laser frequency [145]: an atom from level $F_g = 3$ absorbs a probe radiation photon at frequency ν_P , emits a photon at frequency ν_C , and passes to level $F_g = 2$. This results in the formation of a narrow N -type resonance (cascade resonance, to be correct), which exhibits enhanced absorption, in the probe radiation spectrum. The N -type resonance amplitude is approximately $\exp[\sigma_{TA}(N_3 - N_2)L]$, where σ_{TA} is the cross section of two-photon absorption (which depends on detuning Δ , the coupling laser intensity, and the probabilities of the $F_g = 3 \rightarrow 5P_{1/2}$ and $F_g = 2 \rightarrow 5P_{1/2}$ transitions). It is seen that, if the probe radiation is in resonance with the transition $F_g = 3 \rightarrow 5P_{1/2}$, this leads to the depletion of level $F_g =$

3 and an increase in the population of level $F_g = 2$. As a result, inversion $N_2 > N_3$ appears and an atom passes from $F_g = 2$ to $F_g = 3$ due to two-photon absorption at frequency ν'_C (this process is indicated by dashed lines for ν'_{C1} in Fig. 3.2).

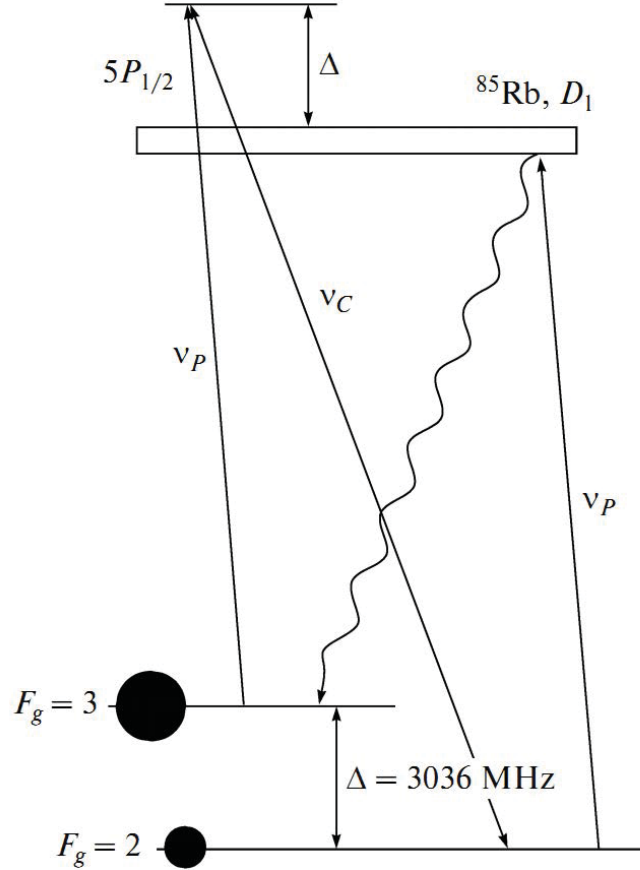


Figure 4.18: Illustration for the N -type resonance formation. The probe radiation in resonance with the transition $F_g = 2 \rightarrow 5P_{1/2}$ transfers atoms from level $F_g = 2$ to level $F_g = 3$, increasing its population (large circle) and decreasing the population of $F_g = 2$ (small circle). This transfer creates inversion $N_3 > N_2$, and two-photon absorption at frequency ν_P accompanied by N -type resonance formation occurs at proper frequency ν_C .

This mechanism is also supported by a substantial improvement of the N -type resonance contrast when a buffer gas is used. This fact is explained as follows: it is known that the lower levels of a Λ -system are weakly broadened by a buffer gas in the pressure range 10-100 Torr (for the case of rubidium atoms and gaseous neon, the collisional cross section that causes electron flipping between $F_g = 2$ and 3 is about 10^{22} cm²) [54]. Thus, the dominating positive effect is an increase in atom transit time t in a laser beam $t = d/v$, where d is the laser beam diameter and v is the atom velocity (*i.e.*, time t of interaction of laser radiation with an atom increases), since the atom velocity (diffusion rate) in the presence of a buffer

gas is several orders of magnitude lower than the atom velocity in pure rubidium vapor. For the case of an exact resonance between probe laser frequency ν_P and an atomic transition, the optical pumping efficiency is proportional to interaction time t [144]. Therefore, more efficient optical pumping and an increase in N_3 are observed. Note that, when pure D_2 -line rubidium vapor was used [142], the contrast was weak, lower than 4% (low contrast in the absence of a buffer gas is caused by a lower value of N_3).

Let us discuss the fact which indicates that $F_g = 3$ (rather than the upper level) is final level for N -type resonance formation. The addition of gaseous neon at a pressure of 10 Torr leads to a strong broadening of level $P_{1/2}$ (up to 100 MHz). It was shown in [147, 148] that, when an EIT resonance forms in a cascade system and upper level $5D$ is the final level, even small addition of a buffer gas results in a broadening of final level $5D$ and decreases the EIT-resonance contrast in the cascade system by several tens of times. The EIT-resonance in pure rubidium vapor (in the same cascade system) has a high contrast [126]. In the theoretical model [2], a Λ -system of the rubidium atomic levels was reduced to the cascade system of levels described above (in which one of the lower levels is the initial level and one of the upper levels is the final level); therefore, as follows from the analogy considered above, the N -type resonance formation in the presence of a buffer gas should be strongly hindered. It is interesting that the buffer gas pressures (330 Torr) used in [2, 135–138] to form an N -type resonance are also optimal for the formation of an EIT-resonance in the same Λ -system for rubidium atoms [1, 54].

Note that the second name of the N -type resonance, namely, three-photon absorption resonance, may cause misunderstanding. Three-photon scattering (absorption) was studied late in the 1960s [149, 150]. This process consists in the following: three-photon scattering takes place for a two-level atom in the presence of detuning $\Delta = \nu_L - \nu_A$ of laser frequency ν_L from atomic frequency ν_A ; as a result, the atom absorbs two laser photons, emits a photon at frequency ν_{3R} , and passes from the lower to the upper state. Therefore, for three-photon scattering, the lower and upper levels are the initial and final levels, which is wrong for the N -type resonance (as was shown by the results of splitting in a magnetic field).

In this chapter the observation of N -type resonance behavior under the magnetic field for

the case of D_1 -line of isotopes 87 and 85 of rubidium in microcell is made. The new physical mechanism of N -resonance formation is suggested and proved.

Conclusion

In this work, we made the detailed observation of coherent effects, such as electromagnetically induced transparency resonance (using nanocell and microcell) and N -type resonance (using microcell) in rubidium atomic vapor under bi-chromatic laser radiation.

For this purpose in the first chapter we demonstrated that usage of nanocell filled with atomic vapors and narrow-band extended cavity diode lasers allows to obtain narrow electromagnetically induced transparency resonance with good (40%) contrast, which allow to realize spectroscopy of high resolution, and to observe the behavior of EIT-resonance under the influence of high magnetic field. We have proved advantages of the methods based on use of a nanocell in further usage of EIT-resonance for magnetic field mapping and miniaturization of devices, where the effect of EIT can be used.

In second chapter we present the behavior of EIT-resonance in magnetic field, for the D_1 -line of Rb atoms. We showed, that due to B magnetic field the initial EIT-resonance splits into new 3 EIT-resonances (3 components) in case of ^{87}Rb D_1 -line. We demonstrated, that for the case of ^{87}Rb D_1 -line, the three components behavior is depending on the frequency detuning of the couple radiation from the corresponding sublevels. We showed, that for a magnetic field $B > 350$ G only two components are detectable, and for $B > 1200$ G only one of EIT components is seen. The experimental results for the isotope 87 of Rb are presented. The theoretical calculations for ^{87}Rb are made. Comparison of theoretical and experimental results is made and good agreement between them is presented, which allows one to develop the magnetometer based on EIT effect on D_1 -line of ^{87}Rb .

Also we reported about the experimental investigation of the behavior of the EIT-resonance

in strong magnetic fields up to 1.7 kG with the use of the 30 μm cell filled with an atomic rubidium vapor and a buffer gas (neon). It is shown that the EIT-resonance in the Λ -system of the D_1 -line of ^{85}Rb atoms in a longitudinal magnetic field splits into five components, whose frequency behavior depends on the frequency configuration of the probe and coupling fields and the magnitude of the magnetic field. It is also shown that the study of the characteristics of the EIT-resonance components in high magnetic fields can readily reveal the onset of the Paschen-Back regime for the hyperfine structure of the atoms.

In chapter three we presented the N -type resonance formation in microcell. We presented the diagram of D_1 -line of ^{85}Rb for N -resonance formation. Observation of narrow-band cascade N -resonance that forms in a Λ -system of rubidium atoms in cells with $L = 8$ mm and 40-90 μm in the presence of neon gas at a pressure of 6, 20, 200, and 400 Torr is done. Detection of the N -resonance at a minimum vapor column thickness of 40 μm is presented. The dependence of N -resonance parameters on the angle between two lasers (which are used to form the resonance) is presented.

Also we made the report of simultaneous observation of the N - and EIT-resonance formation using multi-region cell filled with natural Rb and 150 Torr neon gas (containing micrometric-thin region with the thickness L varying in the range of 1 μm - 90 μm). Simultaneous detection of the low-frequency beating signal and N -resonance is made, which allows the coupling laser frequency direct determination. Possible applications are addressed.

In fourth chapter we presented the N -type resonance splitting in magnetic field using microcell with the addition of neon buffer gas. Results of studies of behavior of N -resonance formed in a Λ -system of D_1 -line of atomic ^{87}Rb vapor in external magnetic fields in the range of 1-200 G, with the use of microcell with the thickness of column of rubidium atoms $L = 50$ μm are presented. Considered theoretical model explains well the splitting of N -resonance into three components in the external magnetic field for the case of D_1 -line of ^{87}Rb .

We presented the N -type resonance splitting on five components in D_1 -line of atomic ^{85}Rb in range of longitudinal magnetic field 1-2100 G. Experimental results are shown. The theoretical calculations of the frequency shift of N -resonance components are made. Com-

parison of theoretical and experimental results is given and good agreement between them is presented.

We also presented the N -resonance splitting on six components for D_1 -line of atomic ^{85}Rb in magnetic field. The experimental results and theoretical calculations are presented and the good agreement between them is shown.

Physical mechanisms of N -type resonance formation are described.

Bibliography

Cited literature

- [1] M. Fleischhauer, A. Imamoglu, and J. P. Marangos, “Electromagnetically induced transparency: Optics in coherent media”, *Rev. Mod. Phys.* **77**, 633-673 (2005).
- [2] A. S. Zibrov, C. Y. Ye, Y. V. Rostovtsev, A. B. Matsko, and M. O. Scully, “Observation of a three-photon electromagnetically induced transparency in hot atomic vapor”, *Phys. Rev. A* **65**, 043817 (2002).

Papers included in the thesis

- [3] R. K. Mirzoyan, “Study of optical narrow-band N -resonance formed in the vapor of isotope ^{87}Rb atoms in an external magnetic field”, *Journal of Contemporary Physics (Armenian Academy of Sciences)* **48**, 26 (2013).
- [4] A. Sargsyan, R. Mirzoyan, A. Papoyan, D. Sarkisyan, “ N -type resonances formation in micrometric-thin cells filled with Rb and buffer gas: splitting in strong magnetic field”, *Optics Letters* **37**, 4871 (2012).
- [5] A. Sargsyan, R. Mirzoyan, D. Sarkisyan, “Splitting of the electromagnetically induced transparency resonance on ^{85}Rb atoms in strong magnetic fields up to the Paschen-Back regime”, *JETP Letters* **96**, 303 (2012).
- [6] A. Sargsyan, R. Mirzoyan, D. Sarkisyan, “Narrow-Band N -resonance Formed in Thin Rubidium Atomic Layers”, *Journal of Experimental and Theoretical Physics* **115**, 769 (2012).

- [7] A. Sargsyan, G. Hakhumyan, R. Mirzoyan, A. Papoyan, D. Sarkisyan, C. Leroy, Y. Pashayan-Leroy, "Selective Amplification of Narrow Resonance Formed in Transmission Spectrum of Rb nanocell in Magnetic Field", Intern. Journ. of Modern Physics: Conference Series **15**, 9 (2012).
- [8] A. Sargsyan, R. Mirzoyan, D. Sarkisyan, "A study of dark resonance splitting for the D_1 -line of ^{87}Rb in strong magnetic fields", Optics and Spectroscopy **113**, 456 (2012).
- [9] G. Hakhumyan, R. Mirzoyan, C. Leroy, Y. Pashayan-Leroy, D. Sarkisyan, "Study of Forbidden Atomic Transitions on D_2 line Using Rb nanocell placed in External Magnetic Field", Eur. Phys. J. D **66**, 119 (2012).
- [10] A. Sargsyan, R. Mirzoyan, S. Cartaleva, D. Sarkisyan, "Simultaneous Observation of N- and EIT- Resonances in 40-micron Thin Cell Filled with Rb and Buffer gas", Proc. SPIE 8770, 17th International School on Quantum Electronics: Laser Physics and Applications, 87700K (March 2013); doi: 10.1117/12.2010673.
- [11] A.Sargsyan, Y. Pashayan-Leroy, C. Leroy, R. Mirzoyan, A. Papoyan, D. Sarkisyan, "High contrast D_1 -line electromagnetically induced transparency in nanometric-thin rubidium vapor cell", Applied Physics B. Lasers and Optics **105**, 767 (2011).
- [12] D. Sarkisyan, G. Hakhumyan, A. Sargsyan, R. Mirzoyan, C. Leroy, Y. Pashayan-Leroy, "Laser Spectroscopy with Nanometric Cells Containing Atomic Vapor of Metal: Influence of Buffer Gas", Proc. SPIE **7747**, 77470C-1 (2011).
- [13] D. Sarkisyan, G. Hakhumyan, R. Mirzoyan, A. Papoyan, A. Atvars, M. Auzinsh, "Use of nanocell with the thickness $L = \lambda$ for study atomic transition of Rb D_2 -line in magnetic field", Proceedings of conference "Laser Physics - 2007", pp. 87-90, Ashtarak, Armenia (2008). R Mirzoyan, A Sargsyan, A S. Sarkisyan, D Sarkisyan
- [14] R. Mirzoyan, A. Sargsyan, A. S. Sarkisyan, D. Sarkisyan, "Study of the splitting of electromagnetically induced transparency resonance in strong magnetic field using Rb nano-thin cell", Journal of Physics: Conference Series **350**, 012008 (2012).

Conference thesis and abstracts

- [15] R. Mirzoyan, G. Hakhumyan, C. Leroy, Y. Pashayan-Leroy and D. Sarkisyan, "Modification of Initially Forbidden Atomic Transitions of Rb D_2 -line in Magnetic Field", 44th Conference of the European Group for Atomic Systems (EGAS), Book of Abstracts P-156, University of Gothenburg, Sweden (2012).
- [16] A. Sargsyan, R. Mirzoyan, C. Leroy, Y. Pashayan-Leroy and D. Sarkisyan, "N-resonance Formation in Micrometric-Thin Cell Filled with Rubidium and Buffer Gas", 44th Conference of the European Group for Atomic Systems (EGAS), Book of Abstracts P-161, University of Gothenburg, Sweden (2012).
- [17] R. Mirzoyan, A. Sargsyan, D. Sarkisyan, "Study of the Rb Dark-line atomic resonance splitting in a Strong Magnetic Field", Book of Abstract Laser Physics P3-7, p-60, (2011).
- [18] D. Sarkisyan, A. Sargsyan, R. Mirzoyan, Y. Pashayan-Leroy, and C. Leroy, "High contrast subnatural resonance of increased absorption formed in cell filled with Rb and buffer gas", 43rd Conference of the European Group for Atomic Systems (EGAS), Book of Abstracts P-46, University of Fribourg, Switzerland (2011).
- [19] Y. Pashayan-Leroy, C. Leroy, A. Sargsyan, R. Mirzoyan, and D. Sarkisyan, "High-contrast dark line atomic resonance of D_1 excitation in nanometric-thin cell filled with rubidium", 43rd Conference of the European Group for Atomic Systems (EGAS), Book of Abstracts P-177, University of Fribourg, Switzerland (2011).
- [20] A. Sargsyan, R. Mirzoyan, A. Papoyan, D. Sarkisyan, Y. Pashayan-Leroy, and C. Leroy, "Study of electromagnetically induced transparency in strong magnetic field using Rb nanometric-thin cell", 43rd Conference of the European Group for Atomic Systems (EGAS), Book of Abstracts P-180, University of Fribourg, Switzerland (2011).
- [21] A. Sargsyan, H. Hakhumyan, R. Mirzoyan, Y. Pashayan-Leroy, C. Leroy, D. Sarkisyan, "Atom-Wall collisions influence on dark-line atomic resonances in submicron thin vapor

cells”, 10th European Conference on Atoms, Molecules and Photons, ECAMP10, Book of Abstracts P-339, Salamanca, Spain (2010).

Cited literature

- [22] S. E. Harris, J. E. Field, and A. Imamoglu, ”Nonlinear Optical Processes Using Electromagnetically Induced Transparency”, *Phys. Rev. Lett.* **64**, 1107-1110 (1990).
- [23] U. Fano, ”Effects of Configuration Interaction on Intensities and Phase Shifts”, *Phys. Rev. A* **124**, 1866 (1961).
- [24] K. J. Boller, A. Imamoglu, and S. E. Harris, ”Observation of Electromagnetically Induced Transparency”, *Phys. Rev. Lett.* **66**, 2593-2596 (1991).
- [25] J. E. Field, K. H. Hahn, and S. E. Harris, ”Observation of Electromagnetically Induced Transparency in Collisionally Broadened Lead Vapor”, *Phys. Rev. Lett.* **67**, 3062-3065 (1991).
- [26] M. Jain, H. Xia, G. Y. Yin, A. J. Merriam, and S. E. Harris, ”Efficient Nonlinear Frequency Conversion with Maximal Atomic Coherence”, *Phys. Rev. Lett.* **77**, 4326-4329 (1996).
- [27] D. Budker, D. F. Kimball, S. M. Rochester, and V. V. Yashchuk, ”Nonlinear Magneto-optics and Reduced Group Velocity of Light in Atomic Vapor with Slow Ground State Relaxation”, *Phys. Rev. Lett.* **83**, 1767-1770 (1999).
- [28] H. Y. Ling, Y. Q. Li, and M. Xiao, ”Electromagnetically induced grating: Homogeneously broadened medium”, *Phys. Rev. A* **57**, 1338-1344 (1998).
- [29] J. P. Marangos, ”Topical review electromagnetically induced transparency”, *J. Modern Optics* **45**, 471-503 (1998).
- [30] S. E. Harris, ”Electromagnetically induced transparency”, *Physics Today* **50(7)**, 36-42 (1997).

- [31] Kuo-Cheng Chen, B.Sc., M.Sc., M.S., "Effects of laser pulse shape and beam profile on Electromagnetically-induced transparency", The University of Texas at Dallas (2000).
- [32] M. O. Scully, "Enhancement of the index of refraction via quantum coherence", Phys. Rev. Lett. **67**, 1855 (1991).
- [33] S. E. Harris, J. E. Field and A. Kasapi, "Dispersive Properties of Electromagnetically Induced Transparency", Phys. Rev. A **46**, R29 (1992); A. D. Wilson-Gordon and H. Friedmann, "Enhanced index of refraction: a comparison between two- and three-level systems", Opt. Commun. **94**, 238 (1992); M. O. Scully and S.-Y. Zhu, "Ultra-large index of refraction via quantum interference", *ibid.* **87**, 134 (1992).
- [34] S. E. Harris, "Refractive-index control with strong fields", Opt. Lett. **19**, 2018 (1994); M. Xiao, Y.-Q. Li, S.-Z. Jin and J. Gea-Banacloche, "Measurement of Dispersive Properties of Electromagnetically Induced Transparency in Rubidium Atoms", Phys. Rev. Lett. **74**, 666 (1995).
- [35] O. Kocharovskaya and Y.I. Khanin, "Coherent Amplification of an Ultrashort Pulse in a Three Level Medium without Population Inversion", JETP Lett. **48**, 630 (1988).
- [36] M.O. Scully, S.Y. Zhu, and A. Gavrielides, "Degenerate Quantum-Beat Laser: Lasing without Inversion and Inversion without Lasing", Phys. Rev. Lett. **62**, 2813 (1989).
- [37] V.G. Arkhipkin and Y.I. Heller, "Radiation Amplification without Population Inversion at Transitions to Autoionising States", Phys. Lett. **98A**, 12 (1983).
- [38] S.E. Harris, "Lasers without Inversion: Interference of a Lifetime Broadened Resonance", Phys. Rev. Lett. **62**, 1033 (1989).
- [39] A. Imamoglu and S.E. Harris, "Lasers without Inversion: Interference of Dressed Lifetime broadened states", Opt. Lett. **14**, 1344 (1989).
- [40] E.E. Fill, M.O. Scully, and S.-Y. Zhu, "Lasing without Inversion via the Lambda Quantum-Beat Laser in the Collision Dominated Regime", Opt. Commun. **77**, 36 (1990).

- [41] G. G. Padmabandu, G. R. Welch, I. N. Shubin, E. S. Fry, D. E. Nikonov, M. D. Lukin and M. O. Scully, "Laser Oscillation without Population Inversion in a Sodium Atomic Beam", *Phys. Rev. Lett.* **76**, 2053 (1996).
- [42] A. S. Zibrov, M. D. Lukin, D. E. Nikonov, L. Hollberg, M. O. Scully, V. L. Velichansky and H. G. Robinson, "Experimental Observation of Laser Oscillation without Population Inversion via Quantum Interference in Rb", *Phys. Rev. Lett.* **75**, 1499 (1995).
- [43] A. Kasapi, "Enhanced isotope discrimination using electromagnetically induced transparency", *Phys. Rev. Lett.* **77**, 1035 (1996).
- [44] H. Schmidt and A. Imamoglu, "Giant Kerr nonlinearities obtained by electromagnetically induced transparency", *Opt. Lett.* **21**, 1936 (1996).
- [45] P. R. Hemmer, D. P. Katz, J. Donoghue, M. Cronin-Golomb, M. S. Shahriar, and P. Kumar, "Efficient low-intensity optical phase conjugation based on coherent population trapping in sodium", *Opt. Lett.* **20**, 982 (1995).
- [46] M. Jain, H. Xia, G. Y. Yin, A. J. Merriam, and S. E. Harris, "Efficient nonlinear frequency conversion with maximal atomic coherence", *Phys. Rev. Lett.* **77**, 4326 (1996).
- [47] K. H. Hahn, D. A. King and S. E. Harris, "Nonlinear generation of 104.8-nm radiation within an absorption window in zinc", *Phys. Rev. Lett.* **65**, 2777 (1990).
- [48] K. Hakuta, L. Marmet and B. P. Stoicheff, "Electric-field-induced second-harmonic generation with reduced absorption in atomic hydrogen", *Phys. Rev. Lett.* **66**, 596 (1991); *Phys. Rev. A* **45**, 5152 (1992).
- [49] P. Hemmer, S. Ezekiel, and J. C. C. Leiby, "Stabilization of a microwave oscillator using a resonance Raman transition in a sodium beam", *Opt. Lett.* **8**, 440 (1983).
- [50] M. Scully and M. Fleischhauer, "High-sensitivity magnetometer based on index-enhanced media", *Phys. Rev. Lett.* **69**, 1360 (1992).
- [51] M. Fleischhauer and M. Scully, "Quantum sensitivity limits of an optical magnetometer based on atomic phase coherence", *Phys. Rev. A* **49**, 1973 (1994).

- [52] D. Budker, V. Yashchuk, and M. Zolotarev, "Nonlinear magneto-optic effects with ultranarrow widths", *Phys. Rev. Lett.* **81**, 5788 (1998).
- [53] M. Linberg and R. Binder, "Dark states in coherent semiconductor spectroscopy", *Phys. Rev. Lett.* **75**, 1403 (1995).
- [54] R. Wynands and A. Nagel, "Precision spectroscopy with coherent dark states", *Appl. Phys. B* **68**, 1 (1999).
- [55] S. Brandt, A. Nagel, R. Wynands, D. Meschede, "Buffer-gas-induced linewidth reduction of coherent dark resonances to below 50 Hz", *Phys. Rev. A* **56**, R1063 (1997).
- [56] J. Kitching, S. Knappe and L. Hollberg, "Miniature vapor-cell atomic-frequency references", *Appl. Phys. Lett.* **81(3)**, 553 (2002).
- [57] M. Erhard and H. Helm, "Buffer-gas effects on dark resonances: Theory and experiment", *Phys. Rev. A* **63**, 043813 (2001).
- [58] Schmidt, O., Wynands, R., Hussein, Z., and Meschede, D., "Steep dispersion and group velocity below $c/3000$ in coherent population trapping", *Phys. Rev. A*, **53**, R27 (1996).
- [59] Xiao, M., qing Li, Y., zheng Jin, S., and Gea-Banacloche, J., "Measurement of dispersive properties of electromagnetically induced transparency in rubidium atoms", *Phys. Rev. Lett.*, **74**, 666 (1995).
- [60] G. Alzetta, A. Gozzini, L. Moi, G. Orriols, "An Experimental Method for the Observation of R.F. Transitions of Laser Beat Resonances in Oriented Na vapor", *Il Nuovo Cimento B* **36**, 5 (1976).
- [61] H.R. Gray, R.M. Whitley, C.R. Stroud, "Coherent trapping of atomic populations", *Opt. Lett.* **3**, 218 (1978)
- [62] D. Budker, D. F. Kimball, S. M. Rochester, and V. V. Yashchuk, "Nonlinear magneto-optics and reduced group velocity of light in atomic vapor with slow ground state relaxation", *Phys. Rev. Lett.* **83**, 1767 (1999).

- [63] L. Hau, S. Harris, Z. Dutton, and C. Behroozi, "Light speed reduction to 17 metres per second in an ultracold atomic gas", *Nature* **397**, 594 (1999).
- [64] M. Kash *et al.*, "Ultraslow group velocity and enhanced nonlinear optical effects in a coherently driven hot atomic gas", *Phys. Rev. Lett.* **82**, 5229 (1999).
- [65] A. V. Turukhin, V. S. Sudarshanam, M. S. Shahriar, J. A. Musser, B. S. Ham, P. R. Hemmer, "Observation of ultraslow and stored light pulses in a solid", *Phys. Rev. Lett.*, **88**, 023602 (2002).
- [66] Fleischhauer, M. and Lukin, M. D., "Dark-state polaritons in electromagnetically induced transparency", *Phys. Rev. Lett.*, **84**, 5094-5097 (2000).
- [67] Wesley W. Erickson, "Electromagnetically Induced Transparency", Department of Physics, Reed College, Portland, Oregon 27708, USA (2012).
- [68] Lukin, M. D. and Imamoglu, A., "Controlling photons using electromagnetically induced transparency", *Nature*, **413**, 273 (2001).
- [69] C. Liu, Z. Dutton, C. H. Behroozi, and L. V. Hau, "Observation of coherent optical information storage in an atomic medium using halted light pulses", *Nature* **409**, 490 (2001).
- [70] D. Phillips, M. Fleischhauer, A. Mair, R. Walsworth, and M. D. Lukin, "Storage of light in atomic vapor", *Phys. Rev. Lett.* **86**, 783 (2001).
- [71] O. Kocharovskaya, Y. Rostovtsev, and M. O. Scully, "Stopping light via hot atoms", *Phys. Rev. Lett.* **86**, 628 (2001).
- [72] Longdell JJ, Fraval E, Sellars MJ, Manson NB, "Stopped light with storage times greater than one second using electromagnetically induced transparency in a solid", *Phys. Rev. Lett* **95**, 063601 (2004).
- [73] M. D. Eisaman, A. André, F. Massou, M. Fleischhauer, A. S. Zibrov, and M. D. Lukin, "Electromagnetically induced transparency with tunable single-photon pulses", *Nature* **438**, 837 (2005).

- [74] Julio Gea-Banacloche, Yong-qing Li, Shao-zheng Jin, and Min Xiao, "Electromagnetically induced transparency in ladder-type inhomogeneously broadened media: Theory and experiment", *Phys. Rev. A* **51**, 576 (1995).
- [75] Cohen-Tannoudji, C., J. Dupont-Roc, and G. Grynberg, 1992, *Atom-Photon Interactions* (Wiley, New York).
- [76] Oreg J., F. T. Hioe, and J. H. Eberly, "Adiabatic following in multilevel systems", *Phys. Rev. A* **29**, 690 (1984).
- [77] D. A. Steck, "Rubidium 85 *D* Line Data," Available online at: <http://steck.us/alkalidata> (revision 2.1.3, 23 December 2010) (2010).
- [78] R. Wynands, A. Nagel, "Precision spectroscopy with coherent dark states", *Appl. Phys. B, Lasers Opt.* **68**, 1 (1999).
- [79] H. N. De Freitas, M. Oria, M. Chevrollier, "Spectroscopy of cesium atoms adsorbing and desorbing at a dielectric surface", *Appl. Phys. B* **75**, 703 (2002).
- [80] S. Knappe, L. Hollberg, J. Kitching, "Dark-line atomic resonances in submillimeter structures", *Opt. Lett.* **29**, 388 (2004).
- [81] K. Fukuda, A. Toriyama, A. Izmailov, M. Tachikawa, "Dark resonance of Cs atoms velocity-selected in a thin cell", *Appl. Phys. B* **80**, 503 (2005).
- [82] E. B. Alexandrov, "Recent progress in optically pumped magnetometers", *Phys. Scr., T* **105**, 2730 (2003).
- [83] A. Aspect, E. Arimondo, R. Kaiser, N. Vansteenkiste, and C. Cohen-Tannoudji, "Laser Cooling below the One-Photon Recoil Energy by Velocity-Selective Coherent Population Trapping", *Phys. Rev. Lett.* **61**, 826 (1988).
- [84] A. Aspect, E. Arimondo, R. Kaiser, N. Vansteenkiste, and C. Cohen-Tannoudji, "Laser cooling below the one-photon recoil energy by velocity-selective coherent population trapping: theoretical analysis", *J. Opt. Soc. Am. B* **6**, 2112 (1989).

- [85] J. Vanier, "Atomic clocks based on coherent population trapping: a review", *Appl. Phys. B.* **81**, 421 (2005).
- [86] A.K. Mohapatra, T.R. Jackson, C.S. Adams, "Coherent Optical Detection of Highly Excited Rydberg States Using Electromagnetically Induced Transparency", *Phys. Rev. Lett.* **98**, 113003 (2007).
- [87] A. Sargsyan, D. Sarkisyan, A. Papoyan, "Dark-line atomic resonances in a submicron-thin Rb vapor layer", *Phys. Rev. A* **73**, 033803 (2006).
- [88] Y. Pashayan-Leroy, C. Leroy, A. Sargsyan, A. Papoyan, D. Sarkisyan, "Electromagnetically induced transparency: the thickness of the vapor column is of the order of a light wavelength", *J. Opt. Soc. Am. B* **24**, 1829 (2007).
- [89] Zhen-Sheng Yuan, Yu-Ao Chen, Bo Zhao, Shuai Chen, Jorg Schmiedmayer, Jian-Wei Pan, "Experimental demonstration of a BDCZ quantum repeater node", *Nature* **454**, 1098 (2008).
- [90] I. Hamdi, P. Todorov, A. Yarovitski, G. Dutier, I. Maurin, S. Saltiel, Y. Li, A. Lezama, T. Varzhapetyan, D. Sarkisyan, M.-P. Gorza, M. Fichet, D. Bloch and M. Ducloy, "Laser Spectroscopy with Nanometric Gas Cells: Distance Dependence of Atom-Surface Interaction and Collisions under Confinement", *Laser Phys.* **15**, 987 (2005).
- [91] B.W. Shore, *The Theory of Coherent Atomic Excitation*, John Wiley & Sons, New York 1990.
- [92] B.J. Dalton and P.L. Knight, "Population trapping and ultranarrow Raman lineshapes induced by phase-fluctuating fields", *Opt. Commun.* **42**, 411 (1982).
- [93] J.H. Eberly, "Atomic Relaxation in the Presence of Intense Partially Coherent Radiation Fields", *Phys. Rev. Lett.* **37**, 1387 (1976).
- [94] G.S. Agarwal, "Exact Solution for the Influence of Laser Temporal Fluctuations on resonance Fluorescence", *Phys. Rev. Lett.* **37**, 1383 (1976).
- [95] G.S. Agarwal, "Quantum statistical theory of optical-resonance phenomena in fluctuating laser fields", *Phys. Rev. A* **18**, 1490 (1978).

- [96] G. Dutier, S. Saltiel, D. Bloch, M. Ducloy, "Revisiting optical spectroscopy in a thin vapor cell: mixing of reflection and transmission as a FabryPerot microcavity effect", *J. Opt. Soc. Am. B* **20**, 793 (2003).
- [97] A.J. Krmpot, M.M. Mijailovic, B.M. Panic, D.V. Lukic, A.G. Kovacevic, D.V. Pantelic, B.M. Jelenkovic, "Sub-Doppler absorption narrowing in atomic vapor at two intense laser fields", *Opt. Express* **13**, 1448 (2005).
- [98] T. A. Vartanyan and D. L. Lin, "Enhanced selective reflection from a thin layer of a dilute gaseous medium", *Phys. Rev. A* **51**, 1959 (1995).
- [99] A. Sargsyan, A.V. Papoyan, D. Sarkisyan, A. Weis, "Efficient technique for measuring laser frequency stability", *Eur. Phys. J.- Appl. Phys.* **48**, 20701 (2009).
- [100] D.H. Sarkisyan, A.S. Sarkisyan, A.K. Yalanusyan, "Thermal Dissociation of Cesium Dimers", *Appl. Phys. B* **66**, 241 (1998).
- [101] D. Sarkisyan, U. Hinze, L. Meyer, B. Wellegehausen, "Efficient cw Sodium dimer Raman laser operation in a high-temperature sapphire cell", *Appl. Phys. B* **70**, 351 (2000).
- [102] D. Sarkisyan, D. Bloch, A. Papoyan, M. Ducloy, "Sub-Doppler spectroscopy by sub-micron thin Cs vapor layer", *Opt. Comm.* **200**, 201 (2001).
- [103] G. Dutier, A. Yarovitski, S. Saltiel, A. Papoyan, D. Sarkisyan, D. Bloch, M. Ducloy, "Collapse and revival of a Dicke-type coherent narrowing in a sub-micron thick vapor cell transmission spectroscopy", *Europhys. Lett.* **63**, 35 (2003).
- [104] D. Sarkisyan, T. Becker, A. Papoyan, P. Thoumany, H. Walther, "Sub-Doppler fluorescence on the atomic D_2 line of a submicron rubidium-vapor layer", *Appl. Phys. B* **76**, 625 (2003).
- [105] M. Stähler, R. Wynands, S. Knappe, J. Kitching, L. Hollberg, A. Taichenachev, V. Yudin, "Coherent population trapping resonances in thermal ^{85}Rb vapor: D_1 versus D_2 line excitation", *Optics Lett.* **27**, 1472 (2002).
- [106] S.A. Knappe, H.G. Robinson, L. Hollberg, "Microfabricated saturated absorption laser spectrometer", *Opt. Express* **15**, 6293 (2007).

- [107] P. Wang, A. Gallagher, J. Cooper, "Selective reflection by Rb", Phys. Rev. A **56**, 1598 (1997).
- [108] D. Sarkisyan, T. Varzhapetyan, A. Sarkisyan, Yu. Malakyan, A. Papoyan, A. Lezama, D. Bloch, M. Ducloy, "Spectroscopy in an extremely thin vapor cell: Comparing the cell length dependence in fluorescence and in adsorption techniques", Phys. Rev. A **69**, 065802 (2004).
- [109] C. Andreeva, S. Cartaleva, L. Petrov, S.M. Saltiel, D. Sarkisyan, T. Varzhapetyan, D. Bloch, M. Ducloy, "Saturation effects in the sub-Doppler spectroscopy of cesium vapor confined in an extremely thin cell", Phys. Rev. A **76**, 013837 (2007).
- [110] X. Wei, J. Wu, G. Sun, Z. Shao, Z. Kang, Y. Jiang, J-Y.Gao, "Splitting of an electromagnetically induced transparency window of rubidium atoms in a static magnetic field", Phys. Rev. A **72**, 0238061 (2005).
- [111] S. M. Iftiqar and V. Natarajan, "Line narrowing of electromagnetically induced transparency in Rb with a longitudinal magnetic field", Phys. Rev. A **79**, 013808 (2009).
- [112] G. Katsoprinakis, D. Petrosyan and I. K. Kominis, "High Frequency Atomic Magnetometer by Use of Electromagnetically Induced Transparency", Phys. Rev.Lett. **97**, 230801 (2006).
- [113] V. I. Yudin, A. V. Taichenachev, Y. O. Dudin, *et al.*, "Vector magnetometry based on electromagnetically induced transparency in linearly polarized light", Phys. Rev. A **82**, 033807 (2010).
- [114] R. Höller, F. Renzoni, L. Windholz, and J. H. Xu, "Coherent population trapping on the sodium D_1 line in high magnetic fields", J. Opt. Soc. Am. **14**, 2221 (1997).
- [115] K. Motomura, and M. Mitsunaga, "High-resolution spectroscopy of hyperfine Zeeman components of the sodium D_1 line by coherent", J. Opt. Soc. Am. **19**, 2456 (2002).
- [116] P. Tremblay, A. Michaud, M. Levesque, S. Theriault, M. Breton, J. Beaubien, N. Cyr, "Absorption profiles of alkali-metal D lines in the presence of a static magnetic field", Phys. Rev. A **42**, 2766 (1990).

- [117] E.B. Aleksandrov, M.P. Chaika, G.I. Khvostenko, “Interference of Atomic States”, (Springer-Verlag, New York, 1993).
- [118] A. Sargsyan, G. Hakhumyan, A. Papoyan, D. Sarkisyan, A. Atvars, M. Auzinsh, “A novel approach to quantitative spectroscopy of atoms in a magnetic field and applications based on an atomic vapor cell with $L = \lambda$ ”, Appl. Phys. Lett. **93**, 021119 (2008).
- [119] G. Hakhumyan, D. Sarkisyan, A. Sargsyan, A. Atvars, M. Auzinsh, “Investigation of Rb D_1 atomic lines in strong magnetic fields by fluorescence from a half-wave-thick cell”, Optics and Spectroscopy, Vol. 108, No. 5, pp. 685-692 (2010).
- [120] G. Hakhumyan, C. Leroy, Y. Pashayan-Leroy, D. Sarkisyan, M. Auzinsh, “High-spatial-resolution monitoring of strong magnetic field using Rb vapor nanometric-thin cell”, Opt. Comm. **284**, 4007 (2011).
- [121] A. Sargsyan, D. Sarkisyan, D. Staedter, A. M. Akulshin, “Doppler-free satellites of resonances of electromagnetically induced transparency and absorption on the D_2 lines of alkali metals”, Optics and Spectroscopy **101**, 762 (2006).
- [122] A. Sargsyan and D. Sarkisyan, ”Electromagnetically induced transparency in Λ -system involving D_2 line of Rb atoms confined in sub-micron columns”, Optics and Spectroscopy **111** (3), 334 (2011).
- [123] J. Wang, Y. Wang, S. Yan, T. Liu, T. Zhang, ”Observation of sub-Doppler absorption in the Λ -type three-level Doppler-broadened cesium system”, Appl. Phys. B **78**, 217 (2004).
- [124] M. Auzinsh, D. Budker, S.M. Rochester, “Optically polarized atoms: understanding light-atom interactions”, (Oxford University Press, 2010).
- [125] S. Knappe, P. Schwindt, V. Shah, L. Hollberg, J. Kitching, L. Liew, J. Moreland, “A chip-scale atomic clock based on ^{87}Rb with improved frequency stability,” Opt. Express **13**, 1249 (2005).

- [126] A. Sargsyan, M. G. Bason, D. Sarkisyan, A. K. Mohapatra, and C. S. Adams, "Electromagnetically induced transparency and two-photon absorption in the ladder system in thin columns of atomic vapors", *Opt. Spectrosc.* **109** (4), 529 (2010).
- [127] G. Hakhumyan, A. Sargsyan, C. Leroy, *et al.*, "Essential Features of Optical Processes in Rb submicron Thin Cell Filled with Neon Gas," *Opt. Express.* **18**, 14577 (2010).
- [128] B. A. Olsen, B. Patton, Y.-Y. Jau, W. Happer, "Optical pumping and spectroscopy of Cs vapor at high magnetic field", *Phys. Rev. A* **84**, 063410 (2011).
- [129] A. Imamoglu, H. Schmidt, G. Woods, and M. Deutsch, "Strongly interacting photons in a nonlinear cavity", *Phys. Rev. Lett.* **79**, 1467 (1997).
- [130] H. Schmidt and A. Imamoglu, "Giant Kerr nonlinearities obtained by electromagnetically induced transparency", *Opt. Lett.* **21**, 1936 (1996).
- [131] S.E. Harris and L.V. Hau, "Nonlinear Optics at Low Light Levels", *Phys. Rev. Lett.* **82**, 4611 (1999).
- [132] M.D. Lukin and A. Imamoglu, "Nonlinear Optics and Quantum Entanglement of Ultraslow Single Photons", *Phys. Rev. Lett.* **84**, 1419 (1999).
- [133] S.E. Harris and Y. Yamamoto, "Photon Switching by Quantum Interference", *Phys. Rev. Lett.* **81**, 3611 (1998).
- [134] A.K. Popov and V.M. Shalaev, "Elimination of Doppler broadening at coherently driven quantum transitions", *Phys. Rev. A* **59**, 946 (1999).
- [135] I. Novikova, D. F. Phillips, A. S. Zibrov, R. L. Walsworth, A. V. Taichenachev, and V. I. Yudin, "Comparison of ^{87}Rb N -resonances for D_1 and D_2 transitions," *Opt. Lett.* **31**, 2353–2355 (2006).
- [136] I. Novikova, D. F. Phillips, A. S. Zibrov, R. L. Walsworth, A. V. Taichenachev, and V. I. Yudin, "Cancellation of light shifts in an N -resonance clock," *Opt. Lett.* **31**, 622–624 (2006).

- [137] C. Hancox, M. Hohensee, M. Crescimanno, D. F. Phillips, and R. L. Walsworth, “Lineshape asymmetry for joint coherent population trapping and three-photon N -resonances,” *Opt. Lett.* **33**, 1536–1538 (2008).
- [138] I. Ben-Aroya, G. Eisenstein, “Observation of large contrast electromagnetically induced absorption resonance due to population transfer in a three-level Λ -system interacting with three separate electromagnetic fields,” *Optics Express* **19**, 9956 (2011).
- [139] T. Baluktsian, C. Urban, T. Bublat, H. Giessen, R. Löw, T. Pfau, “Fabrication method for microscopic vapor cells for alkali atoms,” *Opt. Lett.* **35**, 1950–1952 (2010).
- [140] A. Sargsyan, G. Hakhumyan, C. Leroy, *et al.*, “Hyperfine Paschen-Back regime realized in Rb nanocell,” *Opt. Lett.* **37**, 1379 (2012).
- [141] M. Auzinsh, D. Budker, S.M. Rochester “Optically Polarized Atoms: Understanding Light-Atom Interactions,” Oxford University Press: ISBN-10:0199565120 (2010).
- [142] A. Sargsyan, A. Papoyan, A. Sarkisyan, Yu. Malakyan, G. Grigoryan, and D. Sarkisyan, “Narrow and contrast resonance of increased absorption in Λ -system observed in Rb cell with buffer gas,” *Armenian Journal of Physics* **2**, 84 (2009).
- [143] P. R. S. Carvalho, L. E. E. de Araujo, and J. W. R. Tabosa, ”Angular dependence of an electromagnetically induced transparency resonance in a Doppler-broadened atomic vapor”, *Phys. Rev. A* **70**, 063818 (2004).
- [144] Happer, W., ”Optical Pumping”, *Rev. Mod. Phys.* **44**, 169 (1972).
- [145] Letokhov, V.S. and Chebotaev, V.P., original in Russian: ”Nelineynaya lazernaya spektroskopiya sverkhvysokogo razresheniya” (Ultra-High Resolution Nonlinear Laser Spectroscopy), Moscow: Nauka, 1990.
- [146] D. Sarkisyan, A. Papoyan, T. Varzhapetyan, K. Blush, M. Auzinsh, “Fluorescence of Rb in a sub-micron vapor cell: spectral resolution of atomic transitions between Zeeman sublevels in moderate magnetic field”, *J. Opt. Soc. Am. B* **22**, 88 (2005).

- [147] A. Sargsyan, D. Sarkisyan, U. Krohn, J. Keaveney, Ch. Adams, "Effect of buffer gas on an electromagnetically induced transparency in a ladder system using thermal rubidium vapor", *Phys. Rev. A* **82**, 045806 (2010).
- [148] M. A. Kumar and S. Singh, "Electromagnetically induced transparency and slow light in three-level ladder systems: Effect of velocity-changing and dephasing collisions", *Phys. Rev. A* **79**, 063821 (2009).
- [149] N. N. Badalyan, M. E. Movsesyan, and V. A. Iradyan, "Stimulated resonance effects in potassium vapor", *JETP Lett.* **6** (5), 127 (1967).
- [150] M. L. Ter-Mikaelyan and A. O. Melikyan, "Rayleigh and Raman scattering in the field of an intense wave", *Sov. Phys. JETP* **31** (1), 153 (1970).

Title: Study of the coherent effects in rubidium atomic vapor under bi-chromatic laser radiation.

Abstract: The effect of electromagnetically induced transparency is observed, using nanocell and microcell. The EIT-resonance with good parameters (high contrast and small FWHM) is obtained in thick cells. The EIT-resonance splitting in magnetic field is observed for the cases of D_1 -line of ^{85}Rb and ^{87}Rb . The theoretical model, explaining the EIT-resonance components frequency shift dependence on magnetic field strength is presented. The theoretical and experimental results are compared and good agreement is shown. Also the EIT-resonance behavior in hyperfine Paschen-Back regime is presented and explained.

For the first time the N -type resonance in microcell is observed. Good parameters of the N -type resonance in microcell are obtained. It allows us to observe the N -type resonance behavior in magnetic field. The N -resonance splitting in magnetic field is observed for the cases of ^{85}Rb and ^{87}Rb . The theoretical calculations of the N -resonance components frequency shift dependence on magnetic field is presented. The theoretical and experimental results are compared and good agreement is shown. Also the N -resonance behavior in hyperfine Paschen-Back regime is presented and explained. Simultaneous observation of N - and EIT-resonance is shown. Comparison of EIT- and N -resonance is made.

Key words: Rb hyperfine structure; diode laser; high resolution spectroscopy; nanocell; microcell; combined multi-region cells; buffer gas; Zeeman effect; EIT-resonance; N -type resonance; hyperfine Paschen-Back regime; Λ -system.

Titre : Etude des effets cohérents dans la vapeur de rubidium atomique sous irradiation laser bichromatique.

Résumé : L'effet de la transparence induite électromagnétiquement est observé à l'aide de cellules nanométriques et de cellules micrométriques. La résonance EIT avec de bons paramètres (fort contraste et faible largeur du signal à mi-hauteur) est obtenue dans des cellules étroites. L'éclatement de la résonance EIT dans un champ magnétique est observé pour les raies D_1 du ^{85}Rb et ^{87}Rb . Nous présentons un modèle théorique qui explique la dépendance du déplacement en fréquence des composantes de la résonance EIT en fonction de l'intensité du champ magnétique. Les résultats théoriques et expérimentaux sont comparés et démontrent un bon accord.

Pour la première fois une résonance de type N est obtenue dans une micro-cellule. Nous obtenons de bons paramètres (fort contraste et faible largeur du signal à mi-hauteur) de la résonance N à l'aide d'une micro-cellule. Cela nous permet d'observer le comportement d'une résonance N dans un champ magnétique. L'éclatement de la résonance N dans un champ magnétique est observé pour les raies D_1 du ^{85}Rb et ^{87}Rb . Nous présentons les calculs théoriques qui expliquent la dépendance du déplacement en fréquence des composantes de la résonance N en fonction de l'intensité du champ magnétique. Les résultats théoriques et expérimentaux sont comparés et démontrent un bon accord. Le comportement de la résonance N en régime hyperfin Paschen-Back est présenté et expliqué. Enfin une comparaison des résonances EIT et N est faite.

Mots clefs : Structure hyperfine Rb ; diode laser ; spectroscopie à haute résolution ; nano-cellules ; micro-cellules ; cellules multi-régions combinées ; gaz tampon ; effet Zeeman ; résonance EIT ; résonance N ; régime hyperfin Paschen-Back ; système Λ .